

Supersolid Phases
in Mass Imbalanced Fermi Mixtures

Jildou Baarsma
Supersolid phases in mass imbalanced Fermi mixtures
Instituut voor Theoretische Fysica
Universiteit Utrecht
ISBN: 978-90-393-6007-1

Supersolid Phases in Mass Imbalanced Fermi Mixtures

Supervloeibare Kristallen
in Fermi mengsels met ongelijke massas

(met een samenvatting in het Nederlands)

Proefschrift

ter verkrijging van de graad van doctor aan de Universiteit Utrecht
op gezag van de rector magnificus, prof.dr. G. J. van der Zwaan,
ingevolge het besluit van het college voor promoties in het openbaar
te verdedigen op woensdag 4 september 2013 des middags te 12.45 uur

door

Jildou Eltje Baarsma

geboren op 29 oktober 1986 te Groningen

Promotor : Prof.dr.ir. H. T. C. Stoof

Publications

This thesis is based on the following publications:

- J. E. Baarsma, K. B. Gubbels and H. T. C. Stoof, *Population and mass imbalance in atomic Fermi gases*, Phys. Rev. A **82**, 013624 (2010).
- J. E. Baarsma, J. Armaitis, R. A. Duine and H. T. C. Stoof, *Polarons in extremely polarized Fermi gases: The strongly interacting ^6Li - ^{40}K mixture*, Phys. Rev. A **85**, 033631 (2012).
- J. E. Baarsma and H. T. C. Stoof, *Inhomogeneous superfluid phases in ^6Li - ^{40}K mixtures at unitarity*, Phys. Rev. A **87**, 063612 (2013).

Other publications the author has contributed to:

- K. B. Gubbels, J. E. Baarsma and H. T. C. Stoof, *Lifshitz Point in the Phase Diagram of Resonantly Interacting ^6Li - ^{40}K Mixtures*, Phys. Rev. Lett. **103**, 195301 (2009).

The Dutch summary is based on:

- J.E. Baarsma, *Inhomogene Supervloeistoffen*, Nederlands Tijdschrift voor Natuurkunde **79**, 108 (2013).

Contents

1	Introduction	9
1.1	Ultracold atoms	10
1.2	^6Li - ^{40}K mixtures	14
1.3	Strong interactions and universal behavior	16
1.4	Transport	18
1.5	Phase transitions and long-range order	19
1.6	Outline	21
2	Polarons in extremely polarized Fermi gases	23
2.1	Introduction	23
2.2	Molecular bound state	25
2.3	Spin polaron	27
2.4	Spin-drag relaxation rate	30
2.5	Conclusion	32
2.6	Appendix: Boltzmann transport theory	32
3	Population and mass imbalance in atomic Fermi gases	35
3.1	Introduction	35
3.2	Interactions and Feshbach resonances	38
3.3	Landau theory of phase transitions	40
3.4	Mean-Field theory	43
3.5	Fluctuation effects	60
3.6	Discussion and Conclusion	64
3.7	Appendix: Derivation of the thermodynamic potential	64
3.8	Appendix: Feynman diagrams	67

4 Inhomogeneous superfluid phases	71
4.1 Introduction	71
4.2 Thermodynamic potential	75
4.3 Ginzburg-Landau expansion	81
4.4 LO Green's function	88
4.5 Inhomogeneous densities	90
4.6 Discussion and Conclusion	91
Nederlandse samenvatting	93
Bibliography	101

CHAPTER 1

Introduction

In April 1911 Heike Kamerlingh Onnes discovered the phenomenon of superconductivity [1]. In particular, Kamerlingh Onnes observed the abrupt vanishing of the electrical resistance in a solid mercury wire at a temperature of 4.2 K, a temperature he reached by immersing the wire in liquid helium. Now we know that lattice vibrations inside the solid, so-called phonons, mediate an attractive interaction between the electrons inside the wire. This weak interaction is strong enough to cause the formation of loosely bound Cooper pairs, consisting of two electrons with opposite spin, inside the wire. Below the critical temperature for superconductivity a substantial fraction of Cooper pairs occupies the same quantum state. One of the properties of this collective state is the disappearance of electrical resistance. The above explanation of superconductivity only came in 1957 by Bardeen, Cooper and Schrieffer [2]. Before that Cooper had already shown that in the presence of a Fermi sea any attractive interaction, no matter how weak, suffices for the formation of pairs between fermionic particles.

Electrons are fermions, i.e., particles with half-integer spin. When discovering superconductivity, Kamerlingh Onnes was also the first to observe a superfluid of fermions. Inside a superfluid non-dissipative flow can exist. In the superconductor this flow is an electric current, since electrons have charge. This Thesis deals with the phenomenon of superfluid phases inside atomic fermionic mixtures. Here, the fermionic particles are not electrons, but neutral atoms with half-integer spin. Specifically, we focus on mixtures of the alkali atoms lithium and potassium.

A Cooper pair usually consists of two particles with opposite spin. In the mercury wire used by Kamerlingh Onnes all spin states were equally occupied and all electrons were able to pair up with an other electron to form a Cooper pair. In experiments with alkali atoms it is possible to control the occupation of the different spin states and to study the influence of a spin imbalance on the phase transition from a normal gas to a superfluid phase [3, 4]. It was found

experimentally in a spin-polarized mixture of lithium atoms that a superfluid phase can still occur in the presence of a spin imbalance, although the critical temperature decreases with increasing polarization. For too large spin imbalances the transition to a superfluid does not take place and the fermionic mixture remains a normal gas at all temperatures.

In the field of ultracold atoms it recently became possible to experimentally explore another interesting possibility. Namely, two different species of fermionic alkali atoms, ^6Li and ^{40}K , have been trapped together [5, 6]. This motivated us to study also the influence of a mass imbalance on the phase transition to a superfluid of Bose-Einstein-condensed Cooper pairs, where a Cooper pair now consists of two atoms of different fermionic species. We find that in this mixture a transition to a superfluid phase can still occur, although the critical temperatures are lower as compared to the spin-polarized ^6Li mixture. For a majority of ^{40}K atoms we even find that an exotic type of superfluid can form. Namely, a superfluid phase that also shares properties of a solid and which is therefore called a supersolid.

1.1 Ultracold atoms

A major breakthrough in the field of ultracold atoms was the realization of a Bose-Einstein condensate in 1995 in a weakly interacting gas of alkali atoms, in particular rubidium, lithium and sodium atoms [7–9], after which the field grew rapidly. The phenomenon was predicted already in the 1920’s by Albert Einstein [10], but could only be realized in weakly interacting systems decades later after a number of experimental developments, of which the discovery of laser cooling probably was the most important [11]. In a Bose-Einstein condensate (BEC) all bosonic particles are in the same single-particle quantum state. One of the consequences of this macroscopic occupation of one single-particle quantum state is the disappearance of dissipation inside the BEC, very much comparable to the vanishing of electrical resistance inside a superconductor. Already in 1938 frictionless flow was observed in the strongly interacting bosonic liquid ^4He [12, 13] and shortly after this discovery the link with Bose-Einstein condensation was made [14]. However, the presence of a macroscopic occupation of a single-particle state has never been observed in this system.

In the alkali atom experiments, the BEC state is realized by trapping a very dilute gas in an ultra-high vacuum and then cooling it down to temperatures in the nanoKelvin regime. At these low temperatures where the transition from a normal gas to a Bose-Einstein condensate occurs. The gas has to be dilute in order to prevent a transition to a fluid or solid phase to occur before the condensate

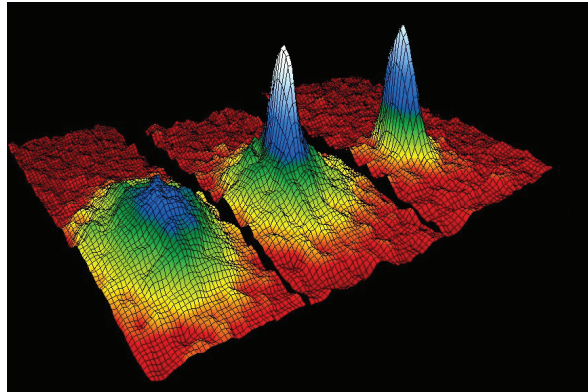


Figure 1.1: The velocity distribution of a cloud of ultracold bosons. On the left the distribution is shown just before the appearance of the condensate. For this temperature the velocity distribution is isotropic. In the middle picture the temperature is just below the condensation temperature, whereas on the right the temperature is even lower and a nearly pure condensate is left. The velocity distribution of the atoms inside the BEC is anisotropic and reveals the shape of the trap, whereas the distribution of the atoms in the thermal cloud is still isotropic. Picture taken from www.bec.nist.gov/gallery.html [7].

phase is reached. To reach these extremely low temperatures the gas is trapped by a combination of magnetic and electrical fields [15]. The microKelvin regime can be reached by laser cooling, after which the nanoKelvin regime is reached by evaporative cooling [16]. The phase transition to the BEC state takes place when de Broglie wavelength Λ of the atoms is of the same order of magnitude as the average interparticle distance, which is $n^{-1/3}$ for a gas with density n in three dimensions. The de Broglie wavelength is given by $\Lambda = (2\pi\hbar/mk_B T)^{1/2}$ with m the mass of the atom and T the temperature. In other words, a BEC occurs when the phase-space density $\Lambda^3 n$ is approximately one. Therefore, in the alkali atom experiments where the densities are extremely low, $n \simeq 10^{12} - 10^{15} \text{ cm}^{-3}$, extremely low temperatures are needed.

The basic idea of laser cooling is that an atom can be slowed down due to collisions with photons. During such a collision the atom absorbs the photon and its momentum is reduced in the opposite direction of the incoming photon. Later, when the atom emits the photon again, it gains momentum. Since the absorption of photons reduces the momentum in the direction of the laser beam, while the photons are emitted in a random direction, the atom is, after a number of

absorption and emission cycles, on average slowed down in the opposite direction of the laser beam. A photon is most likely to be absorbed by an atom if its energy $\hbar\omega$ matches the energy difference between the ground state $|g\rangle$ and excited state $|e\rangle$ of the atom, $E_e - E_g$. Thus, for the above scheme to work efficiently, the frequency ω of the laser light has to match this energy difference. However, in the frame of reference of a moving atom the frequency of the laser light is shifted, which is known as the Doppler effect. This Doppler shift can be taken into account, such that atoms with a velocity in the opposite direction of the laser beam absorb many photons, while atoms with a velocity in the same direction absorb less photons. By using different laser beams for the different spatial directions, the atoms can be brought to a near stand still and thus the temperature of the gas is reduced. With laser cooling the atomic gas can be cooled down to the microKelvin regime.

Contact with the walls of the vacuum chamber would immediately heat up the gas again. Therefore, the atoms are trapped in the center of the container by a combination of magnetic and optical traps. An atom experiences an energy shift in the presence of an externally applied magnetic field, the so-called Zeeman effect. The energy shift is different for atoms in a different hyperfine state, where the hyperfine structure is due to the coupling between the spin of the nucleus and the spin of the electron in the outer shell of the alkali atom. It depends on the hyperfine state whether the atomic energy increases or decreases with an increasing magnetic-field strength and thus there are high-field and low-field seeking states. Since in free space only magnetic-field minima can exist only low-field seeking states can be trapped by a magnetic trap, while by the same trap high-field seeking states are repelled. Transitions between the hyperfine states can be driven by radio-frequency (RF) radiation.

In the presence of an oscillating electric field, atoms acquire an electrical dipole moment. The induced dipole moment in turn couples to the electric field, which results in a ground-state energy shift proportional to the intensity of the field. This property can be exploited to trap atoms in electric fields, where the electric fields are created by laser light. Hence the name optical trapping. The frequency of the laser light should not be too far detuned from the optical transitions of the atom in order to induce a dipole moment. If the frequency of the laser ω_L is smaller than the frequency corresponding to the atomic transition ω_0 , it is called red-detuned and this results in an attractive trapping potential, i.e., the atom is attracted to the laser beam. For a blue-detuned laser, $\omega_L > \omega_0$, the resulting trapping potential is repulsive.

The final step in reaching Bose-Einstein condensation was further cooling of the gas by lowering the trap depth. The most energetic atoms escape now that the trap depth is lower, after which the remaining atoms re-thermalize by elastic

collisions to a lower temperature. This cooling technique is called evaporative cooling. Lowering the trap depth is most easily done in an optical trap, by just reducing the intensity of the laser light. Inside a magnetic trap evaporative cooling is realized by an RF field that induces transitions to a high-field seeking hyperfine state for the most energetic atoms, such that these atoms are no longer trapped by the magnetic trap. By evaporative cooling the nanoKelvin regime can be reached, which is the regime where the transition to a Bose-Einstein condensate takes place for the relevant low densities of interest.

The onset of Bose-Einstein condensation can be detected by doing a time-of-flight measurement. After turning off the trap the distance is measured between releasing and detecting the atoms and thus the velocity distribution of the atoms is obtained. For temperatures above the critical temperatures the atoms occupy many different quantum states and the velocity distribution is an isotropic Gaussian distribution. Below the transition temperature all atoms occupy the same quantum state, which depends on the trapping geometry. Therefore also the measured velocity distribution reflects the shape of the trapping potential and is anisotropic, see Fig. 1.1 [7]. Also, the density at each position in the trap can be obtained by making an in-situ measurement using phase-contrast imaging.

The development of all the techniques described above were necessary for the creation of the first atomic BEC in 1995. Now around 100 experimental BEC machines exist around the world. Moreover, by now Bose-Einstein condensates are also realized in many other condensed-matter systems. For instance, a BEC of exciton-polaritons, photons strongly coupled to electronic excitations, was realized in 2006 [17], a BEC of magnons, the quanta of magnetic excitations, was created also in 2006 [18] and a BEC of photons in an optical microcavity was realized in 2010 [19].

Moreover, due to the large experimental control in atomic systems, many other phenomena apart from Bose-Einstein condensation can be studied. For example, with optical traps many geometries of the trapping potential can be realized. Two counter-propagating laser beams form a standing wave that forms a periodic lattice potential for atoms, a so-called optical lattice [20]. By controlling the intensity of the light the potential barrier between the lattice sites can be tuned, independently in different spatial directions. In this manner, three-dimensional lattices can be created, but also, for instance, two-dimensional lattices or arrays of tubes. With the use of optical lattices the Bose-Hubbard model was realized in a cold atomic system and the superfluid to Mott insulator transition was observed [21, 22].

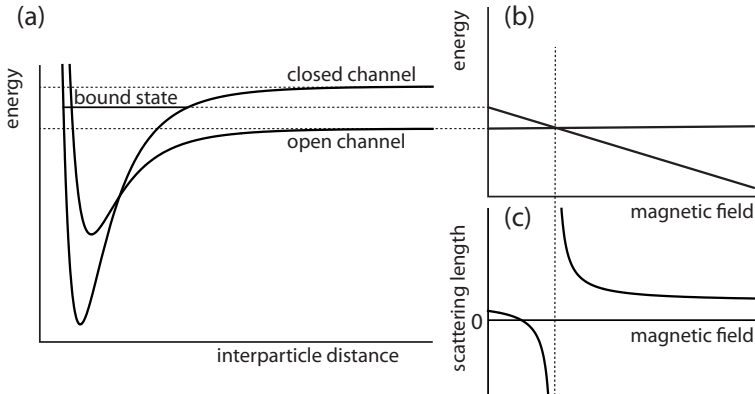


Figure 1.2: Principle of a Feshbach resonance. (a) A pair of atoms is prepared in a hyperfine state and collides through an open channel, whereas an energetically closed channel has a bound state. (b) Both the bound state and the asymptote of the open channel shift as a function of an externally applied magnetic field and for a certain magnetic field they are in resonance. (c) At this resonance the scattering length a diverges and around it all values of a can be accessed.

1.2 ${}^6\text{Li}-{}^{40}\text{K}$ mixtures

The field of ultracold fermionic gases naturally emerged out of the research performed on ultracold bosonic gases. Quantum degeneracy was achieved for the first time in 1999 in ultracold potassium [23]. A major break-through in the field of fermionic alkali atoms, was the idea of using a Feshbach resonance to control the interaction between the atoms [24–26]. This opened up the possibility to study strongly interacting Fermi mixtures and study the crossover from the weakly to the strongly interacting regime [27–32].

The scattering properties of two atoms that collide are determined by the scattering potential. In particular, the s -wave scattering length a is determined by the properties of the scattering potential. Since the initial energy of the atom pair in the initial spin configuration, defined by the hyperfine energy of the two incoming atoms at large separation r , allows for s -wave scattering this is called the open channel, see Fig. 1.2. Any scattering potential, corresponding to a different spin configuration, with a higher asymptotic energy is referred to as a closed channel. If an open and a closed channel are coupled, the presence of a bound state in the closed channel strongly influences the value of the scattering length in the open channel. Namely, the colliding atoms now form virtually a

long-lived molecule with a different spin configuration, which eventually decays into two atoms again.

Because the energies of the open and the closed channel vary differently under the influence of an applied magnetic field, the bound state in the closed channel can become resonant with the asymptotic energy of the open channel. At resonance the scattering length diverges and this phenomenon is known as a Feshbach resonance. By varying the magnetic field the scattering length can be tuned to any value and thus the effective interaction between the atoms can be tuned.

For strong attractive interactions tightly-bound molecules form, which can Bose-Einstein condense at low temperature. The size of the molecules in this so-called BEC regime is much smaller than the average interparticle distance. In the weakly interacting regime, the BCS regime, loosely bound Cooper pairs form. Here, the size of the pair is much larger than the average interparticle distance. It was shown experimentally that these two regimes are continuously connected. In the region in between, where the scattering length diverges, the pair size and interparticle distance are comparable. This is the regime we focus on in this thesis.

As mentioned early in this Introduction, for the formation of *s*-wave Cooper pairs distinguishable fermions are needed. In the case of the superconductor these were electrons in different spin states. In the BCS-BEC crossover experiments using Feshbach resonances, the distinguishable particles were alkali atoms in two different hyperfine states, while in this thesis we consider two different species of atoms, namely ${}^6\text{Li}$ and ${}^{40}\text{K}$ atoms. In both cases that use alkali atoms we still refer to the distinguishable fermions as being in different spin states. Experimentally, distinguishable fermions are also needed for evaporative cooling. Elastic collisions are needed for the rethermalization process, which can only take place between fermions in different spin states at the ultracold temperatures of interest because of the Pauli exclusion principle that forbids *s*-wave scattering for identical fermions.

Experimentally, quantum degeneracy has not been reached yet in the ${}^6\text{Li}-{}^{40}\text{K}$ mixture, but important steps have been made already. Firstly, several Feshbach resonances in the ${}^6\text{Li}-{}^{40}\text{K}$ mixture have been located and studied experimentally, [33, 34]. In particular, a broad resonance, where the effective range of the interaction is negligible, is accessible in this mixture [34]. Also expansion under the influence of strong interactions from an optical dipole trap has been realized [35] and a large atom number dual-species magneto-optical trap was built [36]. Furthermore, the impurity problem of a single ${}^{40}\text{K}$ atom immersed in a sea of ${}^6\text{Li}$ atoms, where the interactions between the impurity and the sea are strongly repulsive, has been studied [37]. In the last case, a metastable quasiparticle can form, called a repulsive polaron, and its energy and lifetime were measured.

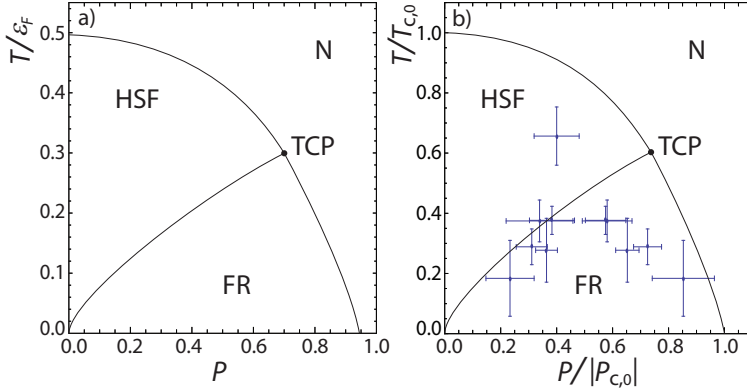


Figure 1.3: Comparison between the mean-field phase diagram and the experimental results for the population imbalanced Fermi gas. In panel (a) the mean-field phase diagram is shown as a function of the polarization $P = (n_\uparrow - n_\downarrow)/(n_\uparrow + n_\downarrow)$, with n_σ the density of the atoms in state $|\sigma\rangle$, the temperature T scaled by the Fermi temperature, $T_F = k_B\epsilon_F$. For small polarizations P a continuous phase transition from the normal gas (N) to a homogeneous superfluid (HSF) occurs, while for larger polarizations a tricritical point (TCP) is found, below which the transition is discontinuous and a forbidden region (FR) is present. In panel (b) the same phase diagram is shown, but here the temperature T is scaled by the critical temperature $T_{c,0}$ at $P = 0$ and the polarization P is scaled by the critical polarization $|P_{c,0}|$ at $T = 0$. Also shown are the data along the phase boundaries by Shin *et al.* [42], for which we used the same scaling. It can be seen that the comparison is already reasonably good.

1.3 Strong interactions and universal behavior

Presently, the understanding of strongly interacting systems is one of the key topics of both theoretical and experimental physics, since many interesting phenomena in nature originate from strong interactions. In the case of fermions examples of strongly interacting systems are high-temperature superconductors [38] and nuclear matter [39]. However, the understanding of these systems is still poor. Because of the unprecedented control in cold-atom systems they are ideal to study strongly interacting Fermi mixtures. Not only can the trapping potential and the interparticle interaction be tuned, also spin-orbit coupling can be engineered [40, 41] and the particles can be placed in an optical lattice [20]. Moreover, both homonuclear and heteronuclear systems can be studied.

In order to facilitate comparisons with other strongly interacting systems the behavior of the cold atoms has to be universal. This means that the behavior

should be independent of the specific details of the system and be solely determined by the fermionic nature of the particles and by the Fermi energy ε_F . With a Feshbach resonance the interaction can be tuned to the regime where the scattering length diverges, $1/|a| = 0$, such that it no longer sets a length scale for the system. In this so-called unitarity regime the only remaining length scale is indeed the Fermi energy $\varepsilon_F = \hbar^2 k_F^2 / 2m$, where m is twice the reduced mass of the particles $m = 2m_\uparrow m_\downarrow / (m_\uparrow + m_\downarrow)$ and k_F is the Fermi wave momentum, which is related to the density.

Apart from being very interesting, strongly interacting systems are also the most challenging theoretically. Since a small parameter is absent making use of a perturbation theory is impossible. For the weakly interacting many-body problem a mean-field approximation is the natural route to follow and it is known that it describes systems very well in that limit. For instance, critical temperatures calculated using mean-field theory are in good agreement with experiment, while in the strongly interacting regime mean-field theory overestimates critical temperatures [43, 44]. The reason for this overestimation is that mean-field theory does not incorporate all interaction effects, which become important for strong interactions.

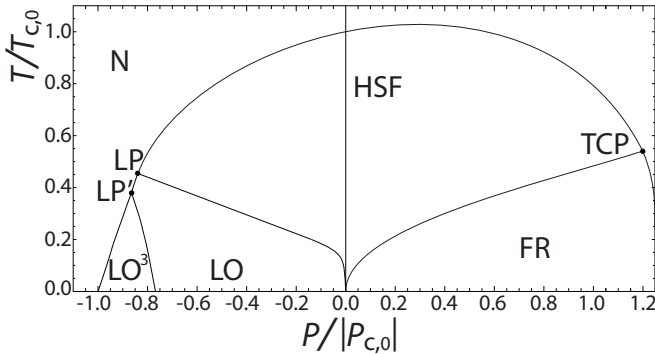


Figure 1.4: Phase diagram of the ${}^6\text{Li}-{}^{40}\text{K}$ mixture at unitarity. The same scaling for the polarization and temperature is used as in Fig. 1.3b. Here $n_\uparrow(\downarrow)$ is the density of the ${}^6\text{Li}({}^{40}\text{K})$ atoms, such that P positive(negative) means a majority of light(heavy) atoms. Apart from the phases present in the mass-balanced Fermi gas, we also find in the ${}^6\text{Li}-{}^{40}\text{K}$ mixture for a majority of ${}^{40}\text{K}$ atoms a Lifshitz point (LP), which signals the instability to an inhomogeneous phase. For larger majorities of ${}^{40}\text{K}$ atoms there is a continuous phase transition to an inhomogeneous superfluid phase where translational symmetry is broken in one spatial direction (LO) and from the point LP' on the continuous transition is to a phase where translational symmetry is broken in three directions (LO³).

There are more advanced techniques developed that do incorporate the important interaction effects such as Monte-Carlo methods [45, 46] and renormalization-group techniques [47], but they also come with their downfalls. The large disadvantage of Monte-Carlo calculations is that they are most effective for fermionic systems at zero temperatures. Moreover, Monte-Carlo techniques offer very little physical insight. Renormalization-group (RG) calculations are more intuitive and can also be performed for nonzero temperatures, but incorporating the superfluid state is very difficult and only second-order phase transitions can be determined by RG methods. Although mean-field theory does not incorporate all interaction effects as mentioned above, it has proven to be very powerful in qualitatively describing the phase diagram of the spin-polarized ^6Li mixture [48]. This qualitative success is, physically, due to the fact that even at unitarity the atomic selfenergies are well approximated by a momentum and frequency independent constant. As a result, thermodynamic instabilities are determined by mean-field-like correlation functions with strongly renormalized constants that lead to quantitative shifts only in the transition lines [47]. This is illustrated in Fig. 1.3. It can be seen that the mean-field results are in excellent qualitative agreement with the experimental results. When the same scaling is used for the mean-field results and the experimental data, the agreement is also quantitatively reasonably good.

A large part of the work presented in this thesis involves results obtained using mean-field theory, which is, for the reasons described above, a good starting point to explore the superfluid phases that can occur in the $^6\text{Li}-{}^{40}\text{K}$ mixture and map out the phase diagram.

1.4 Transport

Transport properties are intimately linked to the phase of a system. For example, the electrical resistance, the transport coefficient relating the applied voltage and the current, is nonzero above the critical temperature whereas it vanishes at the transition to the superconducting phase. Actually, already above the transition temperature the electrical resistance is influenced by the presence of the phase transition. The behavior of transport coefficients can be a precursor for a phase transition, which is an important motivation to study transport properties.

In ultracold atoms the transport coefficient of most interest is the drag resistivity. If a collection of particles is set to motion, which interacts with a second collection of particles, momentum exchange takes place between the two collections due to the interactions. As a consequence the momentum of the first collection

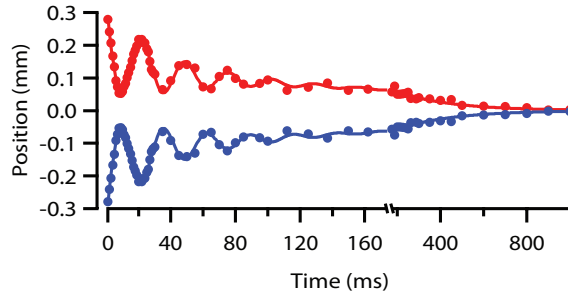


Figure 1.5: The center-of-mass motion of the spin up (red) and spin down (blue) clouds with respect to the center of the trap from Sommer *et al.* [49].

decreases, while the second collection is now also set to motion. The drag resistivity is the measure for the efficiency of this exchange in momentum.

In 2011 the drag was measured in an ultracold Fermi gas for the first time in the group of Zwierlein [49], see Fig. 1.5. A Fermi mixture is created with an equal occupation of two spin states, referred to as spin up (red) and spin down (blue). The two clouds are separated and displaced from the center of the trap and then released. The clouds first bounce off each other several times. Eventually the two clouds relax back to their equilibrium position.

Spin drag in a Bose gas was measured for the first time in 2012 in the group of Van der Straten [50]. It was found by lowering the temperature that the spin drag is enhanced in the quantum regime. This is due to Bose stimulation, which was also predicted theoretically [51].

In the fermion experiment described above the fermionic particles are all of the same species. We calculate in Chapter 2 of this thesis the drag resistivity of a single heavy(light) atom moving through a Fermi sea consisting of light(heavy) atoms.

1.5 Phase transitions and long-range order

Phases can often be characterized by the amount of order present in that phase. Namely, a phase transition is often a transition between an ordered and a disordered phase, which resulted in the concept of an order parameter to distinguish two phases phenomenologically. For instance, in an ordinary liquid no long-range order exists. Which means that at large separations the positions of particles are uncorrelated, whereas at small separations these positions may be correlated.

Short-range order can exist in liquids. If a phase transition occurs from a liquid phase to a solid, this changes drastically. In a solid all particles are ordered in a crystalline structure and once the positions of the particles are known at one point, the position of each particle is known throughout the crystal. In other words, a solid phase does exhibit long-range order. This long-range order shows itself in the diagonal parts, i.e., $\mathbf{r}_1 = \mathbf{r}_2$, of the one-particle density matrix

$$n^{(1)}(\mathbf{r}_1, \mathbf{r}_2, t) = \langle \hat{\Psi}^\dagger(\mathbf{r}_2, t) \hat{\Psi}(\mathbf{r}_1, t) \rangle, \quad (1.1)$$

where $\hat{\Psi}^\dagger(\mathbf{r}, t)$ is the operator creating a particle at time t at position \mathbf{r} , while $\hat{\Psi}$ is the annihilation operator.

In a Bose-Einstein condensate there is also long-range order present [52]. But now the off-diagonal instead of the diagonal elements of the one-particle density matrix $n^{(1)}$ are non-vanishing for large particle separations. Therefore, it is said that a BEC exhibits off-diagonal long-range order. This order makes the Bose-Einstein condensed gas behave very different from ordinary phases of matter. In particular, this many-body state results in the possibility of frictionless flow, i.e., superfluidity.

A supersolid is defined as a phase having both non-vanishing diagonal and off-diagonal elements in the one-particle density matrix. In other words, a supersolid is a state of matter with both crystalline ordering and superfluid properties. Although it is claimed that evidence of the presence of a supersolid phase in ${}^4\text{He}$ has been observed [53, 54], it is not clear yet that this phase is indeed a supersolid [55, 56].

In Fermi systems not the fermionic particles, but rather the Cooper pairs Bose-Einstein condense. Thus, the long-range order in this phase does not show itself in the one-particle density matrix, but in the density matrix corresponding to the pairs, i.e., the two-particle density matrix

$$n^{(2)}(\mathbf{r}_1, \mathbf{r}_2, t) = \langle \hat{\Psi}_\uparrow^\dagger(\mathbf{r}_2, t) \hat{\Psi}_\downarrow^\dagger(\mathbf{r}_2, t) \hat{\Psi}_\downarrow(\mathbf{r}_1, t) \hat{\Psi}_\uparrow(\mathbf{r}_1, t) \rangle, \quad (1.2)$$

where $\hat{\Psi}_\uparrow^\dagger(\mathbf{r}_2, t) \hat{\Psi}_\downarrow^\dagger(\mathbf{r}_2, t)$ creates a pair [57]. If a phase transition has occurred from a normal gas of fermionic particles to a phase of Bose-Einstein-condensed Cooper pairs, the off-diagonal elements are nonvanishing for $|\mathbf{r}_1 - \mathbf{r}_2| \rightarrow \infty$. Just as in the bosonic case this can result in properties such as superfluidity, and in the case of a superconductor it leads to the disappearance of electrical resistance.

In this thesis we investigate the possibility of having a phase where this two-particle density matrix $n^{(2)}$ has both diagonal, crystalline order, and off-diagonal elements that do not vanish for $|\mathbf{r}_2 - \mathbf{r}_1| \rightarrow \infty$. Although such a phase does not obey the definition of the bosonic supersolid, since here the two-particle instead

of the one-particle density matrix exhibits long-range order, this state is indeed a supersolid. Namely, this state of matter exhibits both superfluid properties as well as crystalline order.

1.6 Outline

In Chapter 2 we deal with the extremely imbalanced Fermi gas at unitarity. We study the behavior of a single heavy(light) atom immersed in a non-interacting sea of light(heavy) atoms with which it interacts strongly. We show that a quasiparticle forms, called the spin polaron, and determine its mass and energy for the two different cases. In Chapter 3 we study phase transitions in the mass-imbalanced Fermi mixtures. In particular, we show that the phase diagram of the ${}^6\text{Li}-{}^{40}\text{K}$ mixture contains an instability towards an inhomogeneous superfluid phase, a so-called Lifshitz point. In Chapter 4 we study this inhomogeneous superfluid phase in detail and show that the inhomogeneous superfluid is actually a supersolid. We investigate which supersolid phases are present in the ${}^6\text{Li}-{}^{40}\text{K}$ mixture or, in other words, which crystalline structures the superfluid exhibits.

C HAPTER 2

Polarons in extremely polarized Fermi gases

Abstract — We study the extremely polarized two-component Fermi gas with a mass imbalance in the strongly interacting regime.¹ Specifically we focus on the experimentally available mixture of ⁶Li and ⁴⁰K atoms. In this regime spin polarons, i.e., dressed minority atoms, form. We consider the spectral function for the minority atoms, from which the lifetime and the effective mass of the spin polaron can be determined. Moreover, we predict the radio-frequency (RF) spectrum and the momentum distribution for the spin polarons for experiments with ⁶Li and ⁴⁰K atoms. Subsequently we study the relaxation of the motion of the Fermi polaron due to spin drag.

2.1 Introduction

In many condensed-matter systems the response to a single impurity determines the low-temperature behavior of the system. Probably the most famous example hereof is a single electron moving in a lattice. Local lattice distortions, i.e., phonons, interact with the electron and together they form a quasiparticle that is known as the polaron because of the local change in polarization [58]. Another well-known impurity problem is that of an immobile magnetic impurity in a metal causing an enhanced resistance below a certain temperature due to the Kondo effect [59]. The multichannel version of this effect has especially received much interest in the past, because it leads to the formation of a non-Fermi liquid [60].

¹This chapter, without the appendix, is directly based on J. E. Baarsma, J. Armaitis, R. A. Duine and H. T. C. Stoof, *Polarons in extremely polarized Fermi gases: The strongly interacting ⁶Li-⁴⁰K mixture*, Phys. Rev. A **85**, 033631 (2012).

Here we study an impurity problem in a two-component atomic Fermi gas. An important motivation to use ultracold atoms is the unprecedented experimental control in these systems. They offer the interesting possibility of not only changing, for instance, particle numbers and temperature, but also the interaction strength. Via a Feshbach resonance the bare interaction can be tuned all the way from being weakly attractive (BCS-regime) to strongly attractive (BEC-regime), where in the intermediate regime the scattering length is much larger than the average interparticle distance. This so-called unitarity or strongly interacting limit, is the regime we focus on in this paper.

We consider a mixture at zero temperature consisting of two (spin)species of fermions, where there is one minority particle immersed in a non-interacting sea of majority particles. The mass-balanced Fermi gas with high spin polarization has been studied extensively, both experimentally [61–63] and theoretically [45, 64–70]. At the unitarity limit the minority particle gets dressed by a cloud of majority particles forming a quasiparticle similar to the polaron. This quasiparticle is often referred to as a spin polaron, because its formation is due to interactions between particles in different spin states, or as a Fermi polaron, because it consists of fermionic atoms. Recently, the imbalanced spin-dipole mode [63], the radio-frequency (RF) spectrum of the spin polaron [61], and its energy and effective mass [62] that are different from those of the bare minority particle, have all been measured in this case.

An intriguing new possibility for experiments is having a mass imbalance between the minority and the majority particles by mixing two different atom species. A very promising mixture in this respect is the one of ^6Li and ^{40}K atoms. These atoms together have already been trapped and cooled to quantum degeneracy [33], and moreover, several Feshbach resonances were identified [34]. Theoretically, the phase diagram of the $^6\text{Li}-^{40}\text{K}$ mixture has been determined [71, 72], and it differs greatly from the phase diagram of a spin-imbalanced mixture by having not only a superfluid but also a supersolid region, depending on the sign of the polarization. We show here that already the two limiting cases of this mixture, i.e., a single light impurity in a sea of heavy atoms and vice versa, turn out to differ qualitatively in a manner that reflects the underlying asymmetry of the phase diagram.

Indeed, in the solely spin-imbalanced case, having a $|\sigma\rangle$ or a $|-\sigma\rangle$ minority particle results in the same impurity problem, while with two different atom species there are two fundamentally different impurity problems. Thus, by introducing a mass imbalance, not only does the question whether dressed impurities still represent the ground state of the system arise, but so does the question of what is the difference between a heavy and a light impurity. Here, because the different

atom species act as a pseudospin, the same many-body mechanism causes the dressing of the minority atom as for the solely spin-imbalanced case. Therefore, we also call this quasiparticle a spin polaron. In this paper we study for the two mass-imbalanced cases both a molecular bound state and the spin polaron. We show that although it does not form the ground state, the molecular bound state virtually plays an important role in the system. In addition, we study dissipation of kinetic energy of the minority particle due to interactions with the majority cloud that lead to spin drag [73].

In this paper we consider a homogeneous gas of atoms, while experiments are always done in a trap. Still, when $1/k_F$ is much smaller than the size of the cloud, where k_F is the Fermi momentum of the majority atoms, the gas can locally be considered homogeneous and all our results apply. In this manner the appropriate averaging over the trap can be fully taken into account.

2.2 Molecular bound state

In the unitarity limit the minority particle interacts strongly with the Fermi sea of majority particles. Due to the low densities in ultracold atomic systems two-body processes represent the dominant scattering mechanism, where the minority particle can scatter off a majority particle an arbitrary number of times. Taking this into account in diagrammatic language results in an infinite sum of ladder diagrams, the so-called ladder sum. For the extremely imbalanced case at unitarity the bare interaction with the complete ladder sum added, i.e., the many-body T matrix, obeys

$$\frac{1}{T_{\mathbf{p},\hbar\Omega}} = \int \frac{d\mathbf{k}}{(2\pi)^3} \left[\frac{N(\xi_{\uparrow,\mathbf{k}}) - 1}{\hbar\Omega - \xi_{\uparrow,\mathbf{k}} - \xi_{\downarrow,\mathbf{k+p}}} - \frac{1}{2\varepsilon_{\mathbf{k}}} \right], \quad (2.1)$$

with $\hbar\mathbf{p}$ and $\hbar\Omega$ denoting the total momentum and energy of the two incoming particles, and \uparrow (\downarrow) denoting a majority (minority) particle. The distribution for the majority particles is the Fermi-Dirac function $N(x) = 1/[e^{x/k_B T} + 1]$, with T the temperature and k_B Boltzmann's constant. The distribution for a single minority atom can be taken equal to zero in the integrand. The energy of an atom in state $|\sigma\rangle$ is $\xi_{\sigma,\mathbf{k}} = \varepsilon_{\sigma,\mathbf{k}} - \mu_{\sigma}$, where $\varepsilon_{\sigma,\mathbf{k}} = \hbar^2 k^2 / 2m_{\sigma}$ and μ_{σ} are the kinetic energy and the chemical potential. The kinetic energy $\varepsilon_{\mathbf{k}} = (\varepsilon_{\uparrow,\mathbf{k}} + \varepsilon_{\downarrow,\mathbf{k}})/2$ is associated with twice the reduced mass. Throughout this paper we take μ_{\uparrow} equal to the Fermi energy ε_F , while the chemical potential of the minority atom is determined self-consistently from the self-energy [66], $\mu_{\downarrow} = \hbar\Sigma_{\downarrow}(\mathbf{0},0)$, defined later in Eq.(2.2).

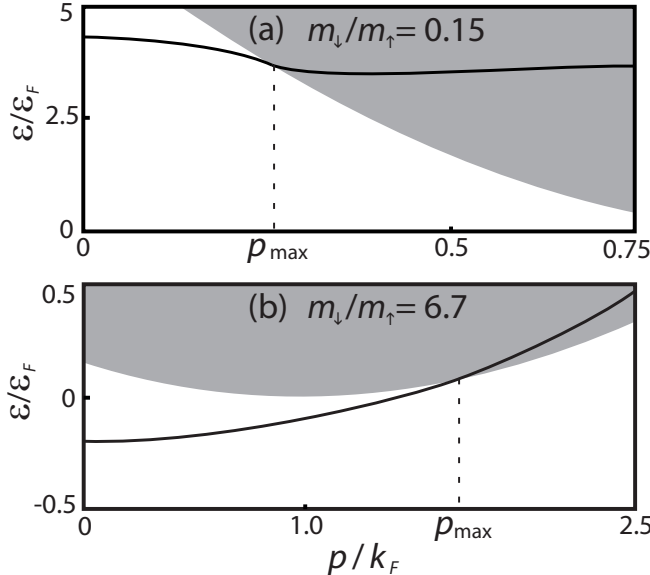


Figure 2.1: Dispersions of the molecular bound states $\varepsilon = \hbar\omega + \mu_\downarrow$ at $T = 0$, scaled by the Fermi energy $\varepsilon_F = \hbar^2(6\pi^2n_\uparrow)^{2/3}/2m_\uparrow$ of the majority cloud, as a function of the momentum $\hbar p = \hbar|\mathbf{p}|$ of the molecule, scaled by $\hbar k_F = \sqrt{2m_\uparrow\varepsilon_F}$. The grey area in both panels is the continuum of particle-particle excitations above the Fermi sea. The solid lines are the dispersions of the stable (decaying) molecular state when it lies below (in) the continuum. Panel (a) corresponds to one ${}^6\text{Li}$ atom in a sea of ${}^{40}\text{K}$ atoms, panel (b) to one ${}^{40}\text{K}$ atom in a Fermi sea of ${}^6\text{Li}$ atoms.

A pole in the T matrix corresponds to a bound state, where the real part of the location of the pole is its energy and the imaginary part is inversely proportional to its lifetime. In the above many-body T matrix the pole physically corresponds to a Feshbach molecule dressed by the Fermi sea, which we here refer to as a molecular bound state. The energy $E_M(p)$ of this bound state at zero temperature, divided by the majority particles Fermi level ε_F , is shown as a solid line in Fig. 2.1. Up to some momentum p_{\max} it is a stable molecular state, while for larger momenta the imaginary part is non-zero and thus the bound state acquires a finite lifetime. A minority and a majority atom cannot scatter off each other if their combined energy lies below a certain level due to Pauli blocking of the Fermi sea. Above this energy level there is a continuum of scattering states. This continuum of particle-particle excitations is also depicted in Fig. 2.1.

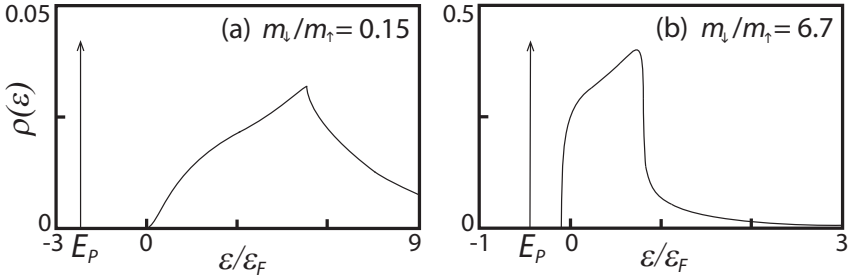


Figure 2.2: Spectral functions $\rho_{\downarrow}(\varepsilon)$ of the minority particles at zero temperature and with zero momentum as a function of the energy $\varepsilon = \hbar\omega + \mu_{\downarrow}$. Panel (a) depicts the light impurity, panel (b) the heavy impurity. The delta peak in both figures corresponds to a stable polaron with energy E_P .

From the molecular dispersions it already becomes clear that a light impurity is very different from a heavy one. Fitting the dispersion of the molecular state for small momentum to $E_M(p) = \hbar^2 p^2 / 2m_M + E_M(0)$, shows that for the light impurity the stable molecule has a negative effective mass, $m_M \simeq -0.13m_{\uparrow}$, and has an energy $E_M(0) \simeq 4.4\varepsilon_F$. The dispersion is qualitatively the same as for the mass-balanced case, where the stable molecule also has a negative mass, namely $m_M \simeq -3.9m_{\uparrow}$. In contrast to the light impurity, with a heavy impurity the stable molecular state has a positive effective mass $m_M \simeq 0.96m_{\uparrow}$ and has an energy $E_M(0) \simeq -0.2\varepsilon_F$. Interestingly, it is also the part of the phase diagram with a minority of heavy particles that differs qualitatively from the mass-balanced case and contains a supersolid phase [71, 72]. In all cases the continuum of particle-particle excitations pushes the molecular state down, which is a consequence of level repulsion as in the more simple case of an avoided crossing of two energy levels. For the light impurity this repulsion results in a negative effective mass for the molecule. For the heavy impurity the effective mass is positive, but smaller than one would obtain in the absence of the continuum.

2.3 Spin polaron

The presence of a molecular bound state does not mean necessarily that a molecule is the ground state of the system, because some other state can have a lower energy than the molecule. We therefore now consider the dressed impurity, the spin polaron, and compare its energy with the molecule to determine the ground state

of the system. The energy and lifetime of the quasiparticle can be obtained from the spectral function $\rho_{\downarrow} = -\text{Im}[G_{\downarrow}]/\pi$, where G_{\downarrow} is the Green's function describing the minority particle in the presence of the Fermi sea. To obtain the latter a self-energy is added to the bare inverse Green's function via $G_{\downarrow}^{-1} = G_{0,\downarrow}^{-1} - \Sigma_{\downarrow}$. At zero temperature and in the many-body T matrix or ladder approximation, that has been very successful for the mass-balanced case [66], we have

$$\hbar\Sigma_{\downarrow}(\mathbf{q}, \omega^+) = \int \frac{d\mathbf{k}}{(2\pi)^3} T_{\mathbf{k}+\mathbf{q}, \hbar\omega^+ + \xi_{\uparrow, \mathbf{k}}} N(\xi_{\uparrow, \mathbf{k}}), \quad (2.2)$$

with $\omega^+ = \omega + i0$. Because the relevant momentum of the minority particle at zero temperature is much smaller than the Fermi momentum of the Fermi sea, we take its momentum equal to zero first. Then the spectral function, for both impurity problems, has at the energy E_P a delta-function peak (see Fig. 2.2), which corresponds to the energy of a stable quasi-particle, i.e., the spin polaron. After comparing this energy with the energy of the molecular state $E_M(0)$ we conclude that for both cases the quasi-particle has lower energy and thus forms the ground state of the system.

Apart from the energy of the dressed particle, also the quasi-particle residue Z_P and the effective mass m^* can be determined from the spectral function. The quasi-particle residue is the weight of the delta peak and the effective mass can be obtained from the momentum dependence of its location. For the light polaron, a dressed ${}^6\text{Li}$ atom, we find $E_P \simeq -2.2\varepsilon_F$, $Z_P \simeq 0.8$ and $m^* \simeq 1.25m_{\downarrow}$, while for the dressed ${}^{40}\text{K}$ atom $E_P \simeq -0.44\varepsilon_F$, $Z_P \simeq 0.64$ and $m^* \simeq 1.16m_{\downarrow}$. The energies and effective masses are in good agreement with previous theoretical results and Monte-Carlo calculations [66, 74] that do not consider the full spectral function.

The presence of the molecular pole is very important for the spectral functions $\rho_{\downarrow}(\mathbf{k}, \omega)$. In particular, the threshold of the continuum of $\rho_{\downarrow}(\mathbf{0}, \omega)$ is at zero energy when the molecular state always has a positive energy, as for the light impurity, see Fig. 2.2(a). In contrast, for the heavy impurity the molecular state can have a negative energy and this causes the threshold of the continuum to lie at a negative energy, see Fig. 2.2(b). The spectral function at zero temperature can be approximated by $\rho_{\downarrow}(\mathbf{k}, \omega) \simeq Z_P \delta(\varepsilon_{\mathbf{k}}^* + E_P - \mu_{\downarrow} - \hbar\omega)$, with $\varepsilon_{\mathbf{k}}^* = \hbar^2 k^2 / 2m^*$. For both impurity problems, however, it does not capture all the features of $\rho_{\downarrow}(\mathbf{k}, \omega)$, as we will see next.

A direct probe for the quasiparticle residue Z_P is the momentum distribution of the minority particles, which can be obtained experimentally by a time-of-flight experiment. From the spectral function it can be calculated by means of $N_{\downarrow}(k) = \int d\omega \rho_{\downarrow}(k, \omega) N(\omega)$. In Fig. 2.3 the results are shown, both for the full spectral function and for the delta peak only, at zero temperature and for polarization

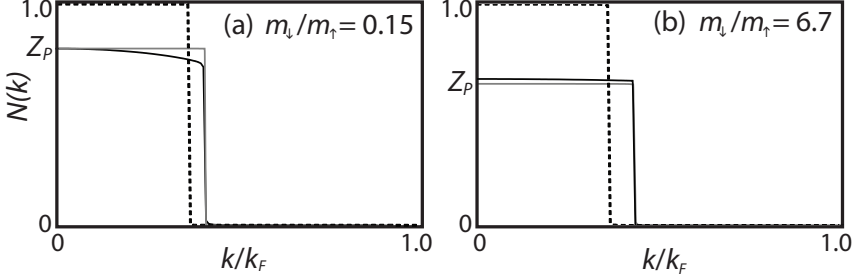


Figure 2.3: Momentum distributions $N(k)$ for the spin polarons at zero temperature and $P = 0.9$, where the polarization $P = (n_\uparrow - n_\downarrow)/(n_\uparrow + n_\downarrow)$. The solid, black (gray) lines are the momentum distributions of the polarons obtained from the full (delta-peak) spectral function, while the dashed lines are the distributions for an ideal gas. Panel (a) depicts the light spin polaron and panel (b) the heavy one.

$P = 0.9$. Also depicted are the ideal gas momentum distributions for comparison. The quasiparticle residue can be read off easily in both figures. It can also be seen that the delta peak is a good approximation for the heavy impurities, while for the light impurities Z_P depends more strongly on the external momentum, which is not captured by this approximation.

The energy of the spin polaron can be directly obtained from the RF spectrum, which was recently measured for the mass-balanced case. In an RF experiment incoming photons with frequency ω_{rf} induce transitions from an occupied hyperfine state to an empty state. The fraction of transferred atoms as a function of the photon frequency is the RF spectrum, where the threshold of the spectrum is the polaron energy. Theoretically, the spectrum can be obtained directly from the spectral function by using the Kubo formula, $I(\omega_{rf}) \propto \int d\mathbf{k}N(\xi_{\downarrow,\mathbf{k}} - \hbar\omega_{rf})\rho_{\downarrow}(\mathbf{k}, \xi_{\downarrow,\mathbf{k}} - \hbar\omega_{rf})$ [75]. When using the low-temperature spectral function the integral can be performed, yielding

$$I(\omega_{rf}) \propto Z_P \sqrt{2(\omega_{rf} + E_P)} N \left(\frac{m_\downarrow \omega_{rf} + m^* E_P}{m^* - m_\downarrow} \right). \quad (2.3)$$

The RF spectra for the two mass-imbalanced impurity problems are shown in Fig. 2.4 for $P = 0.99$ and the temperature of the experiment with mass balance, $T = 0.14T_F$ [61]. For the light impurity the analytic result from Eq. (2.3) reproduces the full spectral function result almost exactly.

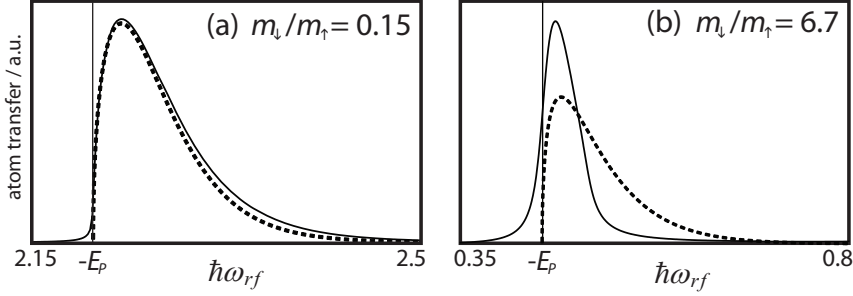


Figure 2.4: RF spectra at $T = 0.14T_F$ and polarization $P = 0.99$ in arbitrary units. The solid lines are obtained from the full spectral functions, the dashed line from Eq. (2.3). In panel (a) the results for the light impurity are depicted and in panel (b) for the heavy impurity.

2.4 Spin-drag relaxation rate

At zero temperature the spin polaron corresponds to a delta-function peak in the spectral function as we have just seen. At nonzero temperatures we expect this peak to broaden and to obtain a width that is proportional to T^2 at low temperatures. An immediate consequence of this non-zero width is that the polaron acquires interesting transport properties. In particular it leads to a non-zero spin-drag relaxation rate $1/\tau_{sd}$ of the polaron moving in a Fermi sea of majority particles. The friction of the spin polaron and the out-of-phase dipole mode are examples of properties determined by $1/\tau_{sd}$. For the mass-balanced case the latter has been studied experimentally [62, 63], and the transport properties of the mass-imbalanced impurity problem have been studied theoretically using thermodynamic arguments to calculate the effective interaction [73].

We derive here a general expression for the relaxation rate of one polaron moving with velocity \mathbf{v} through a cloud of majority particles with which it interacts, where its velocity is small compared to the Fermi velocity of the majority particles $|\mathbf{v}| \ll k_F/m_\uparrow \hbar$. The equation of motion of the spin polaron then reads

$$\frac{d\mathbf{v}}{dt} = \frac{Z_P}{m^* n_\downarrow} \mathbf{\Gamma}(\mathbf{v}) \simeq -\frac{\mathbf{v}}{\tau_{sd}}, \quad (2.4)$$

where $\mathbf{\Gamma}(\mathbf{v})$ is the Boltzmann collision integral, which was linearized in the last step. For the spin-drag relaxation rate for the impurity problem we obtain in this

manner

$$\frac{1}{\tau_{sd}} = \frac{-\beta\hbar}{6m^*(2\pi)^6} \int d\mathbf{q} dk q^2 \frac{(|V_{\mathbf{k},\mathbf{0},\mathbf{q}}|^2 + |V_{\mathbf{k},-\mathbf{q},\mathbf{q}}|^2)}{\sinh^2(\beta\varepsilon_{\mathbf{q}}^*/2)} \\ \times \text{Im} \left[\frac{N_{\uparrow}(\mathbf{k}) - N_{\uparrow}(\mathbf{k} - \mathbf{q})}{\varepsilon_{\mathbf{q}}^* - i0 + \varepsilon_{\uparrow,\mathbf{k}} - \varepsilon_{\uparrow,\mathbf{k}-\mathbf{q}}} \right], \quad (2.5)$$

where β is $1/k_B T$ and $N_{\uparrow}(\mathbf{k})$ is the distribution function of the majority particles. The on-shell effective interaction $V_{\mathbf{k},\mathbf{k}',\mathbf{q}}$ in general depends on the incoming momenta \mathbf{k} and \mathbf{k}' and on the transferred momentum \mathbf{q} of the scattering particles. From the linearized collision integral, the above expression is obtained by using as the distribution function for the dressed impurity a delta function. The result in Eq. (2.5) is generic for any impurity, fermionic or bosonic, in any environment, fermionic or bosonic.

In the impurity problem at hand we take for $N_{\uparrow}(\mathbf{k})$ the Fermi-Dirac distribution function. At low temperatures only small \mathbf{q} contribute and the difference between the two distributions becomes strongly peaked around the Fermi level [51]. For the interaction we take the many-body T matrix from Eq. (2.1), with an additional factor Z_P to account for the wavefunction renormalization, and then ultimately obtain

$$\frac{1}{\tau_{sd}} \sim \frac{\beta m_{\uparrow}^2}{12\pi\hbar m^{*2}(2\pi)^3} \frac{Z_P^2}{|T(k_F, \varepsilon_F)|^2} \int d\mathbf{q} \frac{q^3}{\sinh^2(\beta\varepsilon_{\mathbf{q}}^*/2)} \\ = \gamma \left(\frac{m_{\downarrow}}{m_{\uparrow}} \right) \frac{\varepsilon_F}{\hbar} \left(\frac{T}{T_F} \right)^2, \quad (2.6)$$

where $\gamma(m_{\downarrow}/m_{\uparrow})$ is a dimensionless function depending on the mass ratio of the minority and majority particles. For the light impurity we find $\gamma(0.15) \simeq 8.58$, while we find $\gamma(6.7) \simeq 1.96$ for the heavy impurity. The temperature dependence for only one minority particle in a fermionic environment is the same as for the spin-drag relaxation rate for equal densities of fermions, namely $1/\tau_{sd} \propto T^2$. This quadratic temperature dependence is expected for a Fermi liquid and recently it was verified experimentally for the mass-balanced case that $1/\tau_{sd}$ indeed decreases as the temperature decreases [49, 63]. The result in Eq. (2.6) implies that at $T = 0$ there is no spin drag relaxation, which in turn implies that the spin polaron is a stable quasiparticle in that case. As mentioned above, the latter is consistent with the delta-peaks in the spectral functions in Fig. 2.4 and confirms that the ladder approximation captures the relevant physics for these mass-imbalanced mixtures.

2.5 Conclusion

We calculated a number of important observables of the extremely polarized ${}^6\text{Li}$ - ${}^{40}\text{K}$ mixture. We showed that at the unitarity limit, although virtually the molecular state plays an important role, polarons form at low temperatures and dominate all physical properties of the mixture. Apart from its equilibrium properties we also looked at the transport properties of the spin polaron and found that the spin-drag relaxation rate takes a universal form and scales with the square of the temperature, as expected for a Fermi liquid.

2.6 Appendix: Boltzmann transport theory

In Section 2.4 we calculate the spin-drag relaxation rate starting from the equation of motion of the spin polaron. In this appendix we describe how we obtain this equation of motion and we show in a bit more detail how we obtain the spin-drag relaxation rate from linearizing the Boltzmann collision integral.

A small number of spin polarons, described by the distribution $N^*(\mathbf{k}, t)$, move with velocity \mathbf{v} through an ideal gas of majority particles, described by the distribution $N_\uparrow(\mathbf{k})$, with which they interact. The Boltzmann equation for the spin polarons, in the absence of an external force, reads

$$\frac{\partial N^*(\mathbf{k}, t)}{\partial t} = \Gamma_{\text{coll}}(\mathbf{k}), \quad (2.7)$$

where Γ_{coll} is the collision integral. The above equation states that changes in the distribution of the spin polarons are due to scattering processes of the spin polarons with the majority particles. The above collision integral is given by

$$\begin{aligned} \Gamma_{\text{coll}}(\mathbf{k}) = & \frac{1}{(2\pi)^9} \int d\mathbf{k}_1 d\mathbf{k}_2 d\mathbf{k}_3 |V_{\mathbf{k}, \mathbf{k}_1, \mathbf{k}_2, \mathbf{k}_3}|^2 \left[N^*(\mathbf{k}) N_\uparrow(\mathbf{k}_1) (1 \pm N^*(\mathbf{k}_2)) (1 \pm N_\uparrow(\mathbf{k}_3)) \right. \\ & - (1 \pm N^*(\mathbf{k})) (1 \pm N_\uparrow(\mathbf{k}_1)) N^*(\mathbf{k}_2) N_\uparrow(\mathbf{k}_3) \Big] \\ & \times \delta(\mathbf{k} + \mathbf{k}_1 - \mathbf{k}_2 - \mathbf{k}_3) \delta(\varepsilon^*(\mathbf{k}) + \varepsilon_\uparrow(\mathbf{k}_1) - \varepsilon^*(\mathbf{k}_2) - \varepsilon_\uparrow(\mathbf{k}_3)), \end{aligned} \quad (2.8)$$

where the plus sign is used in the case of bosonic minority or majority atoms and the minus sign in the case of fermions. The momentum balance for the spin polaron is obtained from Eq. (2.7) by multiplying it by $\hbar\mathbf{k}$ and integrating

$$\int d\mathbf{k} \hbar \mathbf{k} \frac{\partial N^*(\mathbf{k}, t)}{\partial t} = \int d\mathbf{k} \hbar \mathbf{k} \Gamma_{\text{coll}}(\mathbf{k}), \quad (2.9)$$

where the right-hand side is the definition of $\Gamma(\mathbf{v})$. For the distribution of the spin polarons we use the distribution of the minority particles, where we replace the

mass of the minority particles by the effective mass of the quasiparticles, displaced with a drift velocity $\mathbf{v}(t)$ and divided by the quasiparticle residue,

$$N^*(\mathbf{k}, t) = \frac{1}{Z_P} N_\downarrow \left(\mathbf{k} - \frac{m^* \mathbf{v}(t)}{\hbar} \right). \quad (2.10)$$

The left-hand side of Eq. (2.9) becomes after plugging in this distribution

$$\begin{aligned} \frac{d}{dt} \int d\mathbf{k} \hbar \mathbf{k} \frac{N_\downarrow(\mathbf{k} - m^* \mathbf{v}(t)/\hbar)}{Z_P} &= \frac{d}{dt} \int d\mathbf{k}' \hbar \left(\mathbf{k}' + \frac{m^* \mathbf{v}(t)}{\hbar} \right) \frac{N_\downarrow(\mathbf{k}')}{Z_P} \\ &= \frac{m^*}{Z_P} \frac{d\mathbf{v}}{dt} \int d\mathbf{k}' N_\downarrow(\mathbf{k}') = \frac{n_\downarrow m^*}{Z_P} \frac{d\mathbf{v}}{dt} \end{aligned} \quad (2.11)$$

and by dividing both sides of the momentum balance by $n_\downarrow m^*/Z_P$ now Eq.(2.4) is obtained. We linearize the collision integral, $\Gamma(\mathbf{v}) \equiv \Gamma_s \mathbf{v}$, by expanding N^* in the drift velocity and collecting all terms linear in \mathbf{v} . The spin-drag relaxation rate τ_{sd} is inversely proportional to Γ_s , which we used in Eq.(2.4), given by

$$\begin{aligned} \Gamma_s &= \frac{2\pi\beta\hbar}{3} \frac{1}{(2\pi)^9} \int d\mathbf{k} d\mathbf{k}' d\mathbf{q} q^2 \delta(\varepsilon^*(\mathbf{k}) + \varepsilon_\uparrow(\mathbf{k}') - \varepsilon^*(\mathbf{k}' + \mathbf{q}) - \varepsilon_\uparrow(\mathbf{k} - \mathbf{q})) \\ &\quad \times |V_{\mathbf{k}, \mathbf{k}', \mathbf{q}}|^2 N^*(\mathbf{k}) N_\uparrow(\mathbf{k}') (1 - N^*(\mathbf{k}' + \mathbf{q})) (1 - N_\uparrow(\mathbf{k} - \mathbf{q})), \end{aligned} \quad (2.12)$$

where $\hbar\mathbf{k}$ and $\hbar\mathbf{k}'$ are the incoming momenta and $\hbar\mathbf{q}$ is the transferred momentum. One momentum integral we performed using the momentum-conserving Dirac delta function. In the above expression we can replace the spin polaron distributions $N^*(\mathbf{k})$ by Kronecker delta's $\delta_{\mathbf{k}, \mathbf{0}}$, since we assume a single spin polaron moving through the majority particles. Then, after using the Dirac identity, $\text{Im}[1/(x + i0)] = -\pi\delta(x)$, we arrive at Eq. (2.5).

C HAPTER 3

Population and mass imbalance in atomic Fermi gases

Abstract — We develop an accurate theory of resonantly interacting Fermi mixtures with both spin and mass imbalance.¹ We consider Fermi mixtures with arbitrary mass imbalances, but focus in particular on the experimentally available ${}^6\text{Li}$ - ${}^{40}\text{K}$ mixture. We determine the phase diagram of the mixture for different interaction strengths that lie on the BCS side of the Feshbach resonance. We also determine the universal phase diagram at unitarity. We find for the mixtures with a sufficiently large mass imbalance, that includes the ${}^6\text{Li}$ - ${}^{40}\text{K}$ mixture, a Lifshitz point in the universal phase diagram that signals an instability towards a supersolid phase.

3.1 Introduction

Ultracold quantum gases of fermionic atoms are at the center of attention of both experimental and theoretical physicists. Because of the amazing experimental control in these gases they offer the possibility to experimentally explore various pairing phenomena. As a result, many fundamental discoveries have already been made, for example the realization of the crossover from a Bardeen-Cooper-Schrieffer (BCS) superfluid of loosely bound Cooper pairs to a Bose-Einstein condensate (BEC) of tightly bound molecules, also called the BEC-BCS crossover

For high- T_c superconductors, the size of a Cooper pair is comparable to the average distance between the electrons. This is analogous to the intermediate regime in the BEC-BCS crossover. In the BCS regime, the distance between two particles making up a Cooper pair is much larger than the average distance

¹This chapter is directly based on J. E. Baarsma, K. B. Gubbels and H. T. C. Stoof, *Population and mass imbalance in atomic Fermi gases*, Phys. Rev. A **82**, 013624 (2010).

between particles, whereas in the BEC regime the distance between particles within a pair is much smaller than the average interparticle distance. If the size of a pair can be manipulated, it is possible to go smoothly from one regime to the other. This manipulation can be achieved in an atomic Fermi gas, where the interaction strength between the atoms in the two different spin states can be controlled with a Feshbach resonance. The smooth BEC-BCS crossover was eventually realized in a trapped gas of ^{40}K [27] and ^6Li atoms [28–32].

For a Fermi mixture pairing is always possible for an equal amount of particles in each spin state. However, pairing is absent for the noninteracting system with all particles in one spin state. Therefore, as a function of population imbalance there must exist a phase transition at low temperatures. Experimentally, this transition was studied for the strongly interacting and mass-balanced case [3, 76], and the phase diagram was found to be governed by a tricritical point that resulted in the observation of phase separation [42, 76]. Sarma superfluidity is also likely to be present in this system [48, 77], but has not been unambiguously identified yet.

Besides an imbalance in the particle densities, there can also be an imbalance between the masses of the particles. Consequences of these imbalances are interesting to study, also because imbalanced Fermi mixtures exist in certain condensed-matter systems in a magnetic field, in nuclear matter, and even in the quark-gluon plasma that is supposed to be present in the core of heavy neutron stars [39, 78].

While studying mass-imbalanced Fermi mixtures, we first focused on the mixture with a mass ratio of 6.7, corresponding to a $^6\text{Li}-^{40}\text{K}$ mixture. This resulted in a Letter [71] where we presented the phase diagram of this mixture as a function of polarization and temperature in the strongly interacting limit, or the so-called unitarity limit, where the scattering length of the interparticle interaction diverges. In the unitarity limit, the size of the Cooper pairs is comparable to the average interparticle distance and the pairing is a many-body effect. As a result, the mass imbalance has profound effects on the pairing, because the imbalance strongly affects the two Fermi spheres that are present in the system. We showed that the phase diagram of the $^6\text{Li}-^{40}\text{K}$ mixture contains a Lifshitz point for a majority of heavy fermions [71]. Typically, Lifshitz points are found at weak interactions where the critical temperatures are very low. However, we found that in the strongly interacting limit the phase diagram of the $^6\text{Li}-^{40}\text{K}$ mixture already contains a Lifshitz point at accessible temperatures, see Fig. 3.17 below. At a Lifshitz point the phase transition undergoes a dramatic change of character. Rather than preferring a homogeneous order parameter, the system now forms an inhomogeneous superfluid.

The possibility of an inhomogeneous superfluid was early investigated by Larkin

and Ovchinnikov (LO), who considered a superfluid with a single standing-wave order parameter [79], which is energetically more favorable than the plane-wave case studied by Fulde and Ferrell (FF)[80]. Since the LO phase results in periodic modulations of the particle densities, it is a supersolid [81]. The FF and LO phases have intrigued the condensed-matter community for many decades, but only very recently strong evidence for the FFLO phase has been obtained in a one-dimensional imbalanced Fermi mixture of two spin states [82]. Theoretically, it is challenging to describe the phase diagram below a Lifshitz point. The most stable states are likely to be complicated superpositions of standing waves, where different ansatzes lead to different stability regions [83, 84].

Initially, our focus was on the ${}^6\text{Li}-{}^{40}\text{K}$ mixture, because this is experimentally a very promising mixture, where several accessible Feshbach resonances are identified [5] and both species have also been simultaneously cooled into the degenerate regime [6]. In contrast to our previous work, we now consider Fermi mixtures with an arbitrary mass ratio. Moreover, apart from the unitarity limit, we also cover the BCS regime. We do not calculate phase diagrams on the BEC side of the Feshbach resonance, because in that regime we should include thermal molecules in our calculations, which requires a different theory. Due to the population and the mass imbalance, the two Fermi spheres in the system are typically mismatched, which can induce phase separation with the location of the tricritical point depending on the mass ratio and the interaction strength [85]. In this paper, we also consider Lifshitz instabilities and also find a multicritical point for the mass-balanced case at a very weak interaction, as shown in Fig. 3.13. At this interaction strength the Lifshitz point and the tricritical point occur for the same polarization and temperature. Furthermore, in the imbalanced Fermi mixture the quasiparticle dispersions in the superfluid phase also give rise to gapless Sarma superfluidity. For the mass-balanced Fermi mixture and for the ${}^6\text{Li}-{}^{40}\text{K}$ mixture we therefore also calculated the regions in the phase diagrams where the superfluid is gapless.

In our Letter [71], we showed that although mean-field theory vastly overestimates critical temperatures in the unitarity limit, it is very useful for a qualitative description of the physics. From the mass-balanced case, we know that the critical temperatures found using mean-field techniques are lowered mainly by two effects, namely the fermionic selfenergies and the screening of the interaction due to particle-hole fluctuations [43, 47]. After discussing mean-field theory for the imbalanced Fermi gases, we take both these effects into account in the unitarity limit for the mass-balanced case and for the experimentally interesting case of the ${}^6\text{Li}-{}^{40}\text{K}$ mixture. This leads to results that compare well with Monte Carlo calculations [46] and for equal masses also with experiment [42]. Our procedure gives a reduction of the mean-field critical temperatures by a factor of 3. This makes it experimentally

more difficult, but not impossible, to reach also for the mass-imbalanced case the superfluid regime. Very importantly, the Lifshitz point remains present in the phase diagram after taking fluctuations into account. This hopefully brings the observation of inhomogeneous superfluidity within experimental reach.

This paper is organized as follows. We start with discussing the interactions in Fermi mixtures in Sec. II. In Sec. III, we give a brief discussion of the Landau theory that we use to describe phase transitions. In particular, we introduce the Landau thermodynamic potential and the order parameter. Next, in Sec. IV, we discuss the mean-field theory that we use to calculate phase diagrams, which are presented in Sec. IVC. We discuss the phase diagrams for three different mass ratios at different interaction strengths, to explore the various topologies of the phase diagrams that can arise. After that, we discuss in more detail the effects of the mass imbalance. We then also explore the effect of the interaction strength on the position of the tricritical points and Lifshitz points in the phase diagram. Subsequently, we discuss the presence of the superfluid Sarma phase for the mass-balanced case and the ${}^6\text{Li}$ - ${}^{40}\text{K}$ mixture, both at unitarity. All these calculations use in first instance mean-field theory. Then, in Sec. V, we include fluctuation effects to obtain more quantitative results for the mass-balanced case and the ${}^6\text{Li}$ - ${}^{40}\text{K}$ mixture. We focus here on the unitarity limit, although fluctuation effects could also be easily incorporated in the BCS limit of the Feshbach resonance. Finally, different appendices are added where more calculations can be found. In Appendix A it is explained how the thermodynamic potential for the mass-imbalanced Fermi gas is obtained, while Appendix B contains the calculations for the amplitudes of relevant Feynman diagrams.

3.2 Interactions and Feshbach resonances

In this paper we study phase transitions in an imbalanced Fermi gas at different interaction strengths. This is in particular relevant if the interaction strength is experimentally under control. In atomic Fermi mixtures the interspecies interaction can be controlled using a Feshbach resonance [86]. The effect of the microscopic interaction potential can be studied via the two-body transition operator \hat{T}^{2B} . The matrix elements of this transition operator are directly related to the scattering amplitudes. It is defined by

$$\hat{V}|\psi_{\mathbf{k}}^{(+)}\rangle \equiv \hat{T}^{2B}|\mathbf{k}\rangle, \quad (3.1)$$

where $|\psi_{\mathbf{k}}^{(+)}\rangle$ are the scattering states and \hat{V} is the microscopic interaction potential. To find an expression for \hat{T}^{2B} we start with the Lippmann-Schwinger

equation

$$\hat{T}^{2B} = \hat{V} + \hat{V} \frac{1}{z - \hat{H}_0} \hat{T}^{2B}, \quad (3.2)$$

where $z = E + i0$ and the notation $i0$ implies the limit $\varepsilon \downarrow 0$. In this paper we study an imbalanced Fermi gas with a point interaction

$$V(\mathbf{x} - \mathbf{x}') \simeq V_0 \delta(\mathbf{x} - \mathbf{x}'), \quad (3.3)$$

where V_0 is negative, since we are interested in an attractive interaction. If we now consider the Lippmann-Schwinger equation at zero energy $z = 0$, multiply both sides with $\langle \mathbf{k}' |$ from the left and with $| \mathbf{k}'' \rangle$ from the right, and we insert a completeness relation in the second term on the right-hand side, we obtain

$$\frac{1}{T^{2B}(0)} = \frac{1}{V_0} + \int \frac{d\mathbf{k}}{(2\pi)^3} \frac{1}{2\varepsilon(\mathbf{k})}, \quad (3.4)$$

where half the reduced kinetic energy, $\varepsilon(\mathbf{k}) = \hbar^2 \mathbf{k}^2 / 2m$, is the kinetic energy associated with a mass m that is equal to twice the reduced mass, namely

$$\frac{2}{m} = \frac{1}{m_\uparrow} + \frac{1}{m_\downarrow}. \quad (3.5)$$

Here, m_\uparrow and m_\downarrow are the masses of a light and a heavy particle, respectively.

The two-body transition matrix is related to the s -wave scattering length a by

$$\frac{1}{T^{2B}(0)} = \frac{m}{4\pi\hbar^2 a}. \quad (3.6)$$

Since we are interested in the behavior of the Fermi gas at ultralow temperatures, we can use a cut-off momentum $\hbar\Lambda$ to evaluate the integral in Eq. (3.4) and we obtain, using Eq. (3.6), a relation between the scattering length a and the microscopic interaction potential V_0 , namely

$$a = \frac{m\pi V_0}{2m\Lambda V_0 + 4\pi^2\hbar^2}. \quad (3.7)$$

This relation is shown in Fig. 3.1. It can be seen that for small values of V_0 the scattering length is negative, which means that the Fermi mixture is in the BCS regime. Then, for $V_0 = -(2\pi\hbar)^2/m\Lambda$ the scattering length diverges, which is called the unitarity limit. For large values of V_0 the scattering length is positive and the Fermi mixture is in the BEC regime.

For $a > 0$ the microscopic interaction has a bound state with an energy $E = -\hbar^2/ma^2$. This is the single-channel picture of a Feshbach resonance. In this paper

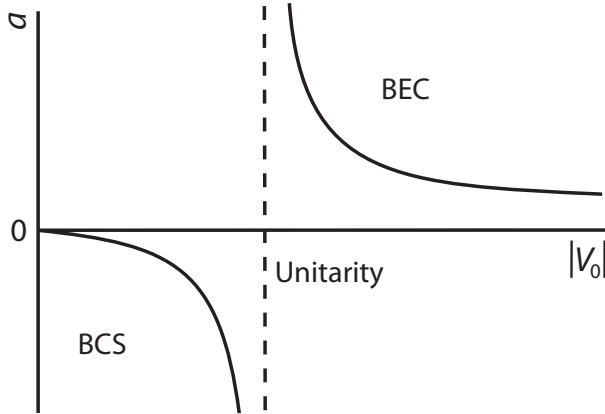


Figure 3.1: The s -wave scattering length a as a function of the microscopic interaction strength V_0 . Here V_0 is negative, since we are considering an attractive interaction.

we focus on the unitarity limit and on the BCS side of the resonance. Thus, we look at the case where a diverges and at negative scattering lengths a . For those scattering lengths we can use the single-channel picture, as long as the Feshbach resonance is sufficiently broad. Namely, in the limit of a broad resonance the amplitude to be in the bare molecular state of the Feshbach resonance turns out to be very small [28, 87].

3.3 Landau theory of phase transitions

In order to study the critical behavior of a system, in our case an imbalanced Fermi gas, we consider the Landau thermodynamic potential density $\omega_L(\Delta(\mathbf{x}))$, with $\Delta(\mathbf{x})$ the superfluid order parameter. Near the phase transition, where the BCS order parameter $\Delta(\mathbf{x})$ is small, the Landau thermodynamic potential density can be expanded as [88, 89]

$$\omega_L(\Delta; \mu_\sigma, T) = \gamma |\nabla \Delta|^2 + \alpha |\Delta|^2 + \frac{\beta}{2} |\Delta|^4 + \dots, \quad (3.8)$$

where the dots denote the higher orders in $|\Delta|^2$ and in gradients $|\nabla \Delta|^2$. The Landau coefficients in the thermodynamic potential all depend on the temperature and on the chemical potentials of the two fermion species. If in the thermodynamic potential all coefficients are positive, the minimum of the thermodynamic potential is located at $\langle \Delta(\mathbf{x}) \rangle$ equal to zero and the system will be in the normal state.

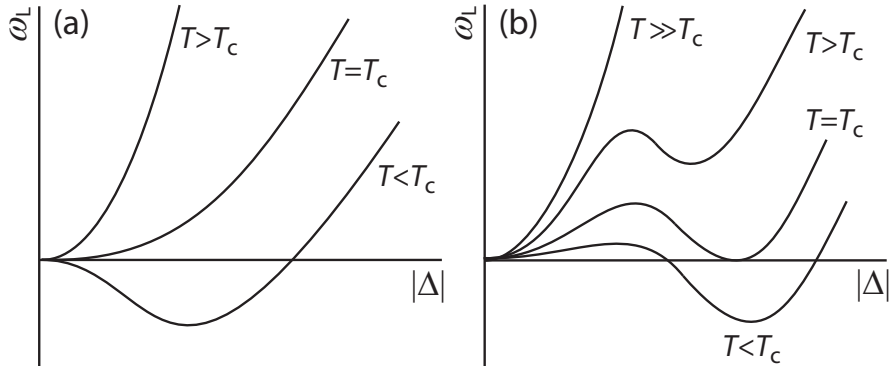


Figure 3.2: The thermodynamic potential density $\omega_L(|\Delta|)$ as a function of the order parameter Δ . Panel (a) shows the behavior of $\omega_L(|\Delta|)$ for different temperatures when a second-order phase transition occurs and panel (b) when a first-order phase transition occurs.

Whereas a phase transition to a superfluid state has occurred when the position of the global minimum is located at a nonzero order parameter $\langle \Delta(x) \rangle$, which describes a condensate of bosonic pairs. In the case that γ is positive, it costs energy to have a spatially varying superfluid. It is then energetically favorable for the system to be homogeneous and therefore we can restrict ourselves to a pairing field Δ independent of position.

We consider first the case where γ is positive and the system is homogeneous. For high temperatures all coefficients in the thermodynamic potential will be positive and the system will be in the normal state. But for low temperatures it can occur that certain coefficients change sign. Suppose that in the Landau thermodynamic potential α is negative and all other coefficients are positive. The minimum of the thermodynamic potential will then be attained at some nonzero $\langle \Delta \rangle$ and the Fermi gas will be in the superfluid state. Thus, as α changes sign a phase transition takes place. The temperature at which the transition from the normal state to the superfluid state occurs, for given chemical potentials, can be determined by equating the quadratic coefficient to zero, $\alpha(T_c) = 0$, where T_c is called the critical temperature. The phase transition just described is called a second-order phase transition and it is characterized by the fact that the minimum of the thermodynamic potential shifts away from zero continuously, see Fig. 3.2a.

It is also possible to have a first-order phase transition. To explain a first-order phase transition we consider the situation where in the thermodynamic

potential density all coefficients but the fourth-order coefficient β are positive. The thermodynamic potential will then typically have two minima. One of these is located at Δ equal to zero and the other one will be located at a nonzero value of the order parameter. For higher temperatures the minimum located at zero is a global minimum and the Fermi gas is in the normal state. If the temperature is lowered there will be a point where the two minima are equal and for even lower temperatures the minimum located at a nonzero order parameter $\langle\Delta\rangle$ is the global minimum. The system is then in the superfluid state. The first-order phase transition takes place when these two minima are equal, i.e., when $\omega_L(0) = \omega_L(\langle\Delta\rangle)$. In contrast to a second-order phase transition, the location of the global minimum of the thermodynamic potential now changes discontinuously from being zero to a nonzero $\langle\Delta\rangle$, see Fig. 3.2b.

Next, we consider the case where γ is negative. The system can then gain energy when the order parameter varies in space. Thus, instead of being constant, the order parameter will now depend on position. Fulde and Ferrell studied the plane-wave solution [80]

$$\Delta(\mathbf{x}) = \Delta_0 e^{i\mathbf{k}\cdot\mathbf{x}}, \quad (3.9)$$

while Larkin and Ovchinnikov considered a superfluid with the single standing-wave order parameter [79]

$$\Delta(\mathbf{x}) = \Delta_0 \cos(\mathbf{k} \cdot \mathbf{x}), \quad (3.10)$$

which turns out to be energetically more favorable than the plane-wave case. Superpositions of more than two plane waves are also possible.

In the LO phase the wavefunction of the bosonic pairs is periodic and therefore there will also exist a periodicity in the atomic density. This periodic structure shows itself in the diagonal elements of the one-particle density matrix $n(\mathbf{x}, \mathbf{x}')$ and is therefore called diagonal long-range order. This diagonal long-range order is what characterizes a solid. In a fermionic superfluid a fraction of the Cooper pairs is in the lowest energy eigenstate. There thus exists a long-range order between the positions of the pairs. It is also said that the two-particle density matrix $g(\mathbf{x}, \mathbf{x}')$ has off-diagonal long-range order, which implies that $g(\mathbf{x}, \mathbf{x}')$ does not vanish in the limit $|\mathbf{x} - \mathbf{x}'| \rightarrow \infty$ and characterizes a superfluid. In the case where γ is negative a transition occurs from the normal state to a superfluid where the atomic density in the superfluid has a periodic structure. Then there exists both diagonal long-range order as well as off-diagonal long-range order and the state is both solid and superfluid. This is called a supersolid phase [81, 89].

Further on, we show that in a mass-imbalanced Fermi gas not only a second-order phase transition can occur, but also a first-order transition and even a

transition to an inhomogeneous superfluid, depending on the values of the two chemical potentials. Therefore, there must be points in the phase diagram where the character of the phase transition changes. If the phase transition changes from being second order to first order there will be a tricritical point [90]. This point can thus be found by setting

$$\alpha(T_{c3}) = \beta(T_{c3}) = 0, \quad (3.11)$$

where T_{c3} is the tricritical temperature. For temperatures higher than the tricritical temperature the phase transition from the normal to the superfluid state is of second order, while for $T < T_{c3}$ there is a first-order phase transition and phase separation occurs.

The phase transition could also change from being a transition from the normal state to a homogeneous superfluid to a transition from the normal state to a supersolid. The point in the phase diagram where this occurs is called a Lifshitz point [90]. This point can be computed by demanding

$$\alpha(T_L) = \gamma(T_L) = 0, \quad (3.12)$$

where T_L is called the Lifshitz temperature. For temperatures lower than the Lifshitz temperature the transition will be from a normal state to a superfluid state where the bosonic pairs have a nonzero momentum. Superfluidity at nonzero momentum can be established in many ways and due to this variety of possibilities it is difficult to predict which kind of superfluidity will be present below the Lifshitz point. However, they all have to emerge from the Lifshitz point and therefore it is important to know the position of the Lifshitz point.

Apart from the above two possibilities, we can think of other scenarios for the change in character of the phase transitions. But in the phase diagrams we calculated for the imbalanced Fermi gas we only found tricritical points and Lifshitz points. Therefore, these are the only two possibilities we discuss in the following.

3.4 Mean-Field theory

In this section we present the mean-field thermodynamic potential, which is an approximation to the exact Landau thermodynamic potential for the Fermi gas with population and mass imbalance. If we have an expression for the Landau thermodynamic potential, we are able to determine the phase diagram.

Although mean-field theory does not contain all interactions present in a Fermi mixture, it turns out that mean-field theory already incorporates all the relevant physics determining the topology of the phase diagrams. Adding fluctuation effects

only changes the phase diagrams quantitatively [43, 47, 71, 91]. Because of the rather straightforward and transparent calculations in mean-field theory, we first discuss mean-field theory in some detail. Later on we take fluctuation effects into account in order to obtain more quantitative results which we can compare with Monte Carlo calculations and for the mass-balanced case with experiment.

3.4.1 Thermodynamic potential

We consider a two-component Fermi mixture, i.e., a mixture containing either a single fermionic species, for which two different hyperfine states are present, or consisting of two different fermionic species with access to a single hyperfine state. A balanced Fermi gas consists of a single species with an equal population of both spin states. In an imbalanced Fermi gas we allow the populations and masses to be different. To take into account a population imbalance we use different chemical potentials for the two (pseudo)spin states, while a mass imbalance implies that the particles in the two hyperfine states have different masses. The chemical potential and the mass of the fermions in state $|\sigma\rangle$ will be denoted by μ_σ and m_σ respectively. From now on heavy particles are always denoted by a minus sign and light particles by a plus sign, thus $\sigma = \pm$.

The mean-field thermodynamic potential for the imbalanced Fermi gas is given by

$$\begin{aligned} \omega_L(|\Delta|) = & -\frac{|\Delta|^2}{T^{2B}(0)} + \int \frac{d\mathbf{k}}{(2\pi)^3} \left\{ \varepsilon(\mathbf{k}) - \mu - \hbar\omega(\mathbf{k}) \right. \\ & \left. + \frac{|\Delta|^2}{2\varepsilon(\mathbf{k})} - \frac{1}{\beta} \sum_{\sigma} \log \left(1 + e^{-\beta\hbar\omega_{\sigma}(\mathbf{k})} \right) \right\}, \end{aligned} \quad (3.13)$$

where the two-body transition matrix $T^{2B}(0)$ is given by Eq. (3.6). This thermodynamic potential is a direct generalization of the thermodynamic potential for a balanced Fermi gas [89, 92]. In the above expression $\beta = 1/k_B T$ is the inverse thermal energy, $\mu = (\mu_{\uparrow} + \mu_{\downarrow})/2$ is the average chemical potential and half the reduced kinetic energy is $\varepsilon(\mathbf{k}) = (\varepsilon_{\uparrow}(\mathbf{k}) + \varepsilon_{\downarrow}(\mathbf{k}))/2$ with

$$\varepsilon_{\sigma}(\mathbf{k}) = \frac{\hbar^2 \mathbf{k}^2}{2m_{\sigma}}. \quad (3.14)$$

The first terms in the above thermodynamic potential represent the BCS ground state of the mixture, where $\hbar\omega(\mathbf{k})$ is the average dispersion of the quasiparticles

$$\hbar\omega(\mathbf{k}) = \sqrt{(\varepsilon(\mathbf{k}) - \mu)^2 + |\Delta|^2}, \quad (3.15)$$

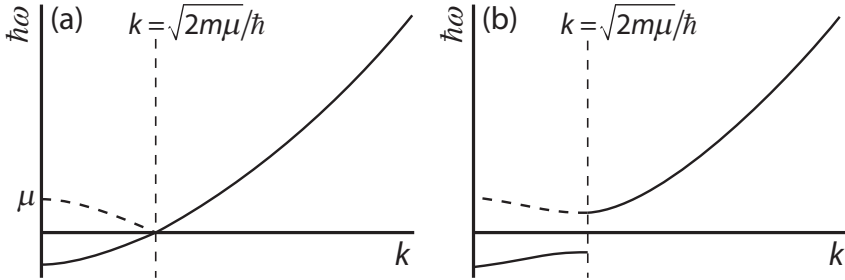


Figure 3.3: The single-particle dispersions $\hbar\omega_\sigma(\mathbf{k})$ for the balanced Fermi gas. Panel (a) shows the dispersions for zero Δ where the system is in the normal state. Panel (b) depicts the case where the system is in the superfluid state, thus the dispersions for nonzero Δ . In both panels the dashed lines are the dispersions of the hole-like excitations, while the full lines give the particle-like dispersions. The latter show more clearly the opening of a gap 2Δ at the Fermi level due to the formation of a condensate of Cooper pairs.

with $|\Delta|$ the so called BCS gap parameter. The complex pairing field Δ is on average related to the expectation value of the pair annihilation operator through

$$\langle \Delta(\mathbf{x}) \rangle = V_0 \left\langle \hat{\psi}_\downarrow(\mathbf{x}) \hat{\psi}_\uparrow(\mathbf{x}) \right\rangle, \quad (3.16)$$

with $\hat{\psi}_\sigma(\mathbf{x})$ the fermionic annihilation operators.

The second part of the thermodynamic potential, namely the part containing the logarithms, corresponds to the contribution of an ideal gas of quasiparticles. Here, $\hbar\omega_\sigma(\mathbf{k})$ is the dispersion relation of the quasiparticles in state $|\sigma\rangle$, given by

$$\hbar\omega_\sigma(\mathbf{k}) = \hbar\omega(\mathbf{k}) - \sigma[2h - \varepsilon_\uparrow(\mathbf{k}) + \varepsilon_\downarrow(\mathbf{k})]/2, \quad (3.17)$$

with $h = (\mu_\uparrow - \mu_\downarrow)/2$ the difference in chemical potentials. For the unpolarized Fermi gas with equal masses the dispersions $\hbar\omega_\sigma(\mathbf{k})$ reduce to the average dispersion in Eq. (3.15). This dispersion is plotted in Fig. 3.3 for both the normal state (Fig. 3.3a) and the superfluid state (Fig. 3.3b). In this case the superfluid is gapped and balanced. For $k = |\mathbf{k}| < \sqrt{2m\mu}/\hbar$ the quasiparticle dispersion describes hole-like excitations. If we mirror this hole-like part of the quasiparticle dispersion, we obtain the negative dispersion of the particle-like excitations. For $k > \sqrt{2m\mu}/\hbar$ the quasiparticle dispersion already describes the particle-like excitations.

In the case of a polarized superfluid with equal masses the dispersions $\hbar\omega_\sigma(\mathbf{k})$ in Fig. 3.3 are shifted by the difference in chemical potentials $2h$. For $h > |\Delta|$

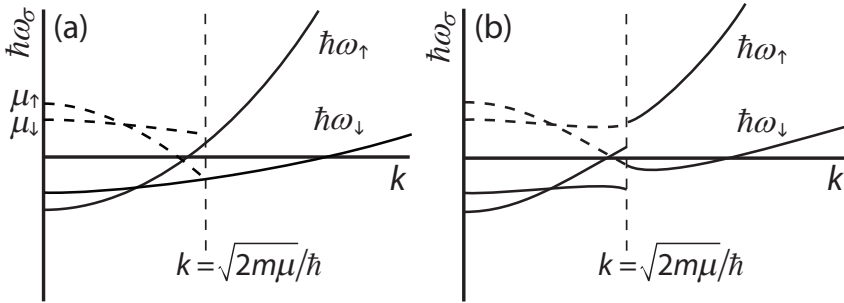


Figure 3.4: The dispersions $\hbar\omega_\sigma(\mathbf{k})$ for the Fermi gas with both population and mass imbalance. Panel (a) shows again the dispersions for zero Δ where the system is in the normal state. And panel (b) again depicts the case where the system is in the superfluid state, thus the dispersions for nonzero Δ . The meaning of the dashed and full lines are the same as for Fig. 3.3.

the dispersion of the majority species becomes negative. When this occurs, the occupation of the single-particle states associated with the negative part of the quasiparticle excitation branch actually lowers the ground-state energy. Since this leads to additional majority quasiparticles and, therefore, additional majority particles and minority holes, in the ground state, the ground state becomes a polarized superfluid. The resulting gapless and polarized superfluid is called the Sarma phase [93]. For the Fermi gas with both mass and population imbalance the dispersions are depicted in Fig. 3.4, where Fig. 3.4a shows the dispersions for zero Δ and Fig. 3.4b for nonzero Δ . The shape of the dispersions is changed due to the difference in mass. It can be seen that in this case also one of the dispersions, namely $\hbar\omega_\downarrow(\mathbf{k})$, is negative so that it would correspond to a gapless Sarma superfluid.

3.4.2 Landau coefficients

For the imbalanced Fermi mixture, we want to study the phase transition from the normal state to the superfluid state. For that transition we want to obtain a phase diagram with the critical temperature as a function of the polarization, $P = (n_\uparrow - n_\downarrow)/(n_\uparrow + n_\downarrow)$ with n_σ the density of particles in state $|\sigma\rangle$.

The particle densities n_σ can be determined from the thermodynamic potential using [89]

$$n_\sigma = -\frac{\partial\omega_L(\Delta)}{\partial\mu_\sigma}\Bigg|_{\Delta=\langle\Delta\rangle}. \quad (3.18)$$

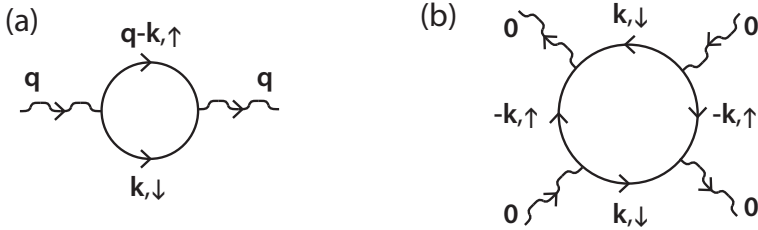


Figure 3.5: (a) The ladder diagram with external momentum \mathbf{q} . The wiggly lines denote the Cooper pairs, which can break up into two fermions of different spin, denoted by the normal lines. Here, \mathbf{q} is the wavevector of the Cooper pairs, while \mathbf{k} and $\mathbf{q} - \mathbf{k}$ are the wavevectors of the fermions. When \mathbf{q} is equal to zero, the amplitude of this diagram corresponds to the quadratic Landau coefficient α in the thermodynamic potential. (b) The Feynman diagram corresponding to the fourth-order Landau coefficient β .

Moreover, in Sec. 3.3 the critical conditions for the transition were explained. In mean-field theory, the quadratic Landau coefficient α is explicitly given by

$$\begin{aligned} \alpha &= \frac{\partial \omega_L}{\partial |\Delta|^2} \Big|_{|\Delta|^2=0} \\ &= -\frac{1}{T^{2B}(0)} + \int \frac{d\mathbf{k}}{(2\pi)^3} \left(\frac{1}{2\varepsilon(\mathbf{k})} + \frac{N_\uparrow(\mathbf{k}) + N_\downarrow(\mathbf{k}) - 1}{2(\varepsilon(\mathbf{k}) - \mu)} \right), \end{aligned} \quad (3.19)$$

where $N_\sigma(\mathbf{k}) = 1/(\exp[\beta(\varepsilon_\sigma(\mathbf{k}) - \mu_\sigma)] + 1)$ are the Fermi distribution functions. To determine the temperature of the tricritical point, we also need to know the fourth-order Landau coefficient β . It is given by

$$\begin{aligned} \beta &= \frac{\partial^2 \omega_L}{(\partial |\Delta|^2)^2} \Big|_{|\Delta|^2=0} \\ &= \int \frac{d^3\mathbf{k}}{(2\pi)^3} \frac{1}{4(\varepsilon(\mathbf{k}) - \mu)^2} \left[\beta N_\uparrow(\mathbf{k})(N_\uparrow(\mathbf{k}) - 1) + \beta N_\downarrow(\mathbf{k})(N_\downarrow(\mathbf{k}) - 1) \right. \\ &\quad \left. + \frac{1 - N_\uparrow(\mathbf{k}) - N_\downarrow(\mathbf{k})}{\varepsilon(\mathbf{k}) - \mu} \right]. \end{aligned} \quad (3.20)$$

Determining γ from the mean-field thermodynamic potential is not possible, since we have assumed the bosonic pairing field $\Delta(\mathbf{x})$ to be independent of position. Nevertheless, there is a rather simple way to determine this coefficient, using Feynman diagrams [94]. The other coefficients could also have been determined using a diagrammatic language. Namely, the quadratic coefficient α corresponds

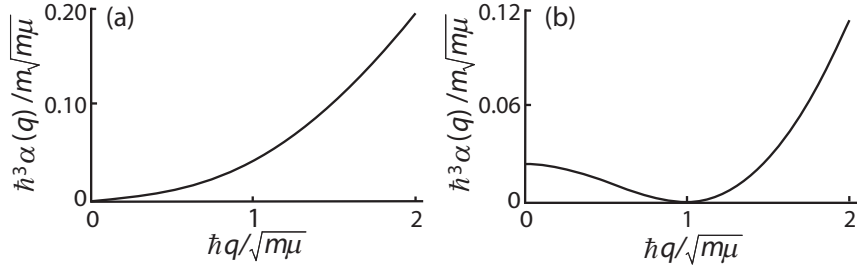


Figure 3.6: Depending on the temperature and the chemical potentials, the minimum of $\alpha(\mathbf{q})$ is either at zero or at nonzero external momentum $\hbar q$. In both pictures the mass ratio is $r = 6.7$. In panel (a), the minimum of $\alpha(\mathbf{q})$ is located at zero external momentum. The corresponding polarization is $P = -0.61$ and the temperature is $T/T_F = 0.21$ with T_F the Fermi temperature. In panel (b), the minimum of $\alpha(\mathbf{q})$ is attained at a nonzero momentum. Here the polarization is $P = -0.7$ and the temperature is $T/T_F = 0.13$.

to the so called ladder diagram where the incoming and outgoing bosonic fields Δ have zero momentum, see Fig. 3.5a. Physically, α can be interpreted as being proportional to the chemical potential of the Cooper pairs. The fourth-order coefficient β has a diagrammatic representation with four external bosonic fields with zero momentum, see Fig. 3.5b.

For the transition to the supersolid phase, we consider the ladder diagram where the bosonic fields carry nonzero momentum \mathbf{q} , since the supersolid phase consists of bosonic pairs with nonzero momentum. The expression for this ladder diagram is

$$\alpha(\mathbf{q}) = -\frac{1}{T^{2B}(0)} + \int \frac{d^3\mathbf{k}}{(2\pi)^3} \left\{ \frac{1}{2\varepsilon(\mathbf{k})} + \frac{N_\uparrow(\mathbf{q}-\mathbf{k}) + N_\downarrow(\mathbf{k}) - 1}{\varepsilon_\uparrow(\mathbf{q}-\mathbf{k}) + \varepsilon_\downarrow(\mathbf{k}) - 2\mu} \right\}. \quad (3.21)$$

The actual shape of $\alpha(\mathbf{q})$ as a function of the external momentum \mathbf{q} depends on the values of the different parameters in this expression, such as the chemical potentials and the temperature. Depending on those quantities the minimum of $\alpha(\mathbf{q})$ is attained either for zero or for nonzero external momentum. As explained in Sec. 3.3, a second-order phase transition can occur, when a quadratic coefficient of the Landau theory changes sign. These coefficients are now given by $\alpha(\mathbf{q})$, where \mathbf{q} is the wavevector of the bosonic pairs. The sign change occurs first for the minimum of $\alpha(\mathbf{q})$, which therefore determines whether or not the transition happens at nonzero \mathbf{q} . The expression for the ladder diagram with nonzero external

momentum can be expanded in even powers of \mathbf{q}

$$\alpha(\mathbf{q}) = a_0 + a_1 \mathbf{q}^2 + a_2 \mathbf{q}^4 + \dots, \quad (3.22)$$

where the dots denote higher order powers in \mathbf{q}^2 . If all the coefficients a_i are positive, $\alpha(\mathbf{q})$ has a minimum for external momentum zero, so that a transition to the homogeneous superfluid phase occurs. But if a_1 is negative, $\alpha(\mathbf{q})$ has a minimum for a nonzero external momentum and therefore it first becomes zero at some nonzero value of \mathbf{q} . The minimum of the thermodynamic potential will then be located at a nonzero order parameter with a nonzero momentum. In other words, it will be energetically favorable for the bosonic pairs to have kinetic energy and the phase transition that occurs is a transition from the normal state to an inhomogeneous superfluid. Comparing this with the Landau theory of Sec. 3.3, we see that in the expansion of $\alpha(\mathbf{q})$, a_0 can be identified with the quadratic coefficient α and a_1 can be identified with γ . Thus, from the ladder diagram with external momentum an expression for γ can be found, namely

$$\gamma = \left. \frac{\partial \alpha(\mathbf{q})}{\partial \mathbf{q}^2} \right|_{\mathbf{q}=0}. \quad (3.23)$$

Physically, γ can be interpreted as being proportional to the inverse of the effective mass of the Cooper pairs.

3.4.3 Results

In this section the results using mean-field theory are presented. First, we present phase diagrams for three Fermi gases with different mass imbalances. Then, we study the effect of the mass imbalance on the critical temperature for an unpolarized Fermi gas. After this, we study the effect of the interaction strength on the temperature corresponding to a tricritical point or a Lifshitz point. Finally, we also consider the superfluid Sarma phase.

Phase diagrams

With the expressions for the Landau coefficients, the phase diagram can be calculated for a fixed mass ratio r and a fixed interaction strength $1/k_F a$. We determine the phase diagram as a function of temperature T and polarization $P = (n_\uparrow - n_\downarrow)/(n_\uparrow + n_\downarrow)$. The mass ratio r is given by $r = m_\downarrow/m_\uparrow$. The interaction strength is characterized by the s -wave scattering length a and the Fermi momentum k_F , which is defined as

$$k_F = (3\pi^2 n)^{1/3}, \quad (3.24)$$

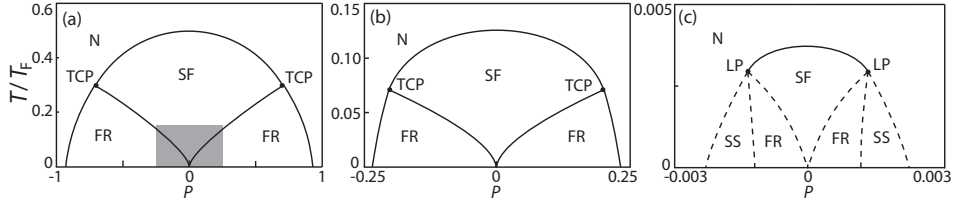


Figure 3.7: Phase diagrams of the mass-balanced Fermi gas, $r = 1$, as a function of temperature T and polarization P at different interaction strengths. The temperature is scaled with the Fermi temperature T_F . Panel (a) shows the phase diagram in the strongly interacting limit, $1/k_F a = 0$. There is a tricritical point (TCP), where the normal state (N), the homogeneous superfluid state (SF) and the forbidden region (FR) meet. The shaded area sets the scale for panel (b), where the phase diagram for a weaker interaction, $1/k_F a = -1$, is shown. Again, there is a tricritical point. There is again a shaded region to set the scale for panel (c), but it is too small to see. In panel (c) the phase diagram is shown for a very weak interaction, $1/k_F a = -3$, and the critical temperatures are now extremely low. For this interaction we find a Lifshitz point (LP), below which there is an instability towards a supersolid (SS). The size of this supersolid region is not calculated within our theory and therefore the dashed lines are only guides to the eye.

where $n = n_\uparrow + n_\downarrow$ is the total particle density. In order to obtain a phase diagram independent of the total particle density n , we scale the temperature with the reduced Fermi temperature

$$k_B T_F = \varepsilon_F = \frac{\hbar^2 k_F^2}{2m}, \quad (3.25)$$

where m is twice the reduced mass, introduced in Eq. (3.5) and k_B is Boltzmann's constant.

We present the phase diagram for three different mass ratios, namely for $r = 1$, which is the mass-balanced case, $r = 6.7$, which corresponds to a ${}^6\text{Li}-{}^{40}\text{K}$ mixtures, and for $r = 10$ where an interesting feature in the phase diagram is found regarding the tricritical point [85]. For these mass ratios we present the phase diagrams at three different interaction strengths in order to see what the effect of the interaction is on the critical temperature. Namely, we present the phase diagrams for a strongly interacting Fermi gas with $1/k_F a = 0$, an intermediate interaction strength with $1/k_F a = -1$ and a weakly interacting Fermi gas. These interaction strengths correspond to the BCS side of the Feshbach resonance, see Fig. 3.1.

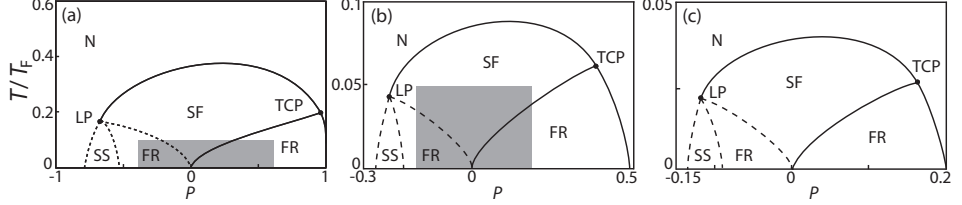


Figure 3.8: Phase diagrams of the Fermi gas with mass ratio $r = 6.7$ for different interaction strengths. Panel (a) shows the phase diagram in the strongly interacting limit. The size of the box is the same as for the mass-balanced case such that the effect of the mass imbalance can be seen. The shaded region sets the scale for panel (b), where the interaction strength is weaker, $1/k_F a = -1$. And in panel (b) the shaded region in turn sets the scale for panel (c) where the interaction is even weaker, $1/k_F a = -3/2$. The dashed lines are again guides to the eye.

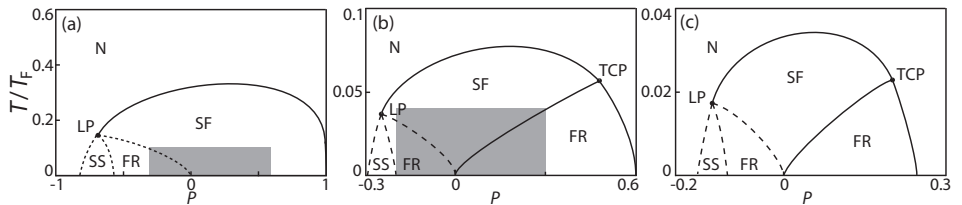


Figure 3.9: Phase diagrams of the Fermi gas with mass ratio $r = 10$ for different interaction strengths. Again, panel (a) shows the phase diagram in the strongly interacting limit and the size of the box is again the same as for the mass-balanced case. The shaded region sets the scale for panel (b), where the interaction strength is weaker, $1/k_F a = -1$. And in panel (b) the shaded region in turn sets the scale for panel (c) where the interaction is even weaker, $1/k_F a = -3/2$. Again, the dashed lines are only guides to the eye.

Fig. 3.7 shows the phase diagrams of the mass-balanced Fermi gas at three different interaction strengths. In Fig. 3.7a the phase diagram for the strongly interacting regime where $1/k_{\text{F}}a = 0$ is depicted. It is symmetric in the polarizations. The phase transition is of second order for small polarizations. Moreover, we find two tricritical points in the phase diagram and below the tricritical points the phase transition is of first order. At a first-order phase transition the order parameter is discontinuous and therefore also the particle densities n_σ , see Eq. (3.18). And thus also the polarization is discontinuous at a first-order phase transition, which gives rise to a forbidden region where phase separation occurs. Fig. 3.7b again shows the phase diagram of the mass-balanced Fermi gas, but now for a weaker interaction, namely for $1/k_{\text{F}}a = -1$. Compared to the unitarity regime, there are no qualitative changes in the phase diagram. However, the critical temperatures are lower than in the strongly interacting regime. Then, Fig. 3.7c shows the phase diagram of the mass-balanced Fermi gas for a very weak interaction, namely $1/k_{\text{F}}a = -3$. Apart from the fact that the critical temperatures are now extremely low, there is a large difference compared to the strongly interacting regime, namely we do not find tricritical points in the phase diagram but instead we find two Lifshitz points. Below the Lifshitz point there is an instability towards supersolidity. We assumed that there will be a second-order transition from the normal state to the supersolid. The critical temperature for this transition is found by solving $\alpha(\mathbf{k}_{\text{LO}}) = 0$, where \mathbf{k}_{LO} is the wavevector of the supersolid. The transition from supersolidity to the homogeneous superfluid phase is expected to be first order [39, 83] and thus a forbidden region will be present in the phase diagram. This simple scenario is sketched in the phase diagram, but it could be that the normal to supersolid second-order phase transition is preempted by weak first-order transitions from the normal state to various more complicated supersolid phases [39, 83, 84]. For the calculation of the relevant fourth-order diagrams with nonzero external momenta, one needs to make an assumption about the crystal structure of the supersolid phase, in order to calculate a first-order phase transition to the supersolid phase. This calculation for the stability regions of all possible supersolid phases is beyond the scope of this paper. To emphasize that we did not investigate this region in great detail we there used dashed lines in the phase diagram.

Fig. 3.8 again shows three phase diagrams at different interactions, but now for the mass-imbalanced Fermi gas with mass ratio $r = 6.7$, corresponding to the ${}^6\text{Li}$ - ${}^{40}\text{K}$ Fermi mixture. In the unitarity regime, see Fig. 3.8a, the phase diagram is no longer symmetric in polarizations and the temperatures are lower in comparison with the mass-balanced case. Furthermore, already in the strongly interacting regime we find a Lifshitz point in the phase diagram for a majority of heavy atoms. For a majority of light particles a tricritical point is found. This

is in sharp contrast with the mass-balanced case where a Lifshitz point is only present for extremely weak interactions. As a result, the Lifshitz temperature is then at least about a hundred times lower than for the ${}^6\text{Li}-{}^{40}\text{K}$ mixture. Below the tricritical point there is a forbidden region and below the Lifshitz point there is an instability towards a supersolid. We sketched the same scenario below the Lifshitz point here as for the mass-balanced case. In Fig. 3.8b and Fig. 3.8c the phase diagrams of the Fermi gas are depicted at interaction strengths $1/k_{\text{Fa}} = -1$ and $1/k_{\text{Fa}} = -3/2$ respectively. The interaction strength does not affect the topology of the phase diagram, but it does affect the critical temperatures. Just as in the mass-balanced case, the critical temperatures are lower for weaker interactions, as expected.

In Fig. 3.9 we show the phase diagrams of an imbalanced Fermi gas with an even larger mass imbalance, namely with mass ratio $r = 10$. The diagram has become even more asymmetric. In the strongly interacting regime, we also find a Lifshitz point for a majority of heavy atoms. But the tricritical point has disappeared, which means that the phase transition remains of second order and no phase separation occurs for a majority of light particles. Below the Lifshitz point the same scenario is sketched as before. Fig. 3.9b shows the phase diagram at a weaker interaction strength, namely at $1/k_{\text{Fa}} = -1$. With respect to the unitarity limit there is a real change in this diagram. Namely, the tricritical point reappears in the phase diagram. Then, in Fig. 3.9c the interaction strength is even weaker, $1/k_{\text{Fa}} = -3/2$, and the critical temperatures are lower. But there are no qualitative changes with respect to the phase diagram in Fig. 3.9b.

Effect of a mass imbalance

By comparing the phase diagrams of the mass-balanced Fermi gas and of the Fermi gases with a mass imbalance, it can be seen that a mass imbalance causes important changes. First, the critical temperatures for the mass-imbalanced Fermi gases are lower than for the mass-balanced case. Second, for a mass-imbalanced Fermi gas the phase diagram is no longer symmetric in polarizations. In other words, the maximum critical temperature is no longer located at zero polarization. Third, for Fermi gases with a sufficiently large mass ratio, like the two mass-imbalanced Fermi gases we presented here, there is a Lifshitz point in the phase diagram for a majority of heavy atoms. These three changes we now discuss in some more detail.

In the weakly interacting limit, the critical temperatures are very low. For the unpolarized Fermi gas the integral in Eq. (4.5) can then be evaluated exactly. Then, by equating α to zero an analytic result for the critical temperature can be

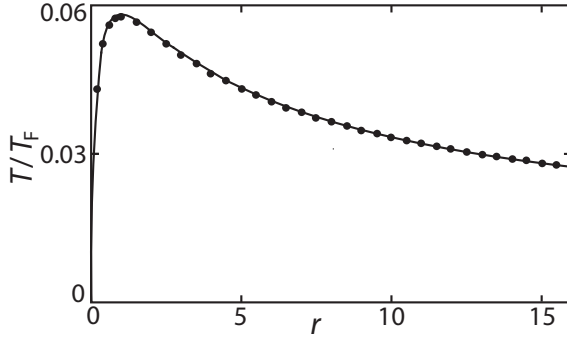


Figure 3.10: The critical temperature of an unpolarized Fermi gas as a function of the mass ratio $r = m_\downarrow/m_\uparrow$. The circles are the numerical results of $\alpha = 0$ and the full line is the analytic result for the weakly interacting limit. Here $1/k_F a = -3/2$.

obtained [95]

$$\begin{aligned} T_c|_{P=0} &= \sqrt{\varepsilon_F, \uparrow \varepsilon_F, \downarrow} \frac{8}{\pi k_B} e^{\gamma-2} e^{-\pi/2k_F|a|} \\ &= \frac{2\sqrt{r}}{1+r} \frac{8\varepsilon_F}{\pi k_B} e^{\gamma-2} e^{-\pi/2k_F|a|}, \end{aligned} \quad (3.26)$$

where ε_F is the Fermi energy corresponding to twice the reduced mass, k_B is Boltzmann's constant and $\gamma = 0.5772$ is Euler's constant. When the atoms making up the Fermi mixture have different masses, r is not equal to one. In that case the term $2\sqrt{r}/(1+r)$ is smaller than one. And thus, by adding a mass imbalance the critical temperature for the unpolarized Fermi gas becomes lower. In Fig. 3.10, it can be seen that the dependence of the critical temperature on the mass ratio is indeed as given by Eq. (3.26) and that the agreement with the numerical results is very good. For the polarized Fermi gas, we expect a similar dependence of the critical temperature on the mass ratio.

For the mass-balanced Fermi gas, the highest critical temperature is located at zero polarization, see Fig. 3.7, whereas for the mass-imbalanced Fermi gas it is located at nonzero polarization, see Fig. 3.8 and Fig. 3.9. As a consequence, the derivative of the critical temperature with respect to h , the difference in chemical potentials, will no longer be zero at $P = 0$. In the weakly interacting limit, the coefficient α in Eq. (4.5) can be expanded around the critical temperature T_c and

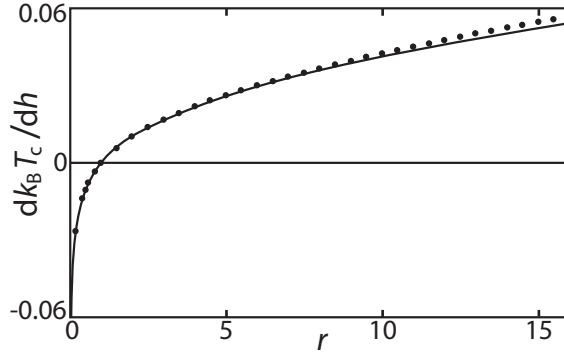


Figure 3.11: Derivative of the critical temperature with respect to the difference in chemical potentials h . The circles are the numerical results and the full line is the analytic result. The interaction strength is $1/k_F a = -3/2$.

the critical ‘Zeeman’ field h_0 corresponding to the unpolarized Fermi gas

$$\alpha(T_c + \delta T_c, h_0 + \delta h) \simeq \alpha(T_c, h_0) + \frac{\partial \alpha}{\partial T}(T_c, h_0)\delta T_c + \frac{\partial \alpha}{\partial h}(T_c, h_0)\delta h. \quad (3.27)$$

For a continuous phase transition, α has to go to zero. The term on the left-hand side and the first term on the right-hand side are therefore zero. Then we find from the other two terms

$$\begin{aligned} \left. \frac{\delta T_c}{\delta h} \right|_{P=0} &= -\frac{\partial \alpha / \partial h}{\partial \alpha / \partial T} = T_c|_{P=0} \frac{1}{4} \left(\frac{1}{\varepsilon_{F,\downarrow}} - \frac{1}{\varepsilon_{F,\uparrow}} \right) \\ &= \frac{2}{\pi k_B} \frac{r-1}{\sqrt{r}} e^{\gamma-2} e^{-\pi/2k_F|a|}. \end{aligned} \quad (3.28)$$

This is indeed nonzero if the mass ratio is not equal to one. Eq. (3.28) is positive for mass ratios larger than one. This is in agreement with our findings that the phase diagram shifts towards positive polarizations for a mass ratio larger than one, see Fig. 3.8 and Fig. 3.9. For mass ratios smaller than one, Eq. (3.28) is negative and the phase diagram then shifts towards negative polarizations. In both cases the phase diagram shifts towards a majority of light particles. Eq. (3.28) is plotted in Fig. 3.11, together with the numerical results. The agreement is good, especially for small mass ratios.

For a sufficiently large mass ratio we find a Lifshitz point in the phase diagram for a majority of heavy particles. To explain why this can be expected we consider the kinetic energies of the particles in Eq. (3.14), which are plotted in Fig. 3.12. In

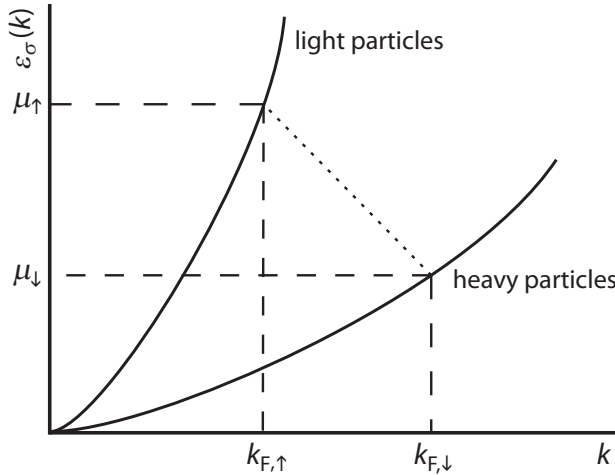


Figure 3.12: The energies $\varepsilon_\sigma(k)$ of the fermions for a Fermi mixture with both a population and a mass imbalance, where $m_\downarrow > m_\uparrow$ and $n_\downarrow > n_\uparrow$. Thus, there is a majority of heavy particles. At the Fermi levels, the energy difference between particles with different momenta (dashed line) is smaller than the energy difference between particles with the same momenta.

In the mass-balanced case a fermion of one species with momentum \mathbf{k} has the same energy as a fermion with momentum $-\mathbf{k}$ of the other species. Coupling these degenerate states by a condensate of Cooper pairs is energetically desirable since the shift of the energy levels due to the coupling is now largest, as is well-known from the physics of avoided crossings. Therefore, it is thus most favorable to form a pair of two fermions with the same but opposite momentum, i.e., a fermion with momentum \mathbf{k} forms a pair with a fermion with momentum $-\mathbf{k}$, since then the energy gain as a result of pairing is maximal. The pair then has no kinetic energy and the pairs form a homogeneous superfluid.

Typically, the formation of pairs mostly occurs at the Fermi energy. There a pair consists of one fermion with momentum \mathbf{k}_F and one with momentum $-\mathbf{k}_F$. Since the Fermi momentum depends on the density of the particles n_σ , see Eq. (3.24), the Fermi momenta will not be the same in the case of a population imbalance. This makes pairing less ideal than in the unpolarized case. The critical temperatures are therefore lower for a polarized mixture, see Fig. 3.7.

In the mass-imbalanced case two fermions with equal momentum but from different species do not have the same kinetic energy. Thus, if now a fermion of

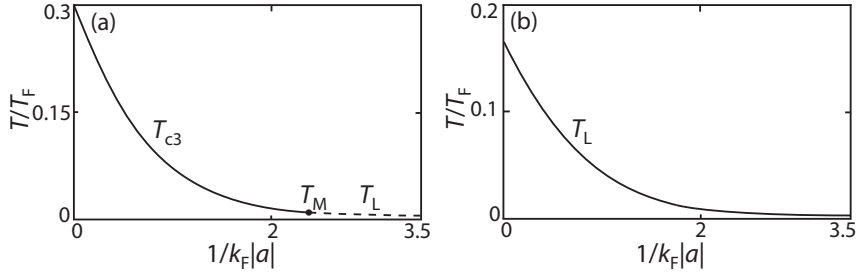


Figure 3.13: Temperature of the tricritical points and the Lifshitz points as a function of the interaction strength. Panel (a) shows the mass-balanced case. In panel (b) we look at a Fermi gas with mass ratio $r = 6.7$ and a majority of heavy particles. T_{c3} is the temperature of a tricritical point, T_M is the temperature of a multicritical point and T_L of a Lifshitz point.

one species with momentum \mathbf{k} forms a pair with a fermion with momentum $-\mathbf{k}$ of the other species, there is an energy difference that reduces the energy gain that can be obtained due to pairing. This explains the fact that the critical temperatures are lower for Fermi mixtures with a mass imbalance. With both a mass imbalance and a population imbalance pairs can still be formed with two fermions with equal but opposite momentum, even though there is an energy difference between the Fermi levels. However, this occurs only if the mass ratio and the population imbalance are not too large. In the extreme case of a large mass imbalance and a large population imbalance a more favorable scenario is possible, see Fig. 3.12. In this figure the kinetic energies are plotted for the different fermions, and there is a majority of heavy particles, thus $k_{F,\downarrow} > k_{F,\uparrow}$. It can be seen that the energy difference between particles with different momenta is now smaller than the energy difference between fermions with the same momentum, i.e., it is now energetically more favorable to form pairs with a nonzero momentum that allows for a direct coupling of the Fermi levels. The first point where this is the case is the Lifshitz point. There the system becomes a supersolid.

Multicritical point

In the phase diagrams, Fig. 3.7, Fig. 3.8 and Fig. 3.9, we find, depending on the mass ratio and the interaction strength, tricritical points (P_{c3}, T_{c3}) , which are solutions of Eq. (3.11), as well as Lifshitz points (P_L, T_L) , solutions of Eq. (3.12).

At unitarity, we find for the mass-balanced case at unitarity a tricritical point, whereas we find a Lifshitz point for the ${}^6\text{Li}-{}^{40}\text{K}$ mixture for a majority of heavy

particles. This Lifshitz point is a clearly distinct point from a tricritical point, just as the tricritical point for the mass-balanced case is a clearly distinct point from a Lifshitz point. This is in accordance with the findings of Parish *et al.* [96], who found that for a mass-balanced Fermi mixture the FFLO line detaches from the tricritical point away from the BCS limit. However, there is a mass ratio between $r = 1$ and $r = 6.7$ for which the phase diagram at unitarity contains a point which is both a tricritical point and a Lifshitz point. In other words, for this mass ratio Eq. (3.11) and Eq. (3.12) have a solution exactly at the same point in the phase diagram. This is a multicritical point and it is found to occur for the mass ratio $r = 4.22$.

It can also be seen in the different phase diagrams that for a given mass ratio the location of tricritical and Lifshitz points changes as the interaction strength changes. In Fig. 3.13, it is shown for the mass-balanced Fermi gas and for the Fermi gas with mass ratio $r = 6.7$ how the temperature T of these points changes as a function of the interaction strength. Note that the polarization is not constant for the lines in Fig. 3.13. In both Fig. 3.13a and Fig. 3.13b one can recognize an exponential decay as a function of the interaction strength, which is exactly what one would expect from Eq. (3.26).

Fig. 3.13a shows the mass-balanced case. In the unitarity regime and for small values of $1/k_F|a|$ a tricritical point is present in the phase diagram, with temperature T_{c3} . This is the full line in Fig. 3.13a. Then for some value of the interaction strength Eq. (3.11) and Eq.(3.12) have a solution at the same point. Thus, there is a multicritical point and the temperature of this point is in Fig. 3.13 denoted by T_M . For even weaker interactions it then turns out that there is an instability towards a supersolid and thus we find a Lifshitz point in the phase diagram, with temperature T_L . This is the dashed line in Fig. 3.13a.

Although the tricritical and Lifshitz points are very close together for very weak interactions, in our approach, where we perform the momentum integrals to calculate the coefficients γ in Eq. (3.23) and β in Eq. (3.20), they are essentially always two distinct points. Except for one value of the interaction strength where we find a multicritical point. If one, however, assumes particle-hole symmetry in the weakly-interacting limit, Eq. (3.23) and Eq. (3.20) become, up to a constant, the same equation and thus one finds that the tricritical point and the Lifshitz point are the same point [39, 97].

Fig. 3.13b gives the temperature of the Lifshitz point present in the phase diagram of the Fermi gas with mass ratio $r = 6.7$ for a majority of heavy particles. Here, we do not find a change in character of the phase transition as a function of interaction strength. The Lifshitz point remains a Lifshitz point. For a majority of light particles of this Fermi mixture, we found a tricritical point in the strongly

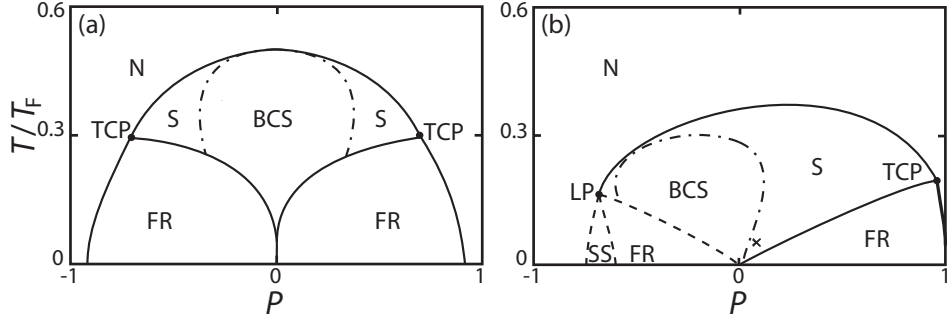


Figure 3.14: Phase diagrams at unitarity including the region where the superfluid is gapless. Panel (a) shows the mass-balanced case. It is the same phase diagram as in Fig. 8a, only now the superfluid region is divided into a gapped superfluid region (BCS) and two Sarma regions (S). Panel (b) shows the mass-imbalanced Fermi gas with mass ratio $r = 6.7$. The small cross in panel (b) is the point at which we calculated the distribution functions of the particles shown in Fig. 3.15.

interacting limit. We expect that this point will also change to a Lifshitz point for very weak interactions, but the extremely low temperatures make it numerically difficult to investigate this possibility in detail.

Sarma phase

In Sec. IVA, while explaining the dispersions of the quasiparticles, we discussed the possibility of a Sarma phase, which occurs when one of the dispersions $\hbar\omega_\sigma(\mathbf{k})$ becomes negative. At each point in the phase diagram the value of the order parameter $|\Delta|$ can be found by minimizing the thermodynamic potential in Eq. (3.13). With this value of the order parameter it can be determined whether the dispersions are always positive or become negative for some range of momenta. In the superfluid phase it turns out that there are different regions. In one region the dispersions are always positive and the superfluid is gapped, while in the other region one of the dispersions becomes negative and we are dealing with a gapless superfluid. At nonzero temperatures, there is no phase transition between these regions. Rather, there is only a smooth crossover. We calculated the gapless superfluid region in the unitarity limit for the mass-balanced case and for the ${}^6\text{Li}$ - ${}^{40}\text{K}$ Fermi mixture. The results are shown in Fig. 3.14. In the mass-balanced case, Fig. 3.14a, there are two regions in the phase diagram where we have a gapless superfluid. In Fig. 3.14b the mass-imbalanced case is shown. Here, the Sarma region is not symmetric in polarizations, just as the rest of the phase diagram.

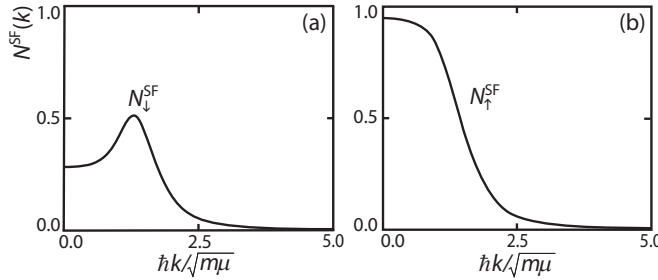


Figure 3.15: The distribution functions $N_\sigma^{\text{SF}}(\mathbf{k})$ for the heavy particles, panel (a), and the light particles, panel (b), in the gapless superfluid phase.

The Sarma region is very large for positive polarizations, whereas for negative polarizations it becomes very small.

Fig. 3.15 depicts the distribution functions $N_\sigma^{\text{SF}}(\mathbf{k})$ of the heavy and the light particles for some point in the phase diagram of Fig. 3.14b that lies in the superfluid Sarma region. In the superfluid phase the distribution functions are modified with respect to the Fermi distribution functions $N_\sigma(\mathbf{k})$ and are given by

$$N_\sigma^{\text{SF}}(\mathbf{k}) = \frac{1}{2} \left[1 + \frac{\varepsilon(\mathbf{k}) - \mu}{\hbar\omega(\mathbf{k})} \right] N_\sigma(\mathbf{k}) + \frac{1}{2} \left[1 - \frac{\varepsilon(\mathbf{k}) - \mu}{\hbar\omega(\mathbf{k})} \right] [1 - N_{-\sigma}(\mathbf{k})]. \quad (3.29)$$

It can be seen in Fig. 3.15 that the distribution function of the heavy particles is nonmonotonic, which is a signature of the Sarma phase.

3.5 Fluctuation effects

As argued before, mean-field theory only leads to a qualitative description of the phase transitions that occur in an imbalanced Fermi gas with unitarity-limited interactions. To achieve also a quantitative description, we have to take fluctuation effects into account. From renormalization-group calculations [47], we know that especially selfenergy effects and the screening of the interaction by particle-hole fluctuations are important in the unitarity limit. The corresponding corrections result in quantitative agreement with experiments in the mass-balanced case [47], and give rise to more accurate predictions for upcoming experiments with the very promising ${}^6\text{Li}-{}^{40}\text{K}$ mixture [71].

As explained in Refs. [71, 77], a convenient way to take selfenergy corrections into account is to introduce renormalized chemical potentials μ'_σ that describe the

(a)

V_{sc}
 $= \bullet +$

 $+ \quad$

 $+ \dots$

(b)

$\frac{1}{V_{sc}}$
 $= \frac{1}{V_0} \otimes$

Figure 3.16: The screened interaction containing an infinite sum of bubble diagrams. Panel (a) shows the perturbative expansion of the screened interaction and panel (b) shows the result of the resummation of this expansion.

selfenergy of particles with spin σ in a Fermi sea of particles with spin $-\sigma$. This can be achieved by using

$$\mu'_\sigma = \mu_\sigma + c_\sigma \frac{\mu'^2_{-\sigma}}{\mu'_\sigma + \mu'_{-\sigma}}, \quad (3.30)$$

where c_σ is a coefficient that can be determined in the ladder approximation [66], but also with the use of renormalization-group calculations [47] or Monte Carlo calculations [74]. For the mass-balanced case, we use $c_{\uparrow,\downarrow} = 0.6$, while for the ${}^6\text{Li}-{}^{40}\text{K}$ mixture we use $c_\uparrow = 2.3$ and $c_\downarrow = 0.36$ to incorporate the Monte Carlo results. The substitution of these renormalized chemical potentials $\mu'_\sigma(\mu_\sigma)$ in the mean-field thermodynamic potential $\omega_L(\Delta; \mu'_\sigma)$ results in the following equation for the densities

$$n_\sigma = - \left. \frac{\partial \omega_L(\Delta; \mu'_\sigma)}{\partial \mu_\sigma} \right|_{\Delta=\langle \Delta \rangle}. \quad (3.31)$$

In Ref. [71], an accurate comparison between the use of renormalized chemical potentials and Monte Carlo calculations was made at zero temperatures, leading to excellent agreement. Note that in the superfluid state Eq. (3.30) overestimates the effects of the interactions on the renormalization of the chemical potentials and another correction proportional to Δ^2 has to be subtracted in the right-hand side of Eq. (3.30) [77].

Fluctuations do not only affect the selfenergies of the fermions in the normal state. There is another effect of particle-hole fluctuations that affects the transition to the superfluid state. Namely, there is a change in the coefficient α due to screening of the interspecies interaction, which is also called the Gor'kov correction. We can take the screening into account by considering an effective two-body interaction that includes the so-called random-phase approximation (RPA) bubble sum. This procedure is diagrammatically represented in Fig. 3.16. The inclusion of the infinite geometric series of bubble diagrams leads at zero external momentum

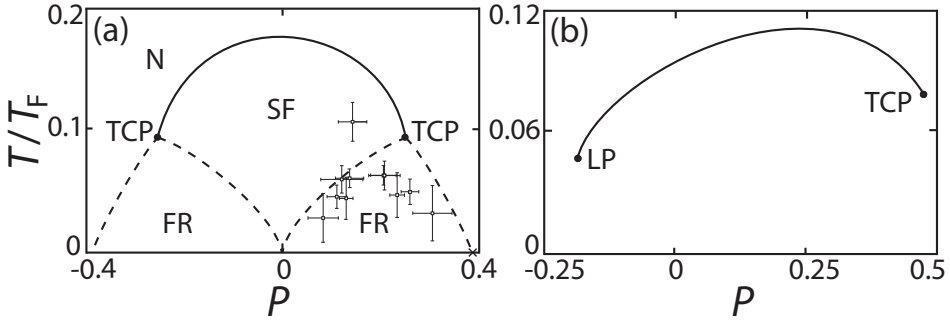


Figure 3.17: Phase diagrams of strongly interacting Fermi gases, i.e., $1/k_{\text{F}}a = 0$, where fluctuation effects have been taken into account. Panel (a) shows the mass-balanced case, i.e., $r = 1$. The open squares are data along the phase boundaries from the experiment of Shin *et al.* [42]. The dashed lines denote the first-order phase transitions, not calculated within our theory and therefore only guides to the eye. However, they include the correct critical polarization at zero temperature, denoted by a cross, known from Monte Carlo calculations [45]. To calculate the first-order phase transition lines more accurately with fluctuation effects taken into account other methods are needed [77]. Panel (b) shows the phase diagram for the $^6\text{Li}-^{40}\text{K}$ mixture, where $r = 6.7$. For both mixtures the critical temperatures are lowered by taking fluctuation effects into account, compare Fig. 3.7a and Fig. 3.8a.

and frequency to

$$\frac{1}{V_{\text{sc}}} = \frac{1}{V_0} - \hbar\Pi(\mathbf{0}, 0), \quad (3.32)$$

where $\hbar\Pi(\mathbf{0}, 0)$ is the amplitude of the bubble diagram. In Appendix B, it is shown that this amplitude is given by

$$\hbar\Pi(\mathbf{0}, 0) = \int \frac{d\mathbf{k}'}{(2\pi)^3} \frac{N_{\uparrow}(\mathbf{k}') - N_{\downarrow}(\mathbf{k}')}{2h' - \epsilon_{\uparrow}(\mathbf{k}') + \epsilon_{\downarrow}(\mathbf{k}')}, \quad (3.33)$$

where we use renormalized chemical potentials to also include the fermionic self-energy effects. Using the screened interaction of Eq. (3.32) in Eq. (3.4), we obtain a screened two-body transition matrix $T_{\text{sc}}^{2B}(0)$, which consequently enters the expression for the quadratic coefficient in Eq. (4.5). When the quadratic coefficient including screening becomes zero, a second-order transition can occur, so that the critical condition now becomes

$$\alpha_{\text{sc}}(T_c, \mu'_{\sigma}) = \alpha(T_c, \mu'_{\sigma}) + \hbar\Pi(\mathbf{0}, 0) = 0. \quad (3.34)$$

The new critical condition that includes both screening and fermionic selfenergy effects typically reduces the obtained critical temperatures with a factor of three.

If we apply this procedure to determine the line of second-order phase transitions in the mass-balanced case, we obtain the result in Fig. 3.17a. In this figure, also the data along the phase boundaries from the experiment of Shin *et al.* [42] are shown. For the unpolarized Fermi gas, we find $T_c = 0.18T_F$ and $\mu(T_c) = 0.51T_F$ [71], which is to be compared with the Monte Carlo results $T_c = 0.15T_F$ and $\mu(T_c) = 0.49T_F$ [46]. Moreover, for the location of the mass-balanced tricritical point we find $k_B T_{c3} = 0.09\varepsilon_{F,\uparrow}$ and $P_{c3} = 0.24$ [71], which is rather close to the experimental data [42]. We included the critical polarization at zero temperature known from Monte Carlo calculations [45], in order to be able to sketch the first-order line and the forbidden region. Other methods are needed to calculate the first-order phase transition more accurately with fluctuation effects taken into account [77]. In Fig. 3.17b, we show the line of second-order phase transitions for the ${}^6\text{Li}-{}^{40}\text{K}$ mixture, when fluctuation effects are included. Compared to the mean-field result of Fig. 3.14b, the critical temperatures are significantly lower. For the positions of the tricritical point and the Lifshitz point, we use Eq. (3.20) and Eq. (3.23), where we again insert the renormalized chemical potentials to include the fermionic selfenergy effects. We then find $k_B T_{c3} = 0.08T_F$ and $P_{c3} = 0.47$, and $k_B T_L = 0.05T_F$ and $P_L = -0.18$, respectively [71]. It is important to note that although the fluctuations have quantitatively a very large effect, the topology of the phase diagrams remains the same.

3.6 Discussion and Conclusion

In this paper we considered Fermi mixtures consisting of two different species of fermions, which can both have a population and a mass imbalance. On the mean-field level we calculated the phase diagrams for those Fermi mixtures as a function of temperature and polarization. We calculated the phase diagrams for different mass ratios and for different interaction strengths, where we found that a mass imbalance leads to a phase diagram that is asymmetrical in the polarization. We also considered the possibility of a Lifshitz instability. We found such instabilities in the Fermi mixtures with a mass ration of $r = 6.7$ and $r = 10$ in the unitarity limit. For a mass-balanced mixture, Lifshitz points occur only in the weakly interacting regime.

By studying the effects of a mass imbalance in more detail we found analytic results for the critical temperature and the change in critical temperature at zero polarization. Furthermore, we investigated what happens to the position of the Lifshitz points and the tricritical points when changing the interaction strength. In the mass-balanced case, we also found a multicritical point for weak interactions. Both for the mass-balanced and the ${}^6\text{Li}-{}^{40}\text{K}$ Fermi mixtures, we calculated the regions where the superfluid phase is gapless in the unitarity limit, i.e., where the mixtures are in the Sarma phase. These regions were present at nonzero temperatures, and turned out to be quite large.

Finally, to obtain more quantitative results we introduced renormalized chemical potentials that include selfenergy effects to account for the resonant interactions. We also took screening effects on the critical temperature into account. In this way, we obtained a phase diagram for the mass-balanced mixture that agrees well with Monte Carlo calculations and with experiment. And we hope to have obtained a good quantitative description of the phase diagram for the ${}^6\text{Li}-{}^{40}\text{K}$ mixture, where especially the presence of a Lifshitz point is exciting. Below the Lifshitz point various supersolid states are competitive. This leads to open questions for further research on the interesting possibility of an inhomogeneous superfluid.

3.7 Appendix: Derivation of the mean-field thermodynamic potential

In this Appendix we explicitly derive the mean-field thermodynamic potential in Eq. (3.13). We start with the microscopic action for an interacting Fermi mixture

consisting of fermions present in two hyperfine states. It is given by

$$S[\phi^*, \phi] = \int_0^{\hbar\beta} d\tau \int d\mathbf{x} \left\{ \sum_{\sigma=\uparrow,\downarrow} \phi_\sigma^*(\mathbf{x}, \tau) \left(\hbar \frac{\partial}{\partial \tau} - \frac{\hbar^2 \nabla^2}{2m_\sigma} - \mu_\sigma \right) \phi_\sigma(\mathbf{x}, \tau) + V_0 \phi_\uparrow^*(\mathbf{x}, \tau) \phi_\downarrow^*(\mathbf{x}, \tau) \phi_\downarrow(\mathbf{x}, \tau) \phi_\uparrow(\mathbf{x}, \tau) \right\}, \quad (3.35)$$

where $V_0 \delta(\mathbf{x} - \mathbf{x}')$ is the bare point-like interaction associated with the short-range atomic potentials. The last term in this action is a fourth-order term in the fermionic fields. Therefore, the integral over the fermionic fields in the partition function

$$Z = \int d[\phi^*] d[\phi] \exp\{-S[\phi^*, \phi]/\hbar\} \quad (3.36)$$

cannot be performed analytically. To deal with this fourth-order term we introduce by means of a Hubbard-Stratonovich transformation bosonic pairing fields $\Delta(\mathbf{x}, \tau)$, which are on average related to the fermionic fields $\phi_\sigma(\mathbf{x}, \tau)$ as in Eq. (3.16). The Hubbard-Stratonovich transformation is performed by inserting into the partition function the following identity

$$1 = \int d[\Delta^*] d[\Delta] e^{(\Delta - \phi_\uparrow \phi_\downarrow V_0 |V_0^{-1}| \Delta^* - V_0 \phi_\downarrow^* \phi_\uparrow^*)/\hbar}, \quad (3.37)$$

where the inner product in the exponent is a short hand notation for

$$\int_0^{\hbar\beta} d\tau \int d\mathbf{x} (\Delta^*(\mathbf{x}, \tau) - \phi_\uparrow^*(\mathbf{x}, \tau) \phi_\downarrow^*(\mathbf{x}, \tau) V_0) V_0^{-1} (\Delta(\mathbf{x}, \tau) - V_0 \phi_\downarrow(\mathbf{x}, \tau) \phi_\uparrow(\mathbf{x}, \tau)). \quad (3.38)$$

Inserting Eq. (3.37) into Eq. (3.36) leaves us with an action $S[\Delta^*, \Delta, \phi^*, \phi]$ which depends only quadratically on the fermionic fields $\phi_\sigma(\mathbf{x}, \tau)$. It is given by

$$S[\Delta^*, \Delta, \phi^*, \phi] = - \int_0^{\hbar\beta} d\tau \int d\mathbf{x} \left\{ \frac{|\Delta(\mathbf{x}, \tau)|^2}{V_0} - \hbar \sum_{\sigma=\uparrow,\downarrow} \int_0^{\hbar\beta} d\tau' \int d\mathbf{x}' \phi_\sigma^*(\mathbf{x}, \tau) G_{0;\sigma}^{-1}(\mathbf{x}, \tau; \mathbf{x}', \tau') \phi_\sigma(\mathbf{x}', \tau') + \phi_\uparrow^*(\mathbf{x}, \tau) \phi_\downarrow^*(\mathbf{x}, \tau) \Delta(\mathbf{x}, \tau) + \Delta^*(\mathbf{x}, \tau) \phi_\downarrow(\mathbf{x}, \tau) \phi_\uparrow(\mathbf{x}, \tau) \right\}. \quad (3.39)$$

The noninteracting Green's function is given by

$$G_{0;\sigma}^{-1}(\mathbf{x}, \tau; \mathbf{x}', \tau') = -\frac{1}{\hbar} \left(\hbar \frac{\partial}{\partial \tau} - \frac{\hbar^2 \nabla^2}{2m_\sigma} - \mu_\sigma \right) \delta(\mathbf{x} - \mathbf{x}') \delta(\tau - \tau'). \quad (3.40)$$

Note that by performing the Hubbard-Stratonovich transformation we have introduced the order parameter $\Delta(\mathbf{x}, \tau)$ in an exact manner into the many-body theory. If we now integrate out the fermionic fields we will be left with an effective action $S^{\text{eff}}[\Delta^*, \Delta]$, which is directly related to the Landau free energy. If we apply mean-field theory we assume that the bosonic fields are position and time independent, i.e., $\Delta(\mathbf{x}, \tau) = \Delta$. In order to integrate out the fermionic fields, we need to diagonalize the action. First, Fourier transforming the above action and then writing it in a more compact way using matrix multiplication yields

$$S[\Delta^*, \Delta, \phi^*, \phi] = -\hbar\beta V \frac{|\Delta|^2}{V_0} - \hbar\beta \sum_{\mathbf{k}} [\varepsilon_{\downarrow}(\mathbf{k}) - \mu_{\downarrow}] \\ - \hbar \sum_{\mathbf{k}, n} [\phi_{n,\uparrow}^*(\mathbf{k}), \phi_{-n,\downarrow}(-\mathbf{k})] \mathbf{G}_{\Delta}^{-1}(\mathbf{k}, i\omega_n) \begin{bmatrix} \phi_{n,\uparrow}(\mathbf{k}) \\ \phi_{-n,\downarrow}^*(-\mathbf{k}) \end{bmatrix}, \quad (3.41)$$

where V is the volume. In the above expression

$$-\hbar \mathbf{G}_{\Delta}^{-1}(\mathbf{k}, i\omega_n) = \begin{pmatrix} -i\hbar\omega_n + \varepsilon_{\uparrow}(\mathbf{k}) - \mu_{\uparrow} & \Delta \\ \Delta^* & -[i\hbar\omega_n + \varepsilon_{\downarrow}(\mathbf{k}) - \mu_{\downarrow}] \end{pmatrix},$$

where ω_n are the odd Matsubara frequencies. By writing the action in matrix form, we have interchanged the fermionic fields ϕ_{\downarrow} and ϕ_{\downarrow}^* and thereby we have picked up a constant term, namely the sum $\Sigma_{\mathbf{k}}[\varepsilon_{\downarrow}(\mathbf{k}) - \mu_{\downarrow}]$ in the first line of Eq. (3.41). We can now diagonalize this action by means of a Bogoliubov transformation. This transformation consists of unitarily transforming the atomic fields $\phi_{n,\sigma}(\mathbf{k})$ to the quasiparticle fields $\psi_{n,\sigma}(\mathbf{k})$

$$\begin{bmatrix} \psi_{n,\uparrow}(\mathbf{k}) \\ \psi_{-n,\downarrow}^*(-\mathbf{k}) \end{bmatrix} = \begin{bmatrix} u(\mathbf{k}) & -v(\mathbf{k}) \\ v^*(\mathbf{k}) & u^*(\mathbf{k}) \end{bmatrix} \cdot \begin{bmatrix} \phi_{n,\uparrow}(\mathbf{k}) \\ \phi_{-n,\downarrow}^*(-\mathbf{k}) \end{bmatrix}, \quad (3.42)$$

where this transformation is unitary if

$$|u(\mathbf{k})|^2 + |v(\mathbf{k})|^2 = 1. \quad (3.43)$$

The coefficients of this transformation can be found by demanding the off-diagonal matrix elements to be zero. The action in terms of the fields $\psi_{n,\sigma}(\mathbf{k})$ then reads

$$S[\Delta^*, \Delta, \psi^*, \psi] = -\hbar\beta V \frac{|\Delta|^2}{V_0} - \hbar\beta \sum_{\mathbf{k}} [\varepsilon(\mathbf{k}) - \mu - \hbar\omega(\mathbf{k})] \\ + \sum_{\mathbf{k}, n} \sum_{\sigma=\uparrow,\downarrow} [-i\hbar\omega_n + \hbar\omega_{\sigma}(\mathbf{k})] \psi_{n,\sigma}^*(\mathbf{k}) \psi_{n,\sigma}(\mathbf{k}), \quad (3.44)$$

where the extra term $\hbar\omega_{\uparrow}(\mathbf{k})$ inside the first sum again comes from interchanging fermionic fields. The mean-field partition function reads after performing the Hubbard-Stratonovich transformation and the Bogoliubov transformation

$$\begin{aligned} Z &= \int d[\psi^*]d[\psi] \exp\{-S[\Delta^*, \Delta, \psi^*, \psi]/\hbar\} \\ &= \exp\left\{\beta V \frac{|\Delta|^2}{V_0} + \text{Tr}[\log(-\mathbf{G}^{-1})]\right\} \\ &= \exp\{-S^{\text{eff}}[\Delta^*, \Delta]/\hbar\}. \end{aligned} \quad (3.45)$$

where \mathbf{G}^{-1} is

$$-\hbar\mathbf{G}^{-1}(\mathbf{k}, i\omega_n) = \begin{pmatrix} i\hbar\omega_n - \hbar\omega_{\uparrow}(\mathbf{k}) & 0 \\ 0 & i\hbar\omega_n - \hbar\omega_{\downarrow}(\mathbf{k}) \end{pmatrix}. \quad (3.46)$$

The interaction V_0 in the effective action can be eliminated in favor of the two-body transition matrix using Eq. (3.4). It is straightforward to calculate the mean-field thermodynamic potential from the effective action, which we find to be

$$\begin{aligned} \omega_L(|\Delta|) &= -\frac{1}{\beta V} \log Z \\ &= -\frac{|\Delta|^2}{T^{2B}(0)} + \int \frac{d\mathbf{k}}{(2\pi)^3} \left\{ \varepsilon(\mathbf{k}) - \mu - \hbar\omega(\mathbf{k}) + \frac{|\Delta|^2}{2\varepsilon(\mathbf{k})} \right. \\ &\quad \left. - \frac{1}{\beta} \sum_{\sigma=\uparrow,\downarrow} \log \left(1 + e^{-\beta\hbar\omega_{\sigma}(\mathbf{k})} \right) \right\}, \end{aligned} \quad (3.47)$$

where to obtain this thermodynamic potential the sum over the Matsubara frequencies was performed using the following identity

$$\sum_n \log[\beta(-i\hbar\omega_n + \varepsilon)] = \log(1 + e^{-\beta\varepsilon}), \quad (3.48)$$

which can be derived using contour integration.

3.8 Appendix: Feynman diagrams

To determine the critical temperature at which a phase transition will take place we can, as mentioned in Section II, either calculate coefficients from the thermodynamic potential by deriving it with respect to $|\Delta|$ or we can use Feynman diagrams. We present the latter scheme in some detail here.

From the action in Eq. (3.39) we can determine the propagator for the fermionic fields and the vertices for the interactions between the fermions and the bosons. Namely the propagator in momentum space is

$$G_{0,\sigma}(\mathbf{k}, i\omega_n) = \frac{-\hbar}{-i\hbar\omega_n + \varepsilon_\sigma(\mathbf{k}) - \mu_\sigma}. \quad (3.49)$$

This propagator is in the Feynman diagrams in Figs. 3.5a and 3.5b represented by a straight line, where the plus (minus) indicates a light (heavy) particle. The interaction vertex is proportional to $\delta(\mathbf{k}_1 + \mathbf{k}_2 + \mathbf{k}_3)\delta_{n,n',n''}$, where \mathbf{k}_i are the momenta and n determine the frequencies of the incoming and outgoing particles. This represents nothing but conservation of momentum and energy. In the diagrams in Figs. 3.5a and 3.5b the vertices are the points where three propagators meet.

In order to determine the Lifshitz point we need an expression for the ladder diagram with nonzero external momenta.

$$\begin{aligned} & \frac{1}{\hbar\beta} \sum_n \int \frac{d\mathbf{k}}{(2\pi)^3} G_{0,\uparrow}(\mathbf{q} - \mathbf{k}, -i\omega_n) G_{0,\downarrow}(\mathbf{k}, i\omega_n) \\ &= \frac{1}{\hbar\beta} \sum_n \int \frac{d\mathbf{k}}{(2\pi)^3} \frac{-\hbar}{i\hbar\omega_n + \varepsilon_\uparrow(\mathbf{q} - \mathbf{k}) - \mu_\uparrow} \frac{-\hbar}{-i\hbar\omega_n + \varepsilon_\downarrow(\mathbf{k}) - \mu_\downarrow}. \end{aligned} \quad (3.50)$$

We can split the fractions and then perform the summation over the Matsubara frequencies. This results in

$$\int \frac{d\mathbf{k}}{(2\pi)^3} \frac{N_\uparrow(\mathbf{q} - \mathbf{k}) + N_\downarrow(\mathbf{k}) - 1}{\varepsilon_\uparrow(\mathbf{q} - \mathbf{k}) + \varepsilon_\downarrow(\mathbf{k}) - 2\mu}.$$

If we want to obtain the full expression for the quadratic part, we have to add the terms proportional to $|\Delta|^2$ from the effective action. By doing so we obtain $\alpha(\mathbf{q})$ in Eq. (3.21). In the same way the diagrams can be calculated needed for α in Eq. (4.5) and for β in Eq. (3.20).

When we include fluctuation effects, we also take the screening of the interaction by the particle-hole fluctuations into account. We do so by replacing the bare interaction potential V_0 by a screened interaction potential V_{sc} containing the infinite sum of so-called RPA bubble diagrams, see Fig. 3.16. The sum over all the bubble diagrams in Fig. 3.16 is a geometric series. Using this, we find the result for the screened interaction Eq. (3.32). Thus, to find the screened interaction, we have to calculate the amplitude of the bubble diagram. The bubble diagram consists of two fermionic propagators with momentum and energy going in opposite directions

through the diagram. The amplitude is given by

$$\frac{1}{\hbar\beta} \sum_n \int \frac{d\mathbf{k}}{(2\pi)^3} \frac{-\hbar}{-i\hbar\omega_n + \varepsilon_\uparrow(\mathbf{k}) - \mu_\uparrow} \frac{-\hbar}{-i\hbar\omega_n + \varepsilon_\downarrow(\mathbf{k}) - \mu_\downarrow}.$$

Writing the above expression as the sum of two fractions and then performing the sum over the Matsubara frequencies results in

$$\hbar\Pi(\mathbf{0}, 0) = \int \frac{d\mathbf{k}}{(2\pi)^3} \frac{N_\uparrow(\mathbf{k}) - N_\downarrow(\mathbf{k})}{2\hbar - [\varepsilon_\uparrow(\mathbf{k}) - \varepsilon_\downarrow(\mathbf{k})]}. \quad (3.51)$$

C HAPTER 4

Inhomogeneous superfluid phases in ${}^6\text{Li}$ - ${}^{40}\text{K}$ mixtures at unitarity.

Abstract — We show that the ultracold three-dimensional ${}^6\text{Li}$ - ${}^{40}\text{K}$ mixture at unitarity can exhibit the highly exotic Larkin-Ovchinnikov superfluid phase.¹ We determine the phase diagram for majorities of ${}^{40}\text{K}$ atoms within mean-field theory taking the inhomogeneities of the fermion states into account exactly. We find two different inhomogeneous superfluid phases in mixtures with a majority of ${}^{40}\text{K}$ atoms, namely the Larkin-Ovchinnikov (LO) phase with one inhomogeneous direction and a cubic phase (LO³) where three spatial translational symmetries are broken. We determine the transition between these two phases by solving the Bogoliubov-de Gennes equations in the superfluid LO phase. Subsequently, we calculate the atomic density modulation of the atoms in the LO phase and show that it is sufficiently large to be visible in experiment.

4.1 Introduction

Since the first realization of superfluidity in a two-component gas of fermionic atoms a large number of exciting experiments have been performed. For instance, with the use of a Feshbach resonance the inter-particle interactions can be tuned and hereby the crossover between the Bose-Einstein condensation of molecules and Cooper pairs was studied [27, 29]. By inducing spin flips in a Fermi gas the number of particles in different spin states can be changed, opening up the possibility of studying the influence of a population imbalance on the phase transition to a superfluid state. This possibility has indeed been materialized in a two-component

¹This chapter is directly based on J. E. Baarsma and H. T. C. Stoof, *Inhomogeneous superfluid phases in ${}^6\text{Li}$ - ${}^{40}\text{K}$ mixtures at unitarity*, Phys. Rev. A **87**, 063612 (2013).

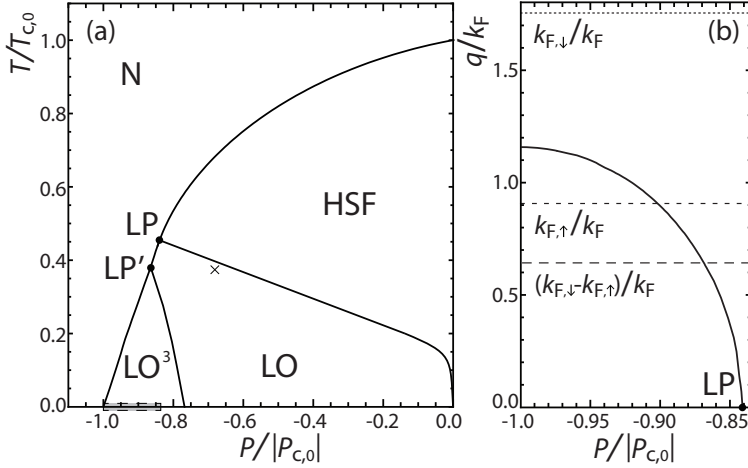


Figure 4.1: Phase diagram for the unitary mixture of ^6Li and ^{40}K atoms (a). Each full line denotes a continuous phase transition. The grey rectangle on the horizontal axis sets the scale for panel (b), where along the line of phase transitions to an inhomogeneous superfluid the wavevector q associated with the periodicity is shown. Also shown are the Fermi wavevectors of the $^6\text{Li}(\uparrow)$ and $^{40}\text{K}(\downarrow)$ atoms and their difference, all at $T = 0$ and $P = P_{c,0}$.

gas of ^6Li atoms and the phase diagram turns out to be governed by a tricritical point below which the gas phase separates into a superfluid and normal region [3, 42, 47, 76].

One of the exotic states of matter that may also be realized in a system of ultracold Fermi atoms is a superfluid where the Cooper pairs have a nonzero center-of-mass momentum. The first to propose this possibility in the context of superfluid films in a magnetic field were Fulde and Ferrel (FF) [80] and independently Larkin and Ovchinnikov (LO) [79]. Signatures of these so called FFLO phases have been seen in an atomic gas in one spatial dimension [82], but a decisive experiment that observes the FFLO correlations has not been carried out yet. In three spatial dimensions a phase with nonzero momentum Cooper pairs is predicted to be present in the population imbalanced Fermi gas with weak interactions [81, 83, 84, 98, 99]. However, the transition temperatures in a weakly interacting Fermi gas are very low and are expected to be out of reach with present cooling techniques. In the three-dimensional strongly interacting mixture of ^6Li and ^{40}K atoms a Lifshitz instability towards a phase with nonzero momentum

Cooper pairs is present at an attainable temperature [71, 72], but the precise form of this superfluid phase has not yet been determined. In this paper we show that at temperatures below the Lifshitz point the Fermi gas will form the exotic LO phase, which shares the properties of both a solid and a superfluid and is therefore a special kind of supersolid. This is a very exciting prospect, because even though this new kind of superfluid was first proposed by Larkin and Ovchinnikov already in 1964 [79], it has never been observed in a three-dimensional fluid. In the ${}^6\text{Li}-{}^{40}\text{K}$ mixture important steps have already been made experimentally. The Feshbach resonances of the mixture were known for some time [5, 6], and now also expansion under the influence of strong interactions from an optical dipole trap has been realized [35], a large atom number dual-species magneto-optical trap was built [36], and the repulsive polaron has been studied in this mixture [37]. At present, therefore, an ultra-cold ${}^6\text{Li}-{}^{40}\text{K}$ mixture at unitarity is to the best of our knowledge one of the most promising systems available in the laboratory to observe such a three-dimensional supersolid in a locally homogeneous trapping geometry and study its properties in detail with the accuracy of atomic physics. In addition, there recently have been proposals to observe FF and LO states in the presence of optical lattices [100] and to observe FF states in cold atom systems with spin-orbit coupling [101, 102].

The LO state is also expected to be present in a number of other condensed-matter systems, such as in superfluid ${}^3\text{He}$ in the presence of a magnetic field [103], neutron stars [39] and heavy-fermion systems [104]. In the context of colorsuperconductivity a large body of theoretical work has been concerned with different inhomogeneous phases [105–109], all considering weak coupling and using Ginzburg-Landau expansions of the free energy. Although continuous (second-order) instabilities can be determined exactly using this expansion, the downfall is that ruling out discontinuous (first-order) transitions is impossible and one is moreover forced to remain close to the normal-superfluid transition.

In this paper we calculate for different superfluid phases where time-reversal or translational symmetry is broken the full thermodynamic potential within mean-field theory, with which both continuous and discontinuous phase transitions can be described. Moreover, in contrast to previous work, it enables us to describe transitions within the superfluid phase. In this manner we complete the phase diagram of the mixture of ${}^6\text{Li}-{}^{40}\text{K}$ atoms for a majority of ${}^{40}\text{K}$ atoms, see Fig. 2(a), and especially what the structure of the inhomogeneous superfluid is. For a majority of ${}^6\text{Li}$ atoms it was shown already that a tricritical point is present, below which a discontinuous phase transition towards a homogeneous superfluid, and thus phase separation, occurs [71]. We find for small negative polarizations $P = (n_{\uparrow} - n_{\downarrow})/(n_{\uparrow} + n_{\downarrow})$, where $n_{\uparrow(\downarrow)}$ denotes the density of ${}^6\text{Li}({}^{40}\text{K})$ atoms, a continuous

transition from the normal state (N) to a homogeneous superfluid (HSF), up to the Lifshitz point (LP). For larger majorities of ^{40}K atoms there is a continuous phase transition to an inhomogeneous superfluid phase where translational symmetry is broken in one spatial direction (LO) and from the point LP' on the continuous transition is to a phase where translational symmetry is broken in three directions (LO³). In Fig. 2(a) the temperature T is scaled by the critical temperature $T_{c,0}$ at $P = 0$ and the polarization P is scaled by the critical polarization $|P_{c,0}|$ at $T = 0$, because interaction effects in first instance only shift the location of the Lifshitz point [71, 72], as we explain below.

This paper is organized as follows. We first explain how we calculate, within a mean-field approximation, the full thermodynamic potential for different inhomogeneous superfluid phases and how we obtain the phase diagram in Fig. 2(a). In Sec. 4.3 we describe the Ginzburg-Landau expansion of the different free energies. We show that from comparing the expansion coefficients it can be directly seen which inhomogeneous superfluid phase is the most favorable. Subsequently, we discuss the possibility of having a linear superposition of the LO and the LO³ phases and show that this does not occur. In Sec. 4.4 we explain how we calculate the transition line between the LO and LO³ inhomogeneous phases in a direct manner. Finally, in Sec. 4.5, we determine the densities for the two atomic species in the LO phase at the conditions of the cross in Fig. 2(a), which are now position dependent with a modulation that can be as big as 10% over one period. This is therefore a convenient signature for the LO phase in experiment, but also other proposals to observe this exotic state of matter have been made [110, 111].

In this paper we calculate the phase diagram for the ^6Li - ^{40}K mixture within a mean-field approximation, which does not include all important physical effects such as, for instance, the screening of the interaction by particle-hole fluctuations. It is known that in the strongly interacting limit these effects play an important role and mean-field theory does not give good quantitative results. However, the phase diagram for the unitary Fermi mixture with population imbalance predicted by mean-field theory was reproduced qualitatively by renormalization-group calculations that do incorporate fluctuation and interaction effects [47] and, more importantly, that are in agreement with the phase diagram mapped out experimentally [3, 42, 76]. From this it can be concluded that for these purposes the mean-field calculation already contains the relevant physics, even at unitarity. The Lifshitz point found in the ^6Li - ^{40}K mixture using mean-field theory remains present when adding screening and selfenergy effects and its position only changes quantitatively [71, 72]. This qualitative success of mean-field theory is, physically, due to the fact that even at unitarity the atomic selfenergies are well approximated by a momentum and frequency independent constant. As a result, thermodynamic

instabilities are determined by mean-field-like correlation functions with strongly renormalized constants that lead to quantitative shifts only in the transition lines. In conclusion, mean-field theory is even at unitarity a good first approximation to explore the superfluid phases that can occur in the ${}^6\text{Li}-{}^{40}\text{K}$ mixture and map out the phase diagram, which is the main aim of this paper.

4.2 Thermodynamic potential

Phase transitions can be determined by studying the Landau free energy of a system as a function of the appropriate order parameter. Here, the role of the Landau free energy is played by the grand-canonical thermodynamic potential $\Omega(\Delta)$, where Δ , the gap parameter describing the condensate of Cooper pairs, is the order parameter for the phase transition from the normal state to a superfluid.

We can calculate the thermodynamic potential Ω for the two-component Fermi gas with mass and population imbalance from the microscopic action

$$S = \int d\mathbf{x}d\tau \left\{ \sum_{\sigma=\uparrow,\downarrow} \phi_\sigma^* \left(\hbar \frac{\partial}{\partial \tau} - \frac{\hbar^2 \nabla^2}{2m_\sigma} - \mu_\sigma \right) \phi_\sigma - \frac{|\Delta|^2}{V_0} + \phi_\uparrow^* \phi_\downarrow^* \Delta + \Delta^* \phi_\downarrow \phi_\uparrow \right\}, \quad (4.1)$$

where $\phi_\sigma(\mathbf{x}, \tau)$ are Grassmann-valued fields describing fermions. In the case under study, $\uparrow(\downarrow)$ denotes a ${}^6\text{Li}({}^{40}\text{K})$ atom with mass $m_{\uparrow(\downarrow)}$. A population imbalance between the two atomic species is introduced by having different chemical potentials μ_σ for the two species, resulting in different densities, since $n_\sigma = -\partial\Omega/\partial\mu_\sigma$. The microscopic interaction strength between the fermionic atoms is denoted by V_0 and is attractive here. The last two terms in the above action represent respectively the annihilation and creation of a Cooper pair, described by the bosonic complex pairing field $\Delta(\mathbf{x}, \tau)$, consisting here of a ${}^6\text{Li}$ and a ${}^{40}\text{K}$ atom.

From the action the partition function can be calculated as

$$Z = \int d[\phi^*] d[\phi] d[\Delta^*] d[\Delta] e^{-S[\phi, \Delta]/\hbar} \quad (4.2)$$

and subsequently the thermodynamic potential can be obtained via $\Omega = -\log Z/\beta$, where $1/\beta = k_B T$ is the inverse thermal energy with k_B Boltzmann's constant.

In the partition function Z not all path integrals can be evaluated exactly and therefore we use a mean-field approximation to calculate the thermodynamic potential. In this approximation the pairing field is replaced by its most probable value and the associated path integral omitted. In practice the thermodynamic potential is then obtained by making an ansatz for the pairing field and thus for the

superfluid phase. The thermodynamic potential describing the phase transition from a normal gas to a homogeneous BCS superfluid, with both time-reversal and translational symmetry present, is calculated by taking for the pairing field $\Delta(\mathbf{x}, \tau) = \Delta_0$. Thus, a Cooper pair consists here of two fermions with opposite momentum, such that the pair has no net momentum.

Fulde and Ferrel considered a plane wave for the pairing field, $\Delta_{\text{FF}}(\mathbf{x}, \tau) = \Delta_0 e^{i\mathbf{q} \cdot \mathbf{x}}$, in which case a Cooper pair has net momentum \mathbf{q} . The superfluid described hereby still obeys translational symmetry but time-reversal symmetry is broken. After replacing the pairing field in Eq. (4.1) by the FF ansatz and using a Matsubara expansion for the fermionic fields,

$$\phi_\sigma(\mathbf{x}, \tau) = \sum_{\mathbf{k}, n} \phi_{\sigma, \mathbf{k}, n} \frac{e^{i(\mathbf{k} \cdot \mathbf{x} - i\omega_n \tau)}}{\sqrt{\hbar\beta V}}, \quad (4.3)$$

where the summation over n runs over the odd Matsubara frequencies ω_n , the terms describing the creation and annihilation of a Cooper pair read

$$\sum_n \sum_{\mathbf{k}} \left\{ \phi_{\uparrow, \mathbf{k}, n} \phi_{\downarrow, -\mathbf{k} + \mathbf{q}, -n} \Delta_0 + \text{c.c.} \right\}. \quad (4.4)$$

The action can now be rewritten using matrix multiplication after which it reads

$$S = -\hbar\beta V \frac{|\Delta_0|^2}{V_0} + \sum_{\mathbf{k}} \left\{ \hbar\beta (\varepsilon_{\downarrow, -\mathbf{k} + \mathbf{q}} - \mu_\downarrow) + \sum_n \Phi^\dagger \begin{pmatrix} -i\hbar\omega_n + \xi_{\uparrow, \mathbf{k}} & \Delta_0 \\ \Delta_0 & -i\hbar\omega_n - \xi_{\downarrow, -\mathbf{k} + \mathbf{q}} \end{pmatrix} \Phi \right\}, \quad (4.5)$$

where $\Phi_{\mathbf{k}, n}^\dagger = [\phi_{\uparrow, \mathbf{k}, n}^*, \phi_{\downarrow, -\mathbf{k} + \mathbf{q}, -n}]$ and V is the volume. The kinetic energy of a fermionic atom in state $|\sigma\rangle$ is $\varepsilon_{\sigma, \mathbf{k}} = \hbar^2 k^2 / 2m_\sigma$ and $\xi_{\sigma, \mathbf{k}} = \varepsilon_{\sigma, \mathbf{k}} - \mu_\sigma$. The above action can be diagonalized analytically by making a Bogoliubov transformation. Subsequently, the integral over the fermionic fields can be evaluated, after which the thermodynamic potential reads

$$\begin{aligned} \Omega_{\text{FF}}(\Delta_0, q) = \frac{1}{V} \int \frac{d\mathbf{k}}{(2\pi)^3} & \left\{ \frac{|\Delta_0|^2}{2\varepsilon_{\mathbf{k}}} + \omega_{\mathbf{k}, \mathbf{q}} - \sqrt{\omega_{\mathbf{k}, \mathbf{q}}^2 + |\Delta_0|^2} \right. \\ & \left. - \frac{1}{\beta} \sum_\sigma \log [1 + e^{-\beta\hbar\omega_{\sigma, \mathbf{k}, \mathbf{q}}}] \right\} - \frac{|\Delta_0|^2}{T^{2B}(0)}, \end{aligned} \quad (4.6)$$

where we replaced the summation over \mathbf{k} by an integral, because we are interested in the thermodynamic limit. The kinetic energy $\varepsilon_{\mathbf{k}} = \hbar^2 k^2 / 2m$ is associated with

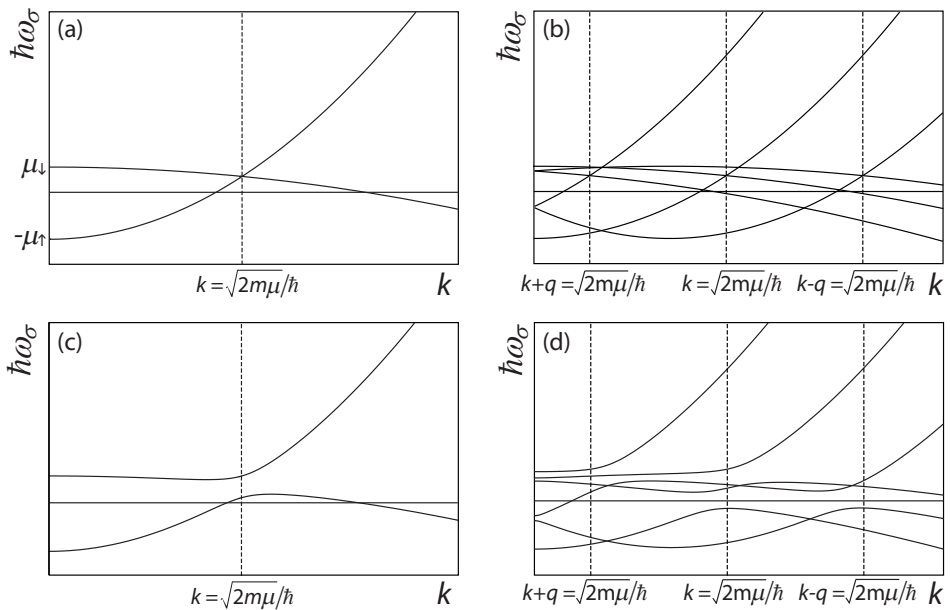


Figure 4.2: Dispersions for the Bogoliubov quasiparticles in the homogeneous case, panel (a) and (c), and in the LO case, panel (b) and (d), for \mathbf{k} parallel to the lattice wavevector \mathbf{q} . The upper panels are dispersions of the Fermi gas in the normal state, where the gap is zero $\Delta_0 = 0$. The lower two panels depict dispersions with a nonzero gap Δ_0

twice the reduced mass, $m = 2m_\uparrow m_\downarrow / (m_\uparrow + m_\downarrow)$, and the dispersions describing the Bogoliubov quasiparticles read

$$\hbar\omega_{\sigma,\mathbf{k},\mathbf{q}} = \sqrt{\omega_{\mathbf{k},\mathbf{q}}^2 + |\Delta_0|^2} + \frac{\sigma}{2} [\varepsilon_{\uparrow,\mathbf{k}} - \varepsilon_{\downarrow,-\mathbf{k}+\mathbf{q}} - 2h], \quad (4.7)$$

with $\omega_{\mathbf{k},\mathbf{q}} = [\varepsilon_{\uparrow,\mathbf{k}} + \varepsilon_{\downarrow,-\mathbf{k}+\mathbf{q}} - 2\mu]/2$, where $\mu = (\mu_\uparrow + \mu_\downarrow)/2$ is the average chemical potential. Above, $\sigma = +1(-1)$ for $\uparrow(\downarrow)$ atoms and $h = (\mu_\uparrow - \mu_\downarrow)/2$ is the chemical potential difference. In the thermodynamic potential we replaced the microscopic interaction V_0 by the two-body transition matrix T^{2B}

$$\frac{1}{V_0} = \frac{1}{T^{2B}(0)} - \frac{1}{V} \sum_{\mathbf{k}} \frac{1}{2\varepsilon_{\mathbf{k}}}, \quad (4.8)$$

which is related to the s -wave scattering length a , $1/T^{2B}(0) = m/4\pi\hbar^2a$. Experimentally, the scattering length can be controlled by the use of a Feshbach resonance. In this paper we consider the unitarity regime, where $1/|a| = 0$.

The above thermodynamic potential describes the transition from a normal gas to the homogeneous BCS superfluid, with time-reversal symmetry, when the momentum \mathbf{q} of the Cooper pairs is set to zero, i.e., $\Omega_{BCS}(\Delta_0) = \Omega_{FF}(\Delta_0, 0)$. Correspondingly, for $\mathbf{q} = 0$ the dispersions in Eq. (4.7) describe the Bogoliubov quasiparticles in the homogeneous superfluid, see Fig. 4.2.

Larkin and Ovchinnikov made an ansatz for the Cooper pair that results in a truly inhomogeneous superfluid, but with time-reversal symmetry unbroken. Namely, they assumed a standing wave,

$$\Delta_{LO}(\mathbf{x}, \tau) = \frac{\Delta_0}{\sqrt{2}} [e^{i\mathbf{q}\cdot\mathbf{x}} + e^{-i\mathbf{q}\cdot\mathbf{x}}], \quad (4.9)$$

in which case not only the Cooper-pair phase but also the superfluid density becomes position dependent. Plugging the LO ansatz in Eq. (4.1) results in the following expression for the Cooper-pair terms

$$\frac{1}{\sqrt{2}} \sum_n \sum_{\mathbf{k}} \left\{ \phi_{\uparrow,\mathbf{k},n} \phi_{\downarrow,-\mathbf{k}+\mathbf{q},-n} \Delta_0 + \text{c.c.} + \phi_{\uparrow,\mathbf{k},n} \phi_{\downarrow,-\mathbf{k}-\mathbf{q},-n} \Delta_0 + \text{c.c.} \right\}, \quad (4.10)$$

where an important difference with the previous ansatz is that via the pairing field now every fermionic field component $\phi_{\sigma,\mathbf{k},n}$ couples to two other components, $\phi_{-\sigma,-\mathbf{k}+\mathbf{q},-n}$ and $\phi_{-\sigma,-\mathbf{k}-\mathbf{q},-n}$, instead of only to $\phi_{-\sigma,-\mathbf{k}+\mathbf{q},-n}$. This has important consequences for the computation of the thermodynamic potential Ω_{LO} . Namely, rewriting the action using matrix multiplication here not yields a 2×2 matrix but one with infinite dimensions. In order to perform a calculation we truncate this matrix and thus neglect some couplings. The smallest matrix we

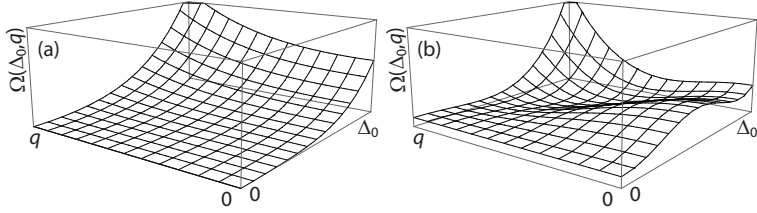


Figure 4.3: The thermodynamic potential for the LO configuration, as a function of the amplitude of the gap Δ_0 and the lattice wavevector q . In panel (a) the Fermi gas is in the normal state, whereas in panel (b) a transition to an inhomogeneous superfluid has occurred. Namely, the global omnimum of the thermodynamic potential in panel (b) lies at nonzero Δ_0 and q .

consider has dimension $D = 6$ and after diagonalizing we find six dispersions $\hbar\omega_i$, see Fig. 4.2. Notice that if the gap is zero, Fig. 4.2(a) and (b), the dispersions are the same as the homogeneous dispersions, only displaced by the lattice wavevector \mathbf{q} . While, if there is a nonzero gap, Fig. 4.2(c) and (d), the LO case is truly different from the homogeneous superfluid since a band structure appears.

With the LO quasiparticle dispersions the thermodynamic potential Ω_{LO} can be calculated, where attention should be paid to a few differences with the homogeneous calculation. Firstly, if a $D \times D$ dimensional matrix is used then Ω_{LO} contains a summation over D dispersions, while we only describe two species of fermions. To compensate for this, we have to multiply the summation by $2/D$.

Secondly, the integrand in the thermodynamic potential needs to be convergent in order to be able to evaluate the integral over momentum. In the homogeneous case, and also in the FF case, there are several divergencies in the integrand that exactly cancel against each other in the limit $k \rightarrow \infty$. In particular, the divergency $-m|\Delta_0|^2/k^2$, coming from the square root in Eq. (4.6) and originating from diagonalizing the matrix in Eq. (4.5), cancels against $|\Delta_0|^2/2\varepsilon_{\mathbf{k}}$ originating from replacing the microscopic interaction V_0 by the s -wave scattering length a .

In the present LO case, the latter divergency enters the thermodynamic potential in the same manner, while the matrix to be diagonalized differs and moreover is truncated, whereby some couplings are neglected. This truncation causes the two divergencies to not cancel in the limit $k \rightarrow \infty$ and we need to account for this. If the matrix has dimension D , there are D momenta involved and there should thus be $2D$ couplings, see Eq. (4.10). However, there are only $2D - 4$ coupling terms accounted for after the truncation, which means that every fermionic field component couples on average to $(2D - 4)/D$ other fermionic components. We

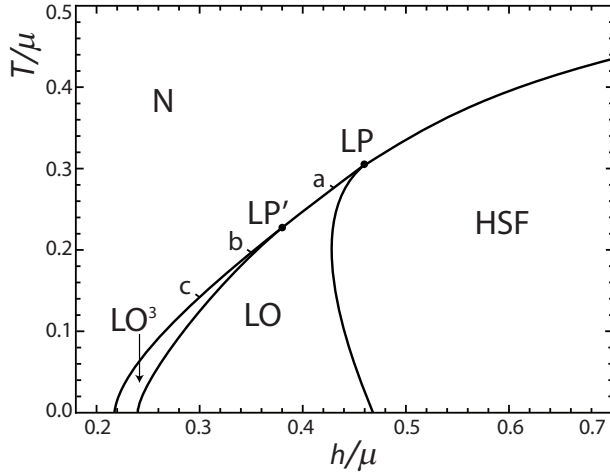


Figure 4.4: Phase diagram for the unitary mixture of ${}^6\text{Li}$ and ${}^{40}\text{K}$ atoms as a function of temperature T and the chemical potential difference h , both scaled by the average chemical potential μ . Each full line denotes a continuous phase transition.

multiply the term originating from replacing V_0 by a by this number divided by two, such that the divergencies cancel again and the integral can be evaluated. Note that in the limit $D \rightarrow \infty$ this prefactor is equal to 1 again, $(2D - 4)/2D \rightarrow 1$.

Finally, the thermodynamic potential should not depend on the dimension of the matrix. We calculated the thermodynamic potential for increasing matrix size to check convergence. At the phase transition convergence is rapid, because we find a second-order phase transition and the gap Δ_0 is small, while we need to go to larger matrix dimensions inside the superfluid phase.

The thermodynamic potential for the LO case is plotted in Fig. 4.3 for different chemical potentials and temperatures. In panel (a) the Fermi gas is in the normal state, whereas in panel (b) a phase transition has occurred. There the global minimum is located at nonzero gap and lattice wavevector q and it can be seen that the global minimum shifted from zero in a continuous fashion to this position.

Obviously, many other choices for the Cooper-pair wavefunction can be made, which all result, by following the steps described above, in a different thermodynamic potential describing a particular phase transition. We calculated the thermodynamic potential for different ansatzes and find for real wavefunctions, such as the LO ansatz, higher critical temperatures than for complex wavefunctions, such as the FF ansatz, which means that phases where time-reversal symmetry is

unbroken are more favorable. Also inside the superfluid phase the states without time-reversal symmetry never form the ground state, because the real ansatzes always give a lower thermodynamic potential. We compared different configurations of standing waves for the Cooper-pair wavefunction. Namely, we calculated Ω for two (LO²) and three (LO³) perpendicular standing waves with equal amplitudes, where the Cooper-pair ansatzes are

$$\Delta_{\text{LO}^2}(\mathbf{x}, \tau) = \frac{\Delta_0}{\sqrt{4}} [e^{iqz} + e^{-iqz} + e^{iqx} + e^{-iqx}], \quad (4.11)$$

$$\Delta_{\text{LO}^3}(\mathbf{x}, \tau) = \frac{\Delta_0}{\sqrt{6}} [e^{iqz} + e^{-iqz} + e^{iqx} + e^{-iqx} + e^{iqy} + e^{-iqy}], \quad (4.12)$$

and for a triangular and tetrahedral configuration of standing waves with equal amplitudes. By comparing the thermodynamic potentials we completed the phase diagram for the Fermi mixture of ⁶Li and ⁴⁰K atoms, see Figs. 2(a) and 4.4. We find that the transition from the normal gas to the inhomogeneous superfluid phase is continuous, i.e., of second order, independently of the structure of the inhomogeneous phase. For all configurations we find the same critical temperature. The lattice wavevector, i.e., the value of q for which the thermodynamic potential $\Omega(\Delta_0, q)$ has a global minimum, along the line of the phase transition is shown in Fig. 2(b). It can be seen that for $T = 0$ it differs from the difference in Fermi wavevectors, which is due to the fact that we are in the strongly interacting regime. We found that inside the LO superfluid phase the global minimum of the thermodynamic potential shifts continuously from a nonzero to a zero lattice wavevector q , in which case the superfluid is homogeneous again. This criterion for the transition between the inhomogeneous and homogeneous superfluid is equivalent to the vanishing of the domain-wall energy [84, 98].

4.3 Ginzburg-Landau expansion

Since we have just found that the phase transition from the normal gas to the inhomogeneous superfluid is continuous we can use a Ginzburg-Landau expansion of the thermodynamic potential

$$\Omega(\Delta_0, q) \simeq \alpha(q)|\Delta_0|^2 + \frac{\beta(q)}{2}|\Delta_0|^4 + \dots \quad (4.13)$$

A second-order phase transition occurs the moment $\alpha(q)$ changes sign. The coefficients in the above expansion can be calculated by taking derivatives of the

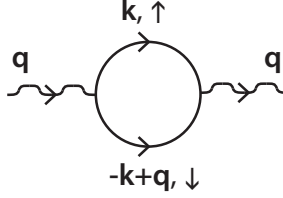


Figure 4.5: Feynman diagram. Wiggly lines denote pairing fields and straight lines denote the fermionic propagators.

thermodynamic potential, for example

$$\alpha(q) = \left. \frac{\partial \Omega(\Delta_0, q)}{\partial |\Delta_0|^2} \right|_{\Delta_0=0}. \quad (4.14)$$

Equivalently, the coefficients can be determined by calculating the amplitude of the proper Feynman diagram [94]. The advantage of using Feynman diagrams instead of derivatives here is that the former is an exact linear-response calculation in the normal state where we do not have to solve a matrix problem of infinite dimensions.

The second-order coefficient α is related to the Feynman diagram shown in Fig. 4.5. The external legs correspond to pairing fields Δ , while the internal lines represent fermionic propagators ϕ_σ . The amplitude of this diagram is given by

$$\frac{1}{\hbar\beta} \sum_n \int \frac{d^3\mathbf{k}}{(2\pi)^3} G_{0;\uparrow}(\mathbf{k}, i\omega_n) G_{0;\downarrow}(-\mathbf{k} + \mathbf{q}, -i\omega_n), \quad (4.15)$$

where $G_{0,\sigma}^{-1}(\mathbf{k}, i\omega_n) = -i\omega_n + \varepsilon_{\sigma,\mathbf{k}} - \mu_\sigma$ is the inverse non-interacting Green's function describing a fermionic atom in state $|\sigma\rangle$. After splitting the fractions and summing over the Matsubara frequencies it reads

$$\alpha(q) = \int \frac{d\mathbf{k}}{(2\pi)^3} \left\{ \frac{1}{2\varepsilon_{\mathbf{k}}} + \frac{N_F(\xi_{\uparrow,\mathbf{k}}) + N_F(\xi_{\downarrow,-\mathbf{k}+\mathbf{q}}) - 1}{\xi_{\uparrow,\mathbf{k}} + \xi_{\downarrow,-\mathbf{k}+\mathbf{q}}} \right\}, \quad (4.16)$$

where the first term originates from the term quadratic in Δ in Eq. (4.1) and the second term is the amplitude of the Feynman diagram. The Fermi distribution functions are given by $N_F(x) = 1/\exp(\beta x + 1)$. The quadratic coefficient for a given lattice configuration is now obtained by summing the above expression over the lattice wavevectors and multiplying it by the normalization squared of $\Delta(\mathbf{x})$, which in the LO case yields for example

$$\alpha_{\text{LO}}(q) = \frac{1}{2} [\alpha(q) + \alpha(-q)] = \alpha(q), \quad (4.17)$$

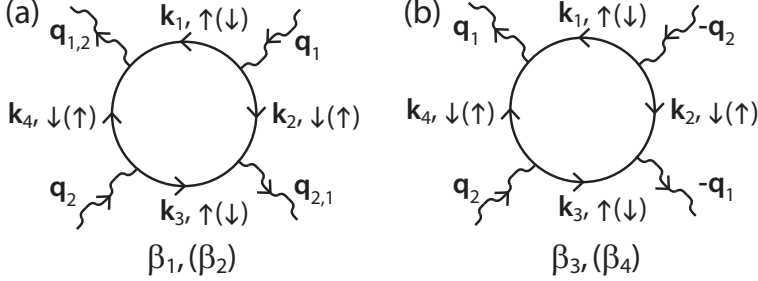


Figure 4.6: The fourth-order diagrams of which we need to calculate the amplitude. External momenta are nonzero, while the external bosonic Matsubara frequencies are equal to zero. The Matsubara frequencies are not shown in this figure.

because this ansatz contains two momenta, \mathbf{q} and $-\mathbf{q}$. Determining this coefficient for other wavefunctions, leads to the conclusion that the α coefficient is the same for every lattice configuration, which confirms our findings from the full thermodynamic potentials. Namely, we find a continuous phase transition at a critical temperature independent of the lattice configuration. Thus, to compare the different lattice configurations we need to look at the fourth-order coefficient $\beta(q)$ in the expansion in Eq. (4.13).

This coefficient can be calculated from the amplitudes of all the diagrams with four external legs, shown in Fig. 4.6. In the case of nonzero external momenta and in the presence of a mass and population imbalance there are four distinct diagrams with four external legs, which are denoted by β_i in Fig. 4.6. Without external momentum all these diagrams give the same amplitude. Without mass and population imbalance there are only two distinct diagrams, namely in the balanced case $\beta_1 = \beta_2$ and $\beta_3 = \beta_4$. Moreover, $\beta_{3,4}$ are only different from $\beta_{1,2}$ if the angle between the two external momenta is not equal to zero or π . In all lattice configurations we consider the lengths of the lattice wavevectors are the same, which means that $|\mathbf{q}_1| = |\mathbf{q}_2| = q$, because this minimizes the quadratic part $\alpha(q)$ of the Ginzburg-Landau expansion. The amplitudes then only depend on the magnitude q and the angle between the external momenta, i.e., $\beta(\mathbf{q}_1, \mathbf{q}_2) = \beta(q, \theta)$. The amplitude of the diagrams in Fig. 4.6(a) are given by

$$\begin{aligned} \beta_{1,2}(q, \theta) &= \frac{1}{\hbar\beta} \sum_n \int \frac{d\mathbf{k}}{(2\pi)^3} G_{0;\sigma}(\mathbf{k} + \mathbf{q}_1 - \mathbf{q}_2, i\omega_n) \\ &\cdot G_{0;-\sigma}(\mathbf{q}_2 - \mathbf{k}, -i\omega_n) G_{0;\sigma}(\mathbf{k}, i\omega_n) G_{0;-\sigma}(\mathbf{q}_2 - \mathbf{k}, -i\omega_n), \end{aligned} \quad (4.18)$$

where we already used conservation of frequency and momentum at all vertices. Again fractions can be split and the sum over the Matsubara frequencies performed. The resulting expression becomes rather lengthy and is omitted here. The diagrams in Fig. 4.6(b) yield similar expressions, namely

$$\begin{aligned} \beta_{3,4}(q, \theta) = & \frac{1}{\hbar\beta} \sum_n \int \frac{d\mathbf{k}}{(2\pi)^3} G_{0;\sigma}(\mathbf{k} + \mathbf{q}_1 - \mathbf{q}_2, i\omega_n) \\ & \cdot G_{0;-\sigma}(-\mathbf{q}_1 - \mathbf{k}, -i\omega_n) G_{0;\sigma}(\mathbf{k}, i\omega_n) G_{0;-\sigma}(\mathbf{q}_2 - \mathbf{k}, -i\omega_n). \end{aligned} \quad (4.19)$$

To obtain the fourth-order coefficient for a given lattice configuration we sum the relevant diagrams and multiply with the normalization factor to the power 4. The expression for $\beta(q)$ for the LO ansatz reads

$$\beta_{\text{LO}}(q) = \frac{1}{4} \left[2\beta_{1+2}(q, 0) + 4\beta_{1+2}(q, \pi) \right], \quad (4.20)$$

where β_{1+2} is short-hand notation for $\beta_1 + \beta_2$. Here, if the external momenta are equal in $\beta_{1,2}$, $\mathbf{q}_1 = \mathbf{q}_2$, there are two possibilities for \mathbf{q}_1 , namely \mathbf{q} and $-\mathbf{q}$, which explains the factor 2 in front of $\beta_{1+2}(q, 0)$ above. In the case of unequal external momenta there are four possibilities for $\beta_{1,2}$. Namely, there are two choices for \mathbf{q}_1 , after which \mathbf{q}_2 is fixed. Subsequently, there are still two possibilities for the outgoing momenta, denoted by $\mathbf{q}_{1,2}$ in Fig. 4.6(a), which makes 4 possibilities in total. In the LO coefficient $\beta_{3,4}$ does not occur. In the case of the LO² ansatz the expression for $\beta(q)$ reads

$$\beta_{\text{LO}^2}(q) = \frac{1}{16} \left[4\beta_{1+2}(q, 0) + 8\beta_{1+2}(q, \pi) + 16\beta_{1+2}(q, \frac{\pi}{2}) + 8\beta_{3+4}(q, \frac{\pi}{2}) \right], \quad (4.21)$$

where the numerical factors are obtained using the same reasoning as above. The LO³ coefficient is given by

$$\beta_{\text{LO}^3}(q) = \frac{1}{36} \left[6\beta_{1+2}(q, 0) + 12\beta_{1+2}(q, \pi) + 48\beta_{1+2}(q, \frac{\pi}{2}) + 24\beta_{3+4}(q, \frac{\pi}{2}) \right]. \quad (4.22)$$

Finally, the triangular configuration leads to the expression

$$\begin{aligned} \beta_{\text{triangular}}(q) = & \frac{1}{36} \left[6\beta_{1+2}(q, 0) + 12\beta_{1+2}(q, \pi) + 24\beta_{1+2}(q, \frac{\pi}{3}) \right. \\ & \left. + 24\beta_{1+2}(q, \frac{2\pi}{3}) + 24\beta_{3+4}(q, \frac{\pi}{3}) \right], \end{aligned} \quad (4.23)$$

while the tetrahedral configuration yields

$$\begin{aligned} \beta_{\text{tetrahedral}}(q) = & \frac{1}{48} \left[8\beta_{1+2}(q, 0) + 16\beta_{1+2}(q, \pi) + 48\beta_{1+2}(q, \phi_0) \right. \\ & \left. + 48\beta_{1+2}(q, \pi - \phi_0) + 48\beta_{3+4}(q, \phi_0) \right], \end{aligned} \quad (4.24)$$

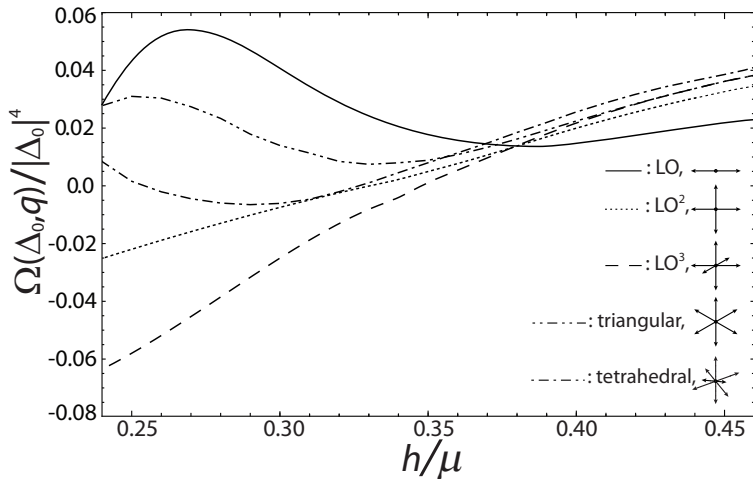


Figure 4.7: The thermodynamic potential along the normal to superfluid transition line from Fig. 4.4(a). At first the LO (solid line) gives the lowest thermodynamic potential, while for larger population imbalances this is true for the LO^3 phase (dashed line). An LO^2 phase (dotted) or more complicated configurations (dashed-dotted and dashed-double-dotted) never form the equilibrium state of this system.

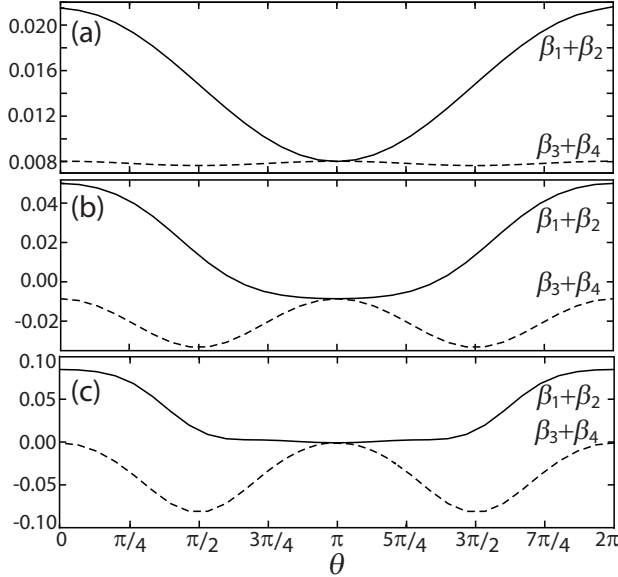


Figure 4.8: Amplitudes of the fourth-order diagrams as a function of the angle θ between \mathbf{q}_1 and \mathbf{q}_2 . In all panels the full line is the sum of β_1 and β_2 and the dashed line is $\beta_3 + \beta_4$. Panel (a), (b) and (c) depict the amplitudes at the conditions marked by a, b and c in Fig. 4.4 respectively.

where $\phi_0 = \arccos(-1/3)$.

We calculate the thermodynamic potential in Eq. (4.13) along the line of second-order phase transitions from the normal gas to the inhomogeneous superfluid phase. The result is shown in Fig. 4.7 and it can be seen that at the Lifshitz point the LO phase gives the lowest energy and is thus the most favorable lattice configuration, whereas for larger majorities of ^{40}K atoms it becomes more favorable to break translational symmetry in three spatial directions. Namely, then the LO^3 configuration gives the lowest thermodynamic potential.

In order to better understand this result, we now look at the dependence of the amplitudes of the Feynman diagrams in Fig. 4.6 on the angle θ between \mathbf{q}_1 and \mathbf{q}_2 . The angular dependencies are shown in Fig. 4.8, for three points along the line of phase transitions. The amplitudes in Fig. 4.8(a) are calculated at the conditions marked by a in Fig. 4.4, close to the Lifshitz point. Panel (b) corresponds to lower temperatures, just below the transition to the LO^3 phase. It can be seen that energy is now gained by having $\pi/2$ angles in the Cooper-

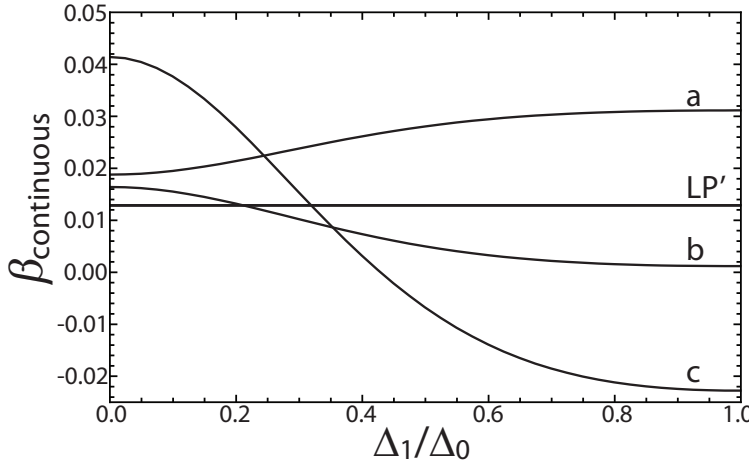


Figure 4.9: The continuous ansatz as a function of the perpendicular amplitude Δ_1 divided by the LO amplitude Δ_0 for different points along the line of continuous phase transitions. The letters a, b and c correspond to the conditions marked in Fig. 4.4. The horizontal line corresponds to the point LP' in Fig. 4.4 where the LO and LO^3 phase meet.

pair wavefunction. This explains why it is now favorable to break translational symmetry in all directions, instead of in only one direction as in the LO phase. For lower temperatures, as in panel (c), this energy gain is even larger. These plots also clarify why more complicated Cooper-pair wavefunctions, such as the triangular configuration, never form the ground state of the system. Namely, these configurations include different angles than the angles for which the amplitudes of the fourth-order diagrams are minimal.

4.3.1 Continuous transition from LO to LO^3

A possibility we did not consider so far is a transition from the LO to the LO^3 phase, where the two standing waves perpendicular to the LO standing wave have an amplitude that continuously changes from zero for higher temperatures to a nonzero value for temperatures below LP' . The Cooper-pair ansatz describing this

possibility has the following form

$$\Delta(\mathbf{x}) = \frac{1}{\sqrt{2 + 4p^2}} [\Delta_0(e^{iq_x x} + e^{-iq_x x}) + \Delta_1(e^{iq_y y} + e^{-iq_y y} + e^{iq_z z} + e^{-iq_z z})], \quad (4.25)$$

where $p = \Delta_1/\Delta_0$ and the perpendicular amplitude Δ_1 can now change continuously from zero to some nonzero value. Also for this ansatz the quadratic coefficient $\alpha(q)$ in Eq. (4.13) has the same form and the fourth-order coefficient reads

$$\begin{aligned} \beta_{\text{continuous}}(q) = & \frac{1}{(2 + 4p^2)^2} \left[(2 + 4a^2)\beta_{1+2}(q, 0) + (4 + 8p^2)\beta_{1+2}(q, \pi) \right. \\ & \left. + (32p^2 + 16p^4)\beta_{1+2}(q, \frac{\pi}{2}) + (16p^2 + 8p^4)\beta_{3+4}(q, \frac{\pi}{2}) \right], \end{aligned} \quad (4.26)$$

which reduces to β_{LO} for $p = 0$, when $\Delta_1 = 0$, and to β_{LO^3} for $p = 1$, when $\Delta_1 = \Delta_0$. In Fig. 4.9 we plot the above coefficient as a function of the perpendicular amplitude for different points along the line of continuous phase transitions from the normal to the inhomogeneous superfluid state. The minimum of this coefficient determines the inhomogeneous superfluid that is the equilibrium state. For point a in Fig. 4.4 the minimum is located at $\Delta_1 = 0$, see Fig. 4.9, which means that the equilibrium state of the Fermi mixture for these conditions is the LO state. While, for points b and c the LO^3 phase occurs and at the transition point LP' the energy of the two phases is equal. We conclude that between the regions where respectively the LO and LO^3 phase occur there is not a region where translational symmetry is already broken in three spatial directions but with a smaller amplitude in the directions perpendicular to the LO direction.

4.4 LO Green's function

We found that for one point (LP') on the normal to superfluid transition line the thermodynamic potentials for the LO and the LO^3 phase are equal, see Figs. 4.4 and 4.7. On the high-temperature side of LP' the transition from the normal gas is to an inhomogeneous superfluid with one broken spatial symmetry, while for lower temperatures it is to a phase with three broken spatial symmetries. Within the superfluid region the transition line between these two different inhomogeneous phases can be obtained by again comparing thermodynamic potentials, but now that we know which phases to compare we can also calculate the transition line more directly. In order to do so, we split the order parameter for the LO^3 phase as

$$\Delta_{\text{LO}^3}(\mathbf{x}) = \Delta_{\text{LO}}(z) + \Delta_{\perp}[\cos(qx) + \cos(qy)], \quad (4.27)$$

where $\Delta_{\text{LO}}(z)$ is given in Eq. (4.9). We now expand the thermodynamic potential for the cubic phase in the perpendicular order parameter Δ_{\perp}

$$\Omega_{\text{LO}^3} \simeq \Omega_{\text{LO}}(\Delta_0, q) + \alpha_{\perp}(\Delta_0, q)|\Delta_{\perp}|^2. \quad (4.28)$$

At the moment α_{\perp} changes sign the minimum of Ω_{LO^3} shifts to a nonzero value of Δ_{\perp} , which means that the LO^3 phase is more favorable than the LO phase. In order to calculate α_{\perp} we need to determine the Green's function for the LO phase, since

$$\alpha_{\perp} = -\frac{V}{V_0} + \frac{k_B T}{2|\Delta_{\perp}|^2} \text{Tr} [\mathbf{G}_{\text{LO}} \mathbf{\Delta}_{\perp} \mathbf{G}_{\text{LO}} \mathbf{\Delta}_{\perp}], \quad (4.29)$$

where $\mathbf{\Delta}_{\perp}(x, y) = (\Delta_{\perp}[\cos(qx) + \cos(qy)]/\hbar)\sigma_x$, with σ_x the first Pauli matrix in Nambu space. The trace in the above equation is taken over real space, imaginary time and Nambu space. The inverse Green's function $\mathbf{G}_{\text{LO}}^{-1}$ is known from Eq. (4.1) and can be expanded in its energy eigenmodes, which are the Bogoliubov quasiparticle wavefunctions. In this manner we obtain an expression for the Green's function in the LO phase, which contains the inhomogeneities of this phase in an exact way. The quasiparticle wavefunctions for the Larkin-Ovchinnikov phase we calculate by solving the Bogoliubov-de Gennes equation

$$\begin{pmatrix} -\frac{\hbar^2 \nabla^2}{2m_{\uparrow}} - \mu_{\uparrow} & \Delta_{\text{LO}}(z) \\ \Delta_{\text{LO}}(z) & \frac{\hbar^2 \nabla^2}{2m_{\downarrow}} + \mu_{\downarrow} \end{pmatrix} \begin{pmatrix} u_n(\mathbf{x}) \\ v_n(\mathbf{x}) \end{pmatrix} = \hbar\omega_n \begin{pmatrix} u_n(\mathbf{x}) \\ v_n(\mathbf{x}) \end{pmatrix}, \quad (4.30)$$

where u and v are the quasiparticle coherence factors and n is the band index labeling the energy eigenmode. The inverse Green's function, on the left-hand side of the equation, contains the Larkin-Ovchinnikov order parameter. Since this pairing field has a periodicity the quasiparticle wavefunctions are according to Bloch's theorem of the form

$$\begin{pmatrix} u_n(\mathbf{x}) \\ v_n(\mathbf{x}) \end{pmatrix} = \begin{pmatrix} u_{\mathbf{k}, n}(z) \\ v_{\mathbf{k}, n}(z) \end{pmatrix} e^{i\mathbf{k} \cdot \mathbf{x}}, \quad (4.31)$$

where $u_{\mathbf{k}, n}(z)$ and $v_{\mathbf{k}, n}(z)$ are periodic functions with the same periodicity as the gap $\Delta_{\text{LO}}(z)$ and are thus only periodic in the z -direction, which is reflected also in the single band index n .

In order to determine the transition line between the LO and LO^3 phase we first obtain the equilibrium state of the thermodynamic potential for the LO phase and this we use as input to calculate α_{\perp} . The line where α_{\perp} is zero is the transition line between the two inhomogeneous superfluid phases, see Figs. 2(a) and 4.4.

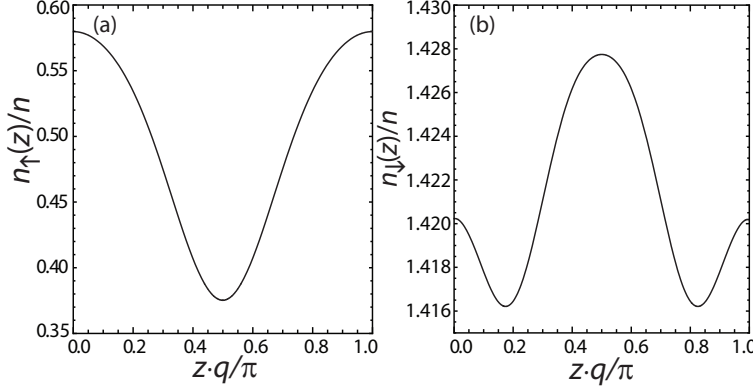


Figure 4.10: Densities for the ${}^6\text{Li}$ atoms (a) and the ${}^{40}\text{K}$ atoms (b) scaled by the total average density $n = [n_{\uparrow}(0) + n_{\downarrow}(0)]/2$ in the LO phase as a function of position for the point denoted with a cross in Fig. 2(a).

4.5 Inhomogeneous densities

From solving the Bogoliubov-de Gennes equation in Eq. (4.30) we know the quasiparticle coherence factors u and v for the LO phase. With these wavefunctions it is possible to calculate the particle densities for the ${}^6\text{Li}$ and the ${}^{40}\text{K}$ atoms as a function of position. Namely, the densities are given by

$$n_{\sigma}(z) = \sum_{\mathbf{k}, n} \{ u_{\mathbf{k}, n}^2(z) N_{\sigma}(\hbar\omega_{\mathbf{k}, n}) + v_{\mathbf{k}, n}^2(z) [1 - N_{-\sigma}(\hbar\omega_{\mathbf{k}, n})] \}. \quad (4.32)$$

We take the vector \mathbf{k} to lie in the first Brioullin zone in momentum space, which is here infinitely large in the x and y direction and has size $2q$ in the z direction. In Fig. 4.10 the inhomogeneous densities in the LO phase are shown for the point denoted with a cross in the phase diagram of Fig. 2(a) and it can be seen that the density of the minority atoms follows the form of the Cooper-pair ansatz. In contrast, the density of the ${}^{40}\text{K}$ atoms has its maximum at the position where the Cooper pair has a minimum. In this way the system relaxes the frustration caused by the population imbalance, instead of phase separating, which occurs for a majority of ${}^6\text{Li}$ atoms [15, 16]. We find that the modulation in the density of the ${}^6\text{Li}$ atoms is about 10%, as can be seen in Fig. 4.10(a), whereas the modulation for the majority atoms is much smaller. The density modulations can be visible in an experiment, for example using Bragg spectroscopy. A homogeneous superfluid

does not show Bragg peaks and thus the appearance of any Bragg peak is a sign of inhomogeneities in the superfluid phase.

4.6 Discussion and Conclusion

For the mixture of resonantly interacting ^6Li and ^{40}K atoms we completed the phase diagram, which contains inhomogeneous superfluid phases. These superfluid phases have a crystalline order, just as a solid, and are thus special kinds of supersolids. Usually a supersolid is defined as a phase with both long-range diagonal and off-diagonal order in the one-particle density matrix. The LO and LO³ only have diagonal order in the one-particle density matrix but there is both long-range diagonal and off-diagonal order in the two-particle density matrix. This means that the inhomogeneous superfluid is a supersolid phase, but not in the usual sense.

The results presented in this paper were calculated making use of two approximations. The first one is the mean-field approximation, which is known to give good qualitative results. Although our results are only reasonable estimates quantitatively, we are confident that, as in the mass-balanced case, the phase diagram does not change qualitatively if screening and selfenergy effects are included. However, fluctuations can have a large effect on the density modulations. In order to observe a spatial periodicity in the densities true long-range order is most desirable. But due to fluctuation effects only algebraic long-range order will exist in the LO phase [98, 112], making it more difficult to observe the periodicity.

The second approximation we make is that we take into account only a single magnitude of the lattice wavevector q . For the continuous transition from the normal gas to the superfluid state this is exact, whereas it is an approximation inside the superfluid phase. Deep in the superfluid phase the pairing field is expected to take a more complicated form and to depend on a range of wave vectors [81]. If in the phase diagram the chemical-potential difference is on the x -axis all transitions take place close to the normal to superfluid transition as shown in Fig. 4.4. Therefore, it is not expected that taking into account a more complicated form for the gap will change the phase diagram qualitatively. Moreover, our calculation is variational and thus gives a conservative estimate of the supersolid region of the phase diagram.

In this paper we presented results for a homogeneous system and we did not consider a confining trap. To take into account the trap for the atoms, a local-density approximation can be made. The trap felt by the atoms depends on the species of the atoms, which means that for two atom species two different traps

have to be taken into account [35]. The trap can have an advantageous influence. Namely, if the periodicity of the Cooper pair wavefunction is pinned by the shape of the trap it becomes easier to observe density modulations.

Nederlandse samenvatting

Als de dichtheid van een stof niet afhangt van de plaats, maar overal gelijk aan een constante is, dan is die stof homogeen. Vloeistoffen zijn homogeen. Na een faseovergang naar een vaste stof is de dichtheid niet meer overal gelijk. Deeltjes zitten dan namelijk geordend in een kristalstructuur en de dichtheid is nu een functie van positie.

In ons onderzoek bekijken we een bijzondere vloeistof, namelijk een supervloeistof. Wij voorspellen dat er gevallen zijn waarin de dichtheid in deze supervloeistof van de plaats afhangt en de supervloeistof dus niet homogeen, maar inhomogeen is.

Ultrakoud

Een ijl gas van atomen kan gevangen worden in een magneetveld en vervolgens met lasers afgekoeld worden. De fotonen afkomstig van de lasers hebben een impulsmoment en dragen dit bij een botsing over aan het atoom. Als een foton en een atoom in tegengestelde richting bewegen, wordt het atoom door de botsing een klein beetje afgeremd. Door met heel veel fotonen van verschillende kanten tegen het gas van atomen te botsen, worden de atomen bijna tot stilstand afgeremd en hierdoor koelt het gas af. Met laserkoeling kan een gas afgekoeld worden tot de micro-Kelvin schaal. Dit is geen koud, maar een ultrakoud gas.

Bij deze temperaturen kan het gas nog verder afgekoeld worden door de magnetische val minder diep te maken. De atomen met de meeste energie, de heetste atomen, ontsnappen dan uit de val en de rest van het gas koelt daardoor verder af. Dit koelingsmechanisme heet verdampingskoelen en heeft veel weg van het afkoelen van een kop koffie door erop te blazen. De heetste koffiemoleculen blaas je weg, waardoor de rest van de koffie afkoelt. Met verdampingskoelen kunnen temperaturen in het nanokelvin-regime bereikt worden.

In dit regime kan er een faseovergang plaatsvinden van een klassiek gas naar een quantummechanische fase, een zogenaamde supervloeistof. Dit is een fase waarin alle atomen zich in dezelfde quantummechanische toestand bevinden en wrijving tussen de atomen volledig afwezig is.

Supervloeistof

Als de atomen bosonisch zijn, oftewel als de spin van de atomen een geheel getal is, dan kunnen meerdere atomen dezelfde quantumtoestand aannemen. Het is zelfs zo dat als een aantal bosonen al een bepaalde quantumtoestand heeft, dat het waarschijnlijk is dat er meer bosonen die toestand aannemen. Dit quantummechanische effect heet Bose-versterking.

Bij het afkoelen van een Bose-gas gaan steeds meer atomen in de grondtoestand zitten. Als een eindige fractie van de atomen in de grondtoestand is, ontstaat er een supervloeistof. Die atomen in de grondtoestand vormen een Bose-Einstein condensaat.

Als de atomen fermionisch zijn, oftewel als de atomen een halftallige spin hebben, dan kan er slechts één atoom een bepaalde quantumtoestand aannemen. Dit effect heet Fermi-blokering. Fermionen kunnen niet, zoals de bosonen, allemaal dezelfde toestand aannemen. Hierdoor kan er in een Fermi-gas niet zomaar een faseovergang naar een supervloeistof plaatsvinden. Echter, als er een aantrekkende kracht is tussen de fermionen, hoe klein ook, dan kunnen twee fermionen een zogenaamd Cooper-paar vormen. Cooper-paren zijn een soort bosonen en kunnen wel allemaal dezelfde quantumtoestand aannemen en een supervloeistof vormen.

Een gevolg van de Fermi-blokering is dat een golffunctie die twee identieke fermionen beschrijft oneven is, wat betekent dat deze een minteken krijgt onder verwisseling van de deeltjes. Deze golffunctie is een product van een baandeel, dat de beweging van de twee fermionen beschrijft, en een spintoestand, waarvan één van de twee oneven moet zijn. Als dit het baandeel is, hebben de twee fermionen verschillende impuls. Een botsing kan dan alleen plaatsvinden als de twee fermionen genoeg energie hebben om de centrifugale barrière over te komen die door het verschil in impuls ontstaat. Door deze barrière vinden er bij lage temperatuur vrijwel geen interacties plaats tussen fermionen met een oneven baandeel en een Cooper-paar van identieke deeltjes bestaat daardoor uit twee fermionen met dezelfde impuls, maar verschillende spintoestanden.

Supergeleiding

Toen Kamerlingh Onnes voor het eerst supergeleiding waarnam in 1911, nam hij ook als eerste, zonder dat hij het wist, een supervloeistof van Cooper-paren waar. Hij had namelijk een supervloeistof van elektronen gecreëerd. Elektronen hebben halftallige spin en zijn dus fermionen. Bij zeer lage temperatuur vormen twee elektronen een Cooper-paar en ontstaat er een supervloeistof van elektronen. De supervloeistof kan wrijvingloos bewegen en dit is wat Kamerlingh Onnes heeft gemeten: bij een bepaalde temperatuur, de kritische temperatuur genoemd, verdwijnt de weerstand van een metaal volledig. Er kan in dat geval veel stroom door het metaal gestuurd worden, zonder dat het metaal opwarmt, vandaar de naam supergeleider.

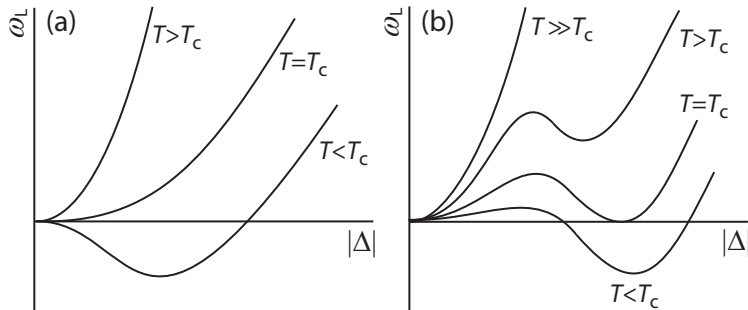
De supergeleider kent al menige toepassing. Doordat supergeleiders grote stromen kunnen vervoeren, kunnen er grote magneetvelden mee opgewekt worden. Dit wordt bijvoorbeeld gebruikt in de MRI-scanner. In de scanner bevinden zich grote spoelen die met vloeibaar helium worden afgekoeld tot beneden de kritische temperatuur, zodat de spoelen supergeleidend worden. De grote magneetvelden die deze spoelen dan opwekken, worden gebruikt om een scan te maken.

Als er een materiaal zou bestaan dat supergeleidend is bij kamertemperatuur zou het wereldenergieprobleem voor een groot deel opgelost zijn, doordat er dan bij energietransport veel minder energie verloren zou gaan. Het begrijpen van de overgang van losse fermionen naar een supervloeistof van Cooper-paren kan helpen bij de ontwikkeling van een dergelijk materiaal. Het is echter lastig om dit fenomeen te bestuderen in een metaal, omdat de elektronen daar door een roosterstructuur bewegen. Atomen zijn goed te manipuleren in een experiment en bieden een uitstekende mogelijkheid om de supervloeistof te bestuderen.

Ultrakoude atomen: ^6Li en ^{40}K

In een experiment met een ultrakoud gas van fermionen, ofwel een Fermi-gas, kunnen veel aspecten van de faseovergang naar een supervloeistof onderzocht worden. Belangrijk is dat het effect van de interacties tussen de atomen op een faseovergang onderzocht kan worden. De interactie tussen atomen kan in een experiment namelijk gecontroleerd worden met een extern magneetveld. Bij een sterke aantrekkende interactie vormen de atomen eerder Cooper-paren en daardoor is de kritische temperatuur relatief hoog, terwijl bij zwakke interacties de kritische temperatuur heel laag is.

Sinds een aantal jaren lukt het experimentatoren ook om verschillende soorten atomen in dezelfde val te vangen. Dit is een belangrijke stap richting een super-



Figuur 1: De thermodynamische potentiaal als functie van Cooper-paar aantallen bij verschillende temperaturen. Een minimum bij nul betekent geen Cooper-paren en geen supervloeistof, een minimum bij een eindig aantal Cooper-paren betekent dat er een faseovergang naar een supervloeistof heeft plaatsgevonden. In figuur (a) verschuift het minimum op een continue manier weg uit het nulpunt, terwijl er in figuur (b) een sprong is. In het geval van figuur (b) treedt er faseseparatie op.

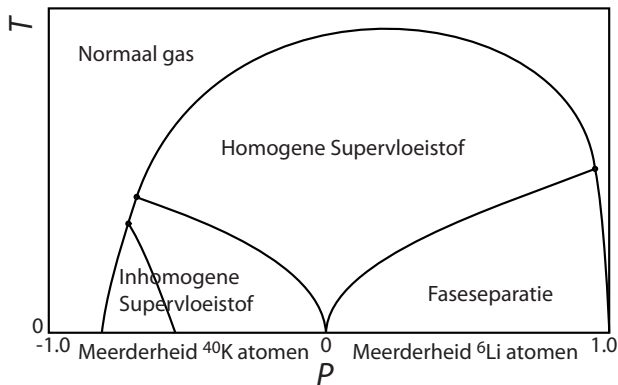
vloeistof van niet-identieke fermionen. In ons onderzoek rekenen we de kritische temperaturen uit in een mengsel van ${}^6\text{Li}$ atomen en ${}^{40}\text{K}$ atomen. Dit mengsel is al wel eens gevangen in een magnetische val, maar nog niet genoeg afgekoeld om een supervloeistof te zien.

In de experimenten met dit mengsel hebben alle ${}^6\text{Li}$ atomen dezelfde spintoestand, waardoor bij lage temperatuur er geen interacties tussen de ${}^6\text{Li}$ atomen zijn. Hetzelfde geldt voor de ${}^{40}\text{K}$ atomen. Er kunnen wel interacties plaatsvinden tussen de ${}^6\text{Li}$ en ${}^{40}\text{K}$ atomen, dat zijn immers geen identieke fermionen en de Fermi-blokering treedt niet op. Een ${}^6\text{Li}$ atoom en ${}^{40}\text{K}$ atoom kunnen samen dus een Cooper-paar vormen. Door het grote massaverschil tussen de atomen, ${}^{40}\text{K}$ is ongeveer zeven keer zo zwaar als ${}^6\text{Li}$, is dit echter minder gemakkelijk dan bij gelijke massa's.

Juist dit massaverschil maakt dit een interessant systeem om te bestuderen. Fermionen met verschillende massa's komen namelijk ook in de natuur voor, zoals bijvoorbeeld in de kern van een neutronenster, die uit quarks bestaat. Door het mengsel van ${}^6\text{Li}$ en ${}^{40}\text{K}$ atomen te bestuderen, kunnen we ook meer over neutronsterren leren.

Het fasediagram

We hebben voor het mengsel van ${}^6\text{Li}$ en ${}^{40}\text{K}$ het complete fasediagram uitgerekend. Dat wil zeggen dat we voor alle polarisaties de kritische temperatuur berekend



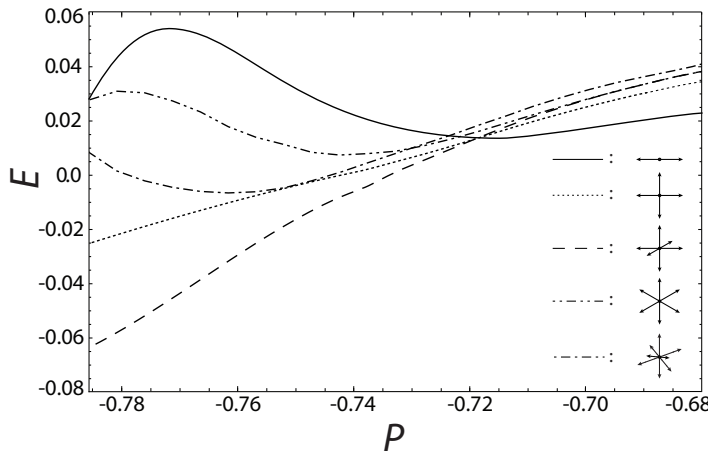
Figuur 2: Het fasediagram van het 6Li-40K mengsel. Voor een meerderheid van 6Li atomen treedt er faseseparatie op, terwijl er een continue overgang naar een inhomogeen supervloeistof plaatsvindt voor een meerderheid van 40K atomen. Er treden twee verschillende inhomogene fasen op.

hebben. De polarisatie P is het verschil in deeltjesaantallen gedeeld door het totale aantal deeltjes,

$$P = \frac{n_{\text{Li}} - n_{\text{K}}}{n_{\text{Li}} + n_{\text{K}}}.$$
 (A)

Bovendien hebben we bestudeerd wat voor supervloeistof de Cooper-paren in dit mengsel vormen en of er door het massaverschil ook meer exotische quantumfases ontstaan.

Om het fasediagram uit te rekenen, bepalen we de thermodynamische potentiaal van dit mengsel van fermionen. Deze hangt af van de thermodynamische parameters van het systeem, zoals de temperatuur en de polarisatie. Bovendien is de thermodynamische potentiaal een functie van het aantal Cooperparen , zie figuur 1, waarbij de evenwichtstoestand van het systeem het minimum is. Als het minimum van de potentiaal bij nul Cooper-paren ligt, is er geen supervloeistof, terwijl er een faseovergang heeft plaatsgevonden als dit minimum niet bij nul ligt. Het minimum kan op een continue of discontinue manier wegschuiven van nul. In het laatste geval treedt er een scheiding tussen twee fasen (faseseparatie) op. Als er evenveel ${}^6\text{Li}$ als ${}^{40}\text{K}$ atomen in de magnetische val zijn, $P = 0$, dan kan elk atoom deel uitmaken van een Cooper-paar, zie figuur 2. De dichtheid van de supervloeistof is hier onafhankelijk van de plaats. De overgang naar deze



Figuur 3: De energie E van het 6Li-40K-mengsel langs de lijn van faseovergangen. Bij de grootste polarisatie waar een inhomogene supervloeistof optreedt, is een dichtheidsconfiguratie met een periodiciteit in één richting het gunstigst (doorgetrokken lijn). Voor kleinere polarisaties is het gunstiger om in drie richtingen een periodiciteit te hebben (gestreepte lijn). Andere roosterconfiguraties geven nooit de laagste energie (gestippelde en gestreept-gestippelde lijnen).

homogene supervloeistof is continu. Als de polarisatie klein is, kunnen er nog steeds Cooper-paren gevormd worden, maar blijven er wel atomen over.

Voor een grote meerderheid van ^6Li atomen is er een discontinue faseovergang naar een homogene supervloeistof. In het experiment zal op dat moment faseseparatie optreden. In het diepste gedeelte van de val bestaat een homogene supervloeistof met evenveel ^6Li als ^{40}K atomen, terwijl er zich aan de rand van de val een gas van ^6Li atomen bevindt. Faseseparatie is niet ongewoon bij faseovergangen, het treedt bijvoorbeeld ook op bij het koken van water.

Inhomogene supervloeistoffen

Het interessantste gebied in het fasediagram is bij een meerderheid van ^{40}K atomen. We vinden dan een continue faseovergang naar een inhomogene supervloeistof. In deze exotische fase hangt de dichtheid van Cooper-paren van de positie af. De dichtheid kan echter op vele manieren plaatsafhankelijk zijn en elke dichtheidsconfiguratie levert een andere thermodynamische potentiaal op. Deze hebben wij voor allerlei configuraties uitgerekend en vervolgens hebben we het minimum

bepaald, wat de energie van de supervloeistof geeft. De dichtheidsconfiguratie die in werkelijkheid op zal treden, is die met de laagste energie, zie figuur 3.

Wij hebben gevonden dat het mengsel van ^6Li en ^{40}K twee verschillende dichtheidsconfiguraties kan vertonen. Allereerst treedt er een faseovergang op naar een inhomogene supervloeistof waarbij in twee ruimtelijke richtingen de dichtheid constant is, terwijl de dichtheid in de derde richting een staande golf is. De periodiciteit en de amplitude van de dichtheidsgolf hangen van de temperatuur en de polarisatie af. In dit geval is de supervloeistof homogeen in twee richtingen.

Voor kleinere polarisaties en lagere temperaturen is de supervloeistof inhomogeen in alle ruimtelijke richtingen en de dichtheid is een staande golf in alle drie de richtingen. De amplitudes en de periodiciteit van de dichtheid zijn in de drie richtingen gelijk. Deze fase heeft ook eigenschappen van een vaste stof, namelijk positie-afhankelijke dichtheseden, maar het is geen vaste stof! Het is een inhomogene supervloeistof!

Dergelijke exotische fasen, een supervloeistof met een dichtheid die in drie richtingen een periodiciteit heeft, zijn nog nooit in een experiment waargenomen. Er is wel een fase met vergelijkbare eigenschappen in een één-dimensionale val waargenomen, maar de dichtheidsvariaties zijn daar alleen indirect waargenomen. Het zou een grote doorbraak betekenen als de fasen die wij voorspellen worden waargenomen!

Bibliography

- [1] H. Kamerlingh Onnes. Akad. van Wetenschappen **14**, 818 (1911).
- [2] J. Bardeen, L. Cooper and J. Schrieffer. Phys. Rev. **108**, 1175 (1957).
- [3] M. W. Zwierlein, A. Schirotzek, C. H. Schunck and W. Ketterle. Science **311**, 492 (2006).
- [4] G. B. Partridge, W. Li, Y. A. Liao, R. G. Hulet, M. Haque and H. T. C. Stoof. Phys. Rev. Lett. **97**, 190407 (2006).
- [5] E. Wille, F. M. Spiegelhalder, G. Kerner, D. Naik, A. Trenkwalder, G. Hendl, F. Schreck, R. Grimm, T. G. Tiecke, J. T. M. Walraven, S. J. J. M. F. Kokkelmans, E. Tiesinga and P. S. Julienne. Phys. Rev. Lett. **100**, 053201 (2008).
- [6] A.-C. Voigt, M. Taglieber, L. Costa, T. Aoki, W. Wieser, T. W. Hänsch and K. Dieckmann. Phys. Rev. Lett. **102**, 020405 (2009).
- [7] M. H. Anderson, J. R. Ensher, M. R. Matthews, C. E. Wieman and E. A. Cornell. Science **269**, 198 (1995).
- [8] C. C. Bradley, C. A. Sackett, J. J. Tollett and R. G. Hulet. Phys. Rev. Lett. **75**, 1687 (1995).
- [9] K. B. Davis, M. O. Mewes, M. R. Andrews, N. J. Van Druten, D. S. Durfee, D. M. Kurn and W. Ketterle. Phys. Rev. Lett. **75**, 3969 (1995).
- [10] A. Einstein. Sitz. Ber. Preuss. Akad. Wiss. (Berlin) **22** (1924).
- [11] J. Prodan, A. Migdall, W. D. Phillips, I. So, H. Metcalf and J. Dalibard. Phys. Rev. Lett. **54**, 992 (1985).
- [12] P. Kapitza. Nature **141**, 74 (1938).
- [13] J. F. Allen and A. D. Misener. Nature **141**, 75 (1938).
- [14] F. London. Nature **141**, 643 (1938).

- [15] A. L. Migdall, W. D. Phillips, J. V. Prodan, T. H. Bergeman and H. J. Metcalf. Phys. Rev. Lett. **54**, 2596 (1985).
- [16] N. Masuhara, J. M. Doyle, J. C. Sandberg, D. Kleppner, T. J. Greytak, H. F. Hess and G. P. Kochanski. Phys. Rev. Lett. **61**, 935 (1988).
- [17] J. Kasprzak, M. Richard, S. Kundermann, A. Baas, P. Jeambrun, J. M. J. Keeling, F. M. Marchetti, M. H. Szymanska, R. Andre, J. L. Staehli, V. Savona, P. B. Littlewood, B. Deveaud and L. S. Dang. Nature **443**, 409 (2006).
- [18] S. O. Demokritov, V. E. Demidov, O. Dzyapko, G. A. Melkov, A. A. Serga, B. Hillebrands and A. N. Slavin. Nature **443**, 430 (2006).
- [19] J. Klaers, J. Schmitt, F. Vewinger and M. Weitz. Nature **468**, 545 (2010).
- [20] P. S. Jessen, C. Gerz, P. D. Lett, W. D. Phillips, S. L. Rolston, R. J. C. Spreeuw and C. I. Westbrook. Phys. Rev. Lett. **69**, 49 (1992).
- [21] M. P. A. Fisher, P. B. Weichman, G. Grinstein and D. S. Fisher. Phys. Rev. B **40**, 546 (1989).
- [22] M. Greiner, O. Mandel, T. Esslinger, T. W. Hänsch and I. Bloch. Nature **415**, 39 (2002).
- [23] B. DeMarco and D. S. Jin. Science **285**, 1703 (1999).
- [24] E. Tiesinga, B. J. Verhaar and H. T. C. Stoof. Phys. Rev. A **47**, 4114 (1993).
- [25] H. Feshbach. Ann. Phys. **5**, 357.
- [26] W. C. Stwalley. Phys. Rev. Lett. **37**, 1628 (1976).
- [27] C. A. Regal, M. Greiner and D. S. Jin. Phys. Rev. Lett. **92**, 040403 (2004).
- [28] G. B. Partridge, K. E. Strecker, R. I. Kamar, M. W. Jack and R. G. Hulet. Phys. Rev. Lett. **95**, 020404 (2005).
- [29] M. W. Zwierlein, C. A. Stan, C. H. Schunck, S. M. Raupach, A. J. Kerman and W. Ketterle. Phys. Rev. Lett. **92**, 120403 (2004).
- [30] J. Kinast, S. L. Hemmer, M. E. Gehm, A. Turlapov and J. E. Thomas. Phys. Rev. Lett. **92**, 150402 (2004).
- [31] M. Bartenstein, A. Altmeyer, S. Riedl, S. Jochim, C. Chin and R. Denschlag, J. H. and Grimm. Phys. Rev. Lett. **92**, 203201 (2004).
- [32] T. Bourdel, L. Khaykovich, J. Cubizolles, J. Zhang, F. Chevy, M. Teichmann, L. Tarruell, S. J. Kokkelmans and C. Salomon. Phys. Rev. Lett. **93**, 050401 (2004).
- [33] L. Costa, J. Brachmann, A.-C. Voigt, C. Hahn, M. Taglieber, T. W. Hänsch and K. Dieckmann. Phys. Rev. Lett. **105**, 123201 (2010).
- [34] T. G. Tiecke, M. R. Goosen, A. Ludewig, S. D. Gensemer, S. Kraft, S. J.

- J. M. F. Kokkelmans and J. T. M. Walraven. Phys. Rev. Lett. **104**, 053202 (2010).
- [35] A. Trenkwalder, C. Kohstall, M. Zaccanti, D. Naik, A. I. Sidorov, F. Schreck and R. Grimm. Phys. Rev. Lett. **106**, 115304 (2011).
- [36] A. Ridinger, S. Chaudhuri, T. Salez, U. Eismann, D. Fernandes, K. Magalhes, D. Wilkowski, C. Salomon and F. Chevy. EPJ D **65**, 223 (2011).
- [37] C. Kohstall, M. Zaccanti, M. Jag, A. Trenkwalder, P. Massignan, G. M. Bruun, F. Schreck and R. Grimm. Nature **485**, 615 (2012).
- [38] J. Bednorz and K. Müller. Zeitschrift fr Physik B **64**, 189 (1986). ISSN 0722-3277.
- [39] R. Casalbuoni and G. Nardulli. Rev. Mod. Phys. **76**, 263 (2004).
- [40] Y.-J. Lin, R. L. Compton, K. Jimenez-Garcia, J. V. Porto and I. B. Spielman. Nature **462** (2009).
- [41] D. L. Campbell, G. Juzeliūnas and I. B. Spielman. Phys. Rev. A **84**, 025602 (2011).
- [42] Y. Shin, C. Schunck, A. Schirotzek and W. Ketterle. Nature **451**, 689 (2008).
- [43] L. Gor'kov and T. Melik-Barkhudarov. Sov. Phys. JETP **13**, 1018 (1961).
- [44] H. Heiselberg, C. J. Pethick, H. Smith and L. Viverit. Phys. Rev. Lett. **85**, 2418 (2000).
- [45] C. Lobo, A. Recati, S. Giorgini and S. Stringari. Phys. Rev. Lett. **97**, 200403 (2006).
- [46] E. Burovski, N. Prokof'ev, B. Svistunov and M. Troyer. Phys. Rev. Lett. **96**, 160402 (2006).
- [47] K. B. Gubbels and H. T. C. Stoof. Phys. Rev. Lett. **100**, 140407 (2008).
- [48] K. B. Gubbels, M. W. J. Romans and H. T. C. Stoof. Phys. Rev. Lett. **97**, 210402 (2006).
- [49] A. Sommer, M. Ku, G. Roati and M. Zwierlein. Nature **472**, 201 (2011).
- [50] S. Koller, A. Groot, P. Bons, R. Duine, H. Stoof and P. van der Straten. arXiv:1204.6143 .
- [51] R. A. Duine, M. Polini, A. Raoux, H. T. C. Stoof and G. Vignale. New Journal of Physics **13**, 045010 (2011).
- [52] A. J. Leggett. Rev. Mod. Phys. **73**, 307 (2001).
- [53] E. Kim and M. H. W. Chan. Nature **427**, 225 (2004).
- [54] E. Kim and M. H. W. Chan. Science **305**, 1941 (2004).
- [55] T. Leggett. Science **305**, 1921 (2004).

- [56] N. Prokof'ev and B. Svistunov. Phys. Rev. Lett. **94**, 155302 (2005).
- [57] L. Pitaevskii. *Superconductivity: Conventional and Unconventional Superconductors*, chapter Phenomenology and Microscopic Theory: Theoretical Foundations. Springer (2008).
- [58] L. Landau. Phys. Z. Sowjetunion **3**, 664 (1933).
- [59] N. Mannella, W. Yang, X. J. Zhou, H. Zheng, J. F. Mitchell, J. Zaanen, T. P. Devereaux, N. Nagaosa, Z. Hussain and Z.-X. Shen. nature **438**, 474 (2005).
- [60] P. Nozières and A. Blandin. J. Phys. (France) **41**, 193 (1980).
- [61] A. Schirotzek, C.-H. Wu, A. Sommer and M. W. Zwierlein. Phys. Rev. Lett. **102**, 230402 (2009).
- [62] S. Nascimbène, N. Navon, K. J. Jiang, L. Tarruell, M. Teichmann, J. McKeever, F. Chevy and C. Salomon. Phys. Rev. Lett. **103**, 170402 (2009).
- [63] A. Sommer, M. Ku and M. Zwierlein. New J. Phys. **13**, 055009 (2011).
- [64] F. Chevy. Phys. Rev. Lett. **96**, 130401 (2006).
- [65] N. Prokof'ev and B. Svistunov. Phys. Rev. B **77**, 020408 (2008).
- [66] R. Combescot, A. Recati, C. Lobo and F. Chevy. Phys. Rev. Lett. **98**, 180402 (2007).
- [67] P. Massignan, G. M. Bruun and H. T. C. Stoof. Phys. Rev. A **78**, 031602 (2008).
- [68] R. Combescot and S. Giraud. Phys. Rev. Lett. **101**, 050404 (2008).
- [69] M. Punk, P. T. Dumitrescu and W. Zwerger. Phys. Rev. A **80**, 053605 (2009).
- [70] P. Massignan and G. Bruun. The European Physical Journal D **65**, 83 (2011).
- [71] K. B. Gubbels, J. E. Baarsma and H. T. C. Stoof. Phys. Rev. Lett. **103**, 195301 (2009).
- [72] J. E. Baarsma, K. B. Gubbels and H. T. C. Stoof. Phys. Rev. A **82**, 013624 (2010).
- [73] G. M. Bruun, A. Recati, C. J. Pethick, H. Smith and S. Stringari. Phys. Rev. Lett. **100**, 240406 (2008).
- [74] A. Gezerlis, S. Gandolfi, K. E. Schmidt and J. Carlson. Phys. Rev. Lett. **103**, 060403 (2009).
- [75] G. M. Bruun and G. Baym. Phys. Rev. A **74**, 033623 (2006).
- [76] G. B. Partridge, W. Li, R. I. Kamar, Y.-a. Liao and R. G. Hulet. Science **311**, 503 (2006).

- [77] J. Diederix, K. Gubbels and H. Stoof. arXiv:0907.0127v2 (2009).
- [78] D. Bailin and A. Love. Phys. Rep. **107**, 325 (1984).
- [79] A. I. Larkin and Y. N. Ovchinnikov. Zh. Eksp. Teor. Fiz. **47**, 1136 (1964).
- [80] P. Fulde and R. A. Ferrell. Phys. Rev. **135**, 550 (1964).
- [81] A. Bulgac and M. M. Forbes. Phys. Rev. Lett. **101**, 215301 (2008).
- [82] Y. Liao, A. Rittner, T. Paprotta, W. Li, G. Partridge, R. Hulet, S. Baur and E. Mueller. Nature **467**, 567 (2010).
- [83] C. Mora and R. Combescot. Phys. Rev. B **71**, 214504 (2005).
- [84] N. Yoshida and S.-K. Yip. Phys. Rev. A **75**, 063601 (2007).
- [85] M. M. Parish, F. M. Marchetti, A. Lamacraft and B. D. Simons. Phys. Rev. Lett. **98**, 160402 (2007).
- [86] R. Duine and H. Stoof. Physics Reports **396**, 115 (2004). ISSN 0370-1573.
- [87] M. W. J. Romans and H. T. C. Stoof. Phys. Rev. Lett. **95**, 260407 (2005).
- [88] J. Negele and H. Orland. *Quantum Many-Particle Systems*. Westview Press, Boulder (1998).
- [89] H. T. C. Stoof, K. B. Gubbels and D. B. M. Dickerscheid. *Ultracold Quantum Fields*. Theoretical and Mathematical Physics. Springer (2009).
- [90] P. Chaikin and T. Lubensky. *Principles of Condensed Matter Physics*. Cambridge University Press (1995).
- [91] M. Iskin and C. A. R. Sá de Melo. Phys. Rev. A **77**, 013625 (2008).
- [92] A. L. Fetter. Phys. Rev. B **14**, 2801 (1976).
- [93] G. Sarma. J. Phys. Chem. Solids **24**, 1029 (1963).
- [94] H. Kleinert. Fortschr. Phys. **26**, 565 (1978).
- [95] T. Paananen, P. Törmä and J.-P. Martikainen. Phys. Rev. A **75**, 023622 (2007).
- [96] M. M. Parish, F. M. Marchetti, A. Lamacraft and B. D. Simons. Nature Physics **3**, 124 (2007).
- [97] A. Buzdin and H. Kachkachi. Phys. Lett. A **225**, 341 (1997).
- [98] L. Radzihovsky. Phys. Rev. A **84**, 023611 (2011).
- [99] L. Jiang and J. Ye. Phys. Rev. B **76**, 184104 (2007).
- [100] D. Kim and P. Törmä. Phys. Rev. B **85**, 180508(R) (2012).
- [101] L. Dong, L. Jiang and H. Pu. arXiv:1302.1189 (2013).
- [102] K. Seo, L. Han and C. Sá de Melo. arXiv:1301.1353 (2013).
- [103] A. Meyerovich. Phys. Lett. A **76**, 297 (1980).

- [104] Y. Matsuda and H. Shimahara. *J. Phys. Soc. Jpn.* **76**, 051005 (2007).
- [105] R. Casalbuoni, R. Gatto, N. Ippolito, G. Nardulli and M. Ruggieri. *Phys. Lett. B* **627**, 89 (2005).
- [106] M. Mannarelli, K. Rajagopal and R. Sharma. *Phys. Rev. D* **73**, 114012 (2006).
- [107] K. Rajagopal and R. Sharma. *Phys. Rev. D* **74**, 094019 (2006).
- [108] N. Ippolito, G. Nardulli and M. Ruggieri. *JHEP04* **036** (2007).
- [109] M. Mannarelli, K. Rajagopal and R. Sharma. *Phys. Rev. D* **76**, 074026 (2007).
- [110] J. Edge and N. Cooper. *Phys. Rev. Lett.* **103**, 065301 (2009).
- [111] I. Zapata, F. Sols and E. Demler. *Phys. Rev. Lett.* **109**, 155304 (2012).
- [112] L. Radzihovsky and A. Vishwanath. *Phys. Rev. Lett.* **103**, 010404 (2009).